

**DESIGN AND SIMULATION OF REUSED ELECTRIC VEHICLE
BATTERY SYSTEMS FOR HOME ENERGY STORAGE AND
VEHICLE CHARGING**

A Dissertation
Presented to
The Academic Faculty

by

Reid Spence

In Partial Fulfillment
of the Requirements for the Degree
Master of Science in Mechanical Engineering

Georgia Institute of Technology
May 2018

COPYRIGHT © 2018 BY REID SPENCE

**DESIGN AND SIMULATION OF REUSED ELECTRIC VEHICLE
BATTERY SYSTEMS FOR HOME ENERGY STORAGE AND
VEHICLE CHARGING**

Approved by:

Dr. Bert Bras, Advisor
School of Mechanical Engineering
Georgia Institute of Technology

Dr. Samuel Graham
School of Mechanical Engineering
Georgia Institute of Technology

Dr. Chris Paredis
Department of Automotive Engineering
Clemson University

Date Approved: May 23rd, 2018

ACKNOWLEDGEMENTS

I would like to thank my advisor, Dr. Bert Bras for his guidance in the creation of this thesis and for his mentorship over the past several years.

I would like to thank Ford Motor Company who funded much of this work and Ford team members Jacob Mathews, John Snyder, Luke Spinolo, and Noam Zimet for their assistance and feedback.

I would like to thank Jakob Rattay for his collaboration on this work and for his continuation of this project upon my leave. I would also like to thank all my lab-mates for helping me through the thesis process.

Finally, I would like to thank my friends and family for their continuous support and encouragement.

TABLE OF CONTENTS

ACKNOWLEDGEMENTS	iii
LIST OF TABLES	vii
LIST OF FIGURES	ix
LIST OF SYMBOLS AND ABBREVIATIONS	xv
SUMMARY	xvi
CHAPTER 1. Introduction	1
1.1 Opportunities for Second Life Batteries	1
1.2 Potential for Second-life Batteries as Residential Energy Storage	2
1.3 The Challenging Economics for Residential Energy Storage	4
1.4 Proposed Solution – Addition of DC Fast Charging	6
CHAPTER 2. Background	9
2.1 Technical Background	10
2.1.1 Lithium-ion Batteries	10
2.1.2 Heat and Temperature in Lithium-ion Batteries.	16
2.1.3 Degradation of Lithium-ion Batteries	19
2.2 Literature Review	25
2.2.1 Simulation Based Studies	25
2.2.2 Experimental Studies	28
2.2.3 Discussion	29
2.3 Review of Industry	30
2.3.1 Currently Available Products for Home Energy Storage	30
2.3.2 Industry Projects for Home Energy Storage with Reused EV Batteries	33
2.3.3 Industry Projects for DC Fast Charging Stations with Reused EV Batteries	35
2.4 Background on Selected Electric Vehicles	37
2.4.1 2013 Chevy Volt Battery Pack	37
2.4.2 2013 Nissan Leaf	42
2.4.3 2013 Ford Focus Electric	45
2.4.4 Summary of Battery Parameters	46
CHAPTER 3. Methods	49
3.1 Summary of Methods	49
3.2 Proposed Device	51
3.2.1 General Design	51
3.2.2 Electrical Design	52
3.2.3 Thermal Management Design	55
3.3 Battery Thermal Model	64
3.3.1 Generalized Thermal Model Set-up	64

3.3.2	Battery Heat Generation Model	69
3.3.3	Modelling for Adiabatic Conditions	73
3.3.4	Modelling for Passive Thermal Management	74
3.3.5	Modelling Active Liquid Cooling	79
3.3.6	Modelling Active Air Cooling	92
3.4	Electrical Model	97
3.5	Fluid Model	100
3.5.1	Validation	103
3.6	Degradation Model	105
3.7	Case Studies for Performance in Realistic Scenarios	107
3.7.1	Summary	107
3.7.2	Household Demand and PV Modelling	108
3.7.3	Vehicle Charge Modelling	115
3.7.4	Simplified Battery Thermal Model	120
3.7.5	Battery Control Scheme	123
3.7.6	Simulation Process	126
3.7.7	Simulation Parameters	128
3.8	Handling Uncertainty	130
3.8.1	Estimating Battery Health at End of Vehicle Life	130
3.8.2	Uncertainty in Thermal Parameters	137
CHAPTER 4.	Results	140
4.1	Thermal Performance Under Adiabatic Conditions	140
4.1.1	Step Response to Various C-rates	140
4.1.2	Step Response to Various Discharge Powers	140
4.1.3	Discussion	143
4.2	Thermal Performance with Passive Thermal Management	145
4.2.1	Step Response to Various Discharge Powers	145
4.2.2	Cool Down Rate	146
4.2.3	Uncertainty and Sensitivity Analysis	147
4.2.4	Discussion	149
4.3	Thermal Performance with Active Liquid Cooling	151
4.3.1	Step Response to Various Discharge Powers	151
4.3.2	Cool Down Rate	155
4.3.3	Parameters Sweep of Cooling Capacity	156
4.3.4	Uncertainty and Sensitivity Analysis	157
4.3.5	Discussion	160
4.4	Thermal Performance with Active Air Cooling	161
4.4.1	Step Response to Various Discharge Powers	161
4.4.2	Cool Down Rate	163
4.4.3	Parameter Sweep	164
4.4.4	Uncertainty and Sensitivity	165
4.4.5	Discussion	166
4.5	Fluid Analysis and Thermal Management Power Consumption	168
4.5.1	Liquid Cooling	168
4.5.2	Air Cooling	171
4.5.3	Discussion	173

4.6	Comparison of Thermal Management Methods	175
4.7	Simple Life Estimates	178
4.8	Case Study Simulation of Realistic Use in Homes	182
4.8.1	Home Energy Use without Storage Device	182
4.8.2	Home Energy Use with Storage Device	185
4.8.3	General Observations	189
4.8.4	Discussion	194
CHAPTER 5.	Conclusions and Future Work	196
REFERENCES		200

LIST OF TABLES

Table 1 – Summary of battery pack parameters for selected EV’s.....	47
Table 2 – Summary of battery cell parameters for slected EVs	48
Table 3 – Natural convection coefficients for a variety of air and cell temperatures	77
Table 4 – Nusselt number correlations for laminar flow in rectangular ducts [64].....	87
Table 5 – Parameters used by Chen et al. [62]	89
Table 6 – Parameters for calculating open circuit voltage.....	98
Table 7 – Minor loss coeficients for pipe flow from literature [69]	102
Table 8 – Typical values of pump and fan effeciencies from literature	103
Table 9 – Simulation paramters for thermal management.....	128
Table 10 – Simulation paramters for battery controls	129
Table 11 – Simulation paramters for power electronics	129
Table 12 – Simulation paramters for electric vehicle	129
Table 13 – Battery waranty for selected electric vehicles	131
Table 14 – INL Advanced Vehicle Testing conditions	132
Table 15 – Estimations from Neubauer et al (2015) for battery health at end of vehicle life	134
Table 16 – Base case and uncertainty disctributions for vehicle ageing	135
Table 17 – Thermal properties of large pouch lithium-ion cells from literature	138
Table 18 – Base case and uncertainty distributions for thermal parameters.....	139
Table 19 – Time constant for cooldown of battery cells	147
Table 20 – Heat exchanger and liquid chiller data used for	152
Table 21 – Time constant for cooldown of battery cells with liquid cooling after 50 kW discharge	156
Table 22 – Time constant for cooldown of battery cells with air cooling	164

Table 23 – Summary of ageing scenario conditions	179
Table 24 – Energy consumption of case study homes before the addition of energy storage	183
Table 25 – Comparison of utility rates chosen for each city for summer period.....	185
Table 26 – Change in energy consumption for one year simulation	186
Table 27 – Energy cost savings for one year simulation	187
Table 28 – DC fast charging energy delivered to vehicle for one year simulation	188

LIST OF FIGURES

Figure 1 – General diagram of lithium-ion battery components [23].....	10
Figure 2 – Illustration of movement of lithium ions inside lithium-ion Batttery [24].....	11
Figure 3 – Different battery cell configurations [24].....	13
Figure 4 – Open circuit potential versus capacity for various lithium-ion chemestries [25]	14
Figure 5 – lithium-ion batteries at the cell, module, and pack level for two vehicles [24]	15
Figure 6 – Manganese from positive electrode catalyzing SEI growth on negative electrode [2]	21
Figure 7 – SEI formation and growth process [2].....	21
Figure 8 – Example of lithium plating with dendrite formation [2]	22
Figure 9 – Example of the possible stages of degradation for lithium-ion cells [2].....	24
Figure 10 – The Tesla Powerwall 2 [43]	30
Figure 11 – Tesla Powerwall 2 instillation configuration for partial home backup [43]..	31
Figure 12 – High voltage LG Chem RESU residential storage products and specs [44].	32
Figure 13 – The sonnenBatterie Eco [45]	33
Figure 14 – Nissan's XSTORAGE which is expected to have an option with reused Leaf batteries [46]	34
Figure 15 – BMW's battery reuse project for home energy storage with i3 battery packs [48].....	34
Figure 16 – E-stor DC fast charging system with second life Renault batteries [18].....	36
Figure 17 – The Chevy Volt battery pack [50]	38
Figure 18 – Chevy Volt showing location of battery pack and motor [50]	38
Figure 19 – A Chevy Volt pouch cell [52]	39
Figure 20 – Chevy Volt cell cooling fin and manifold	40

Figure 21 – Chevy Volt cooling circuit [2].....	41
Figure 22 – a 2013 Chevy Volt cell inside its plastic frame (a) and the adjacent liquid cooling fin (b)	42
Figure 23 – Nissan Leaf with battery pack location shown [53]	43
Figure 24 – Cell, module, and pack in Nissan Leaf [54]	43
Figure 25 – The purchased module from a 2013 Nissan Leaf (a) and the same module with the front face of the aluminum cover removed to show the cells (b).	44
Figure 26 – Hypothosised air flow in and out of module casing (a); hypothesised air flow around edges of cells inside module (b)	45
Figure 27 – Ford Focus Electric with motor and battery pack shown [57]	46
Figure 28 – Diagram of system electrical topology.....	55
Figure 29 – Active liquid cooling concept circuit diagram	58
Figure 30 – Simplified active liquid cooling circuit with chiller removed.....	59
Figure 31 – Example of heat exchanger from ATS Inc [60]	60
Figure 32 – Pressure drop and heat transfer coefficient for various sized heat exchangers from ATS Inc [60]	60
Figure 33 – Example of coolant chiller from liard technologies [61].....	61
Figure 34 – Original air flow design around Nissan Leaf cell (a) vs the air flow assumed for active air cooling in our device (b).....	62
Figure 35 – Diagram of air flow for active air thermal management design.....	63
Figure 36 – Original gemoetry of the cells (a) (example shown is Volt cell); Defined gemetry of the cell for thermal model with orientation and axis defined (b).	66
Figure 37 – Heat flows in thermal model for passively cooled cells.....	67
Figure 38 – Heat flows and model domain for liquid cooled cells.....	68
Figure 39 – Heat flows and model domain for air cooled cells	69
Figure 40 – Entropic heat coefficient for LMO cell [30].....	70
Figure 41 – Change in relative internal resistance with temperature.....	72

Figure 42 – Validation of heat generation model by comparison with Liu et al. (2014) [30].....	73
Figure 43 – Example of simplified fin and cell geometry for liquid cooled model.....	82
Figure 44 – Example of thermal node numbering	83
Figure 45 – Model geometry used by Chen et al. [62].....	88
Figure 46 – Comparison of cell average temperature and temperature difference between our model and the model from Chen et al. for the end of a 2.71 C discharge.	90
Figure 47 – Comparison of cell surface temperature from our model (b) and the model from Chen et al. (a) for the end of a 2.71 C discharge and 0.29 g/s of coolant flow	91
Figure 48 – Convergence study for average cell temperature and cell temperature gradient for liquid cooled Volt cell after 3C discharge.....	92
Figure 49 – Example of model geometry for active air cooled case.....	93
Figure 50 – Comparison of cell average temperature and temperature difference between our model and the model from Chen et al. for the end of a 2.71 C discharge.	95
Figure 51 – Comparison of cell surface temperature from our model (b) and the model from Chen et al. (a) for the end of a 2.71 C discharge and 0.9 g/s of air flow.	95
Figure 52 – Convergence study for average cell temperature and cell temperature gradient for air cooled Leaf cell after 3C discharge.....	96
Figure 53 – Battery equivalent circuit model	99
Figure 54 – Fluid-circuit analogy for pressure drop	100
Figure 55 – Comparison of results from our model and the CFD model from Chen et al. for coolant channel pressure drop of a liquid fin cooled battery (a) and an air cooled battery (b).....	104
Figure 56 – Parameters used to create the DOE residential load profiles [75].....	109
Figure 57 – Example house load profile with appliances marked [76]	110
Figure 58 – Comparison of 5-min load data to hourly averaged load data [77].....	110
Figure 59 – Example of sub-hourly variations effect on energy storage use.....	112
Figure 60 – Example of TMY hourly data vs 5-min synthetic model output.....	113
Figure 61 – Example of the synthetic variation in residential demand.....	115

Figure 62 – Number of charge events per day in 2011 for Nissan Leaf owners in EV Project [80].....	116
Figure 63 – State of charge at start of charge event for Nissan Leaf owners in EV Project [80].....	117
Figure 64 – Probability density functions for number of home charge events per day for weekdays (a) and weekends (b).	118
Figure 65 – Example charge events for one week. Figure a) is the beginning state of charge. Figure b) is the start time.....	119
Figure 66 – Battery control algorithm	124
Figure 67 – Thermal management control algorithm	125
Figure 68 – Simulation process.....	126
Figure 69 – Relative capacity loss for vehicles in INL’s Advanced Vehicle Tests.....	132
Figure 70 – Relative resistance growth for vehicles in INL’s Advanced Vehicle Tests	133
Figure 71 – Uncertainty distribution CDF generated for capacity loss at end of vehicle life	136
Figure 72 – Uncertainty distribution CDF generated for resistance at end of vehicle life	137
Figure 73 – Battery cell temperature for different rates of discharge under adiabatic conditions under 1C discharge (a), 2C discharge (b), 3C discharge (c), and 4C discharge (d).....	141
Figure 74 – Battery cell temperature for different rates of discharge under adiabatic conditions under 10 kW discharge (a), 25 kW discharge (b), 50 kW discharge (c), 100 kW discharge (d).....	143
Figure 75 – Battery cell temperature for different rates of discharge under passive thermal management under 10 kW discharge (a), 25 kW discharge (b), 50 kW discharge (c), 100 kW discharge (d).....	146
Figure 76 – Distribution of maximum cell temperature (a) and cooling time constant (b) for all monte-carlo runs for step discharge at 50 kW.....	148
Figure 77 – Sensitivity of (a) max temperature and (b) cooling time constant to uncertainty in parameters.....	149
Figure 78 – Step response of battery pack paired with 100 W/K heat exchanger to 25 kW (a), 50 kW (b), and 100 kW (c) discharge.	154

Figure 79 – Step response of battery pack paired with 170 W/K heat exchanger to 25 kW (a), 50 kw (b), and 100 kW (c) discharge.	154
Figure 80 – Step response of battery pack paired with 170 W/K heat exchanger to 25 kW (a), 50 kw (b), and 100 kW (c) discharge.	154
Figure 81 – Temperature for cross sections of Volt cell after 50 kW discharge for “medium cooling” case	155
Figure 82 – Effect of heat exchanger cooling capacity and liquid chilling rate to the average cell temperature at end of 50 kW discharge	157
Figure 83 – Distribution of maximum cell temperature (a), cooling time constant (b), and cell temperature gradient (c) for all monte-carlo runs for step discharge at 50 kW with liquid cooling	158
Figure 84 – Sensitivity of max temperature (a), cooling time constant (b), and cell temperature gradient (c) to uncertainty in parameters for liquid cooled batteries under 50 kW discharge and “medium cooling” case	159
Figure 85 – Figure Step response of air cooled battery with 500 m ³ /h of air flow heat exchanger to 25 kW (a), 50 kw (b), and 100 kW (c) discharge.	162
Figure 86 – Figure Step response of air cooled battery with 1500 m ³ /h of air flow heat exchanger to 25 kW (a), 50 kw (b), and 100 kW (c) discharge.	162
Figure 87 – Figure Step response of air cooled battery with 3000 m ³ /h of air flow heat exchanger to 25 kW (a), 50 kw (b), and 100 kW (c) discharge.	162
Figure 88 – Temperature for cross sections of Leaf cell after 50 kW discharge with 1500 m ³ /hr of air flow.	163
Figure 89 – Parameter sweep of air cooling gap size and air flow rate for air cooled battery after 50 kW discharge.	165
Figure 90 – Distribution of maximum cell temperature (a), cooling time constant (b), and cell temperature gradient (c) for all Monte Carlo runs for step discharge at 50 kW with active air cooling	166
Figure 91 – Pressure drop and power consumption for coolant flow across liquid cooled battery pack	169
Figure 92 – Pressure drop and power consumption for different components in liquid cooling loop	170
Figure 93 – Power consumption of different liquid cooling system configurations seperated by pump, fan, and chiller	171

Figure 94 – Pressure drop and power consumption for coolant flow across air cooled Leaf battery pack.....	172
Figure 95 – Power consumption of different active air cooling flow rates by power to drive fluid through battery pack and air filter.	173
Figure 96 – Comparison of thermal managment methods for 50 kW discharge	176
Figure 97 – Comparison of thermal management method power consumption under “medium cooling” case.....	177
Figure 98 – Capacity degredation estimates in second-life under different scenarios ...	180
Figure 99 – Comparison of utility rates in selected locations for summer months	184
Figure 100 – Example of battery temperature for Volt battery during first week of the year in Phoenix home.....	189
Figure 101 – Example of battery SOC for Volt battery during first week of the year in Phoenix home.....	191
Figure 102 – Example of grid use with and without Volt battery during first week of the year in Phoenix home.....	192
Figure 103 – Example of battery temperature for Focus battery during summer week in Phoenix home.....	193
Figure 104 – Example of battery temperature for Volt battery during winter week in Chicago home.	194

LIST OF SYMBOLS AND ABBREVIATIONS

B2U	Battery Second Use
CFD	Computational Fluid Dynamics
DCFC	Direct Current Fast Charging
DOD	Depth of Discharge
EOL	End of Life
EV	Electric Vehicle
EVSE	Electric Vehicle Supply Equipment
INL	Idaho National Labs
kWh	Kilo-watt-hour
LMO	lithium-manganese-oxide
MPPT	Maximum Power Point Tracker
NREL	National Renewable Energy Laboratory
PV	Photovoltaic
SEI	Solid Electrolyte Interphase
SOC	State of charge
TMY	Typical Meteorological Year
UPS	Uninterruptible Power Source

SUMMARY

As electric vehicles become more prevalent on today's roads, there is a question as to what to do with the lithium-ion batteries after the vehicles have reached end-of-life. One proposed solution is to reuse the batteries as energy storage for a home to provide energy cost savings, increased energy independence, and back-up power. However, several studies have shown that the economics of such use cases can be challenging. Thus, we propose the addition of another use case: providing DC fast charging to an electric vehicle. Because the batteries can be charged slowly and discharged quickly to charge a vehicle, the high cost of the electrical infrastructure typically required for fast charging can be avoided, and home fast charging may provide enough value to the user to offset the upfront cost of such a device.

In this thesis we examine three existing electric vehicle batteries and propose a generalized design to reuse them for home energy storage and vehicle charging. We put emphasis on how the existing thermal management components can be reused to allow for high rates of discharge at minimal additional cost. We create an electro-thermal model to estimate the thermal performance of such systems while accounting for uncertainty. We also estimate the thermal management system power consumption and effect thermal management has on battery lifetime. We conclude with a simulation of the device's use in three US cities and calculate performance based on changes in household energy use, energy cost, and the amount of vehicle fast charging provided.

Results show that for low power draws, like those required to power a home, passive cooling methods are adequate due to the low heat generated relative to the high

thermal mass of the batteries. However, at the higher discharge rates like the 50 kW typical of DC fast charging, the batteries see a significant temperature rise under passive cooling and also take several hours to cool back down. This is undesirable for safety reasons and for mitigating the rate of battery degradation. Including active liquid or air cooling significantly reduces the maximum battery temperature and cooldown rate, increasing safety and reducing degradation. Additionally, estimates for the power consumption of these active thermal management systems show that fans dominate the power use, but overall the total consumption is relatively low (on the order of 100 watts).

Simulations of realistic usage in homes shows that the devices can reduce grid reliance by around 20% and provide an average of around 20 miles of charge in 10 minutes per fast charge event. However, inefficiencies in the system increase overall energy consumption slightly and energy cost savings are minimal in most cases. Additionally, close analysis of the simulations reveals tradeoffs between providing home energy storage and vehicle charging.

Ultimately, the results of this study prove the feasibility of reusing electric vehicle batteries for home energy storage and vehicle fast charging, however additional studies are required to determine if such devices are economically viable. This would include estimates of system cost, the utility of home vehicle fast charging to customers, and more detailed analysis of battery degradation in both first and second life. Such information could also be used to determine the optimal battery energy management and thermal management strategy.

CHAPTER 1. INTRODUCTION

1.1 Opportunities for Second Life Batteries

Electric vehicles (EVs) are becoming ever more prevalent on roads across the United States and the world. An estimate by Bloomberg New Energy Finance predicts electric vehicles will outsell internal combustion engine vehicles globally by 2038 [1]. Electric vehicles are an attractive option for those looking to reduce emissions and mitigate their climate impact, however, the batteries that power these vehicles degrade over time [2, 3]. Eventually when these batteries reach approximately 70-80% of their original energy capacity they are expected to be no longer desirable for use in electric vehicles [4]. What to do with these batteries after vehicle life is a current issue of debate. Placing these batteries in a landfill is undesirable due to their mild toxicity, and proper dismantling and recycling of these batteries is currently a costly endeavor, with the reclaimed value of the materials rarely offsetting the costs [3]. For these reasons many have proposed that reusing these batteries at end of vehicle life (EOL) as stationary energy storage might provide the greatest benefits for the economy and environment, by producing additional value and offsetting some demand for new batteries before their eventual recycling [4].

1.2 Potential for Second-life Batteries as Residential Energy Storage

It is expected that at end of vehicle life, the now decreased energy density of the batteries makes them unsuitable for automotive use, however they could be used in stationary applications where weight and size are of lesser importance [4-6]. This could be done at a grid-level scale or at a residential, commercial, or industrial scale where they could provide a variety of functions such as demand shifting, renewable energy storage, or frequency regulation [5]. Studies project that demand from any one of these use cases will not match the supply of second-life batteries, and thus multiple use cases must be considered [4].

One such use case is to reuse EV batteries to provide behind-the-meter energy storage for homes. Companies like Tesla already sell new batteries for home energy storage and some have proposed that a similar product could be made with reused electric vehicle batteries [6-8]. Residential energy storage can be used for several different applications, including:

- *Energy shifting*: shifting energy use from high price peak times to low cost times.
- *Demand charge reduction*: reducing the peak power demand of the home to avoid demand charges from the utility.
- *Solar energy storage*: storing rooftop solar energy to offset temporal variation in production and demand.
- *Back-up power*: providing back-up power during power outages.

The value to the customer comes not just from direct monetary savings on their energy bill due to energy shifting and demand charge reduction, but also the value of greater energy independence from solar storage and the value of increased resilience from back-up power. If the combined value of these functions exceeds the costs of a second-life battery system, then such a device will be economically viable.

1.3 The Challenging Economics for Residential Energy Storage

For many people, the capabilities of home energy storage systems are attractive, however some studies have found that implementing home energy storage has marginal economic returns if any at all for most US locations under current electricity prices [9, 10]. One reason is that batteries and the necessary power electronics have efficiency losses which can increase the total energy consumption of the house and degrade the benefits of energy shifting and demand reduction. Another reason is the prevalence of “net-metering” rates available in many areas of the US, which remove the economic incentive to store rooftop solar energy. Net-metering allows a homeowner to subtract the electricity they supply to the grid from their demand. From an economic perspective, a resident under a net-metering policy can effectively use the grid as a 100% efficient, infinite capacity energy storage system, with which a stationary battery cannot compete [10, 11]. Even without net-metering, and where a customer is paid nothing for power returned to the grid, Hittinger and Siddiqui (2017) found that most US location will still not see a profit from adopting energy storage [10]. This is mostly due to the high capital cost of the battery, and the economics may be improved if capital cost can be significantly decreased by using second-life batteries instead. However, even if the cost of the storage device falls, as Hittinger and Siddiqui point out, the utility would likely be able to adopt that same storage system and provide it at lower cost than a single resident could, due to economies of scale, suggesting the implausibility, in the long run, of producing and storing one’s own energy cheaper than it can be bought from the grid.

Even if economic returns for energy cost savings are marginal, a customer may still buy a home energy storage device if the perceived value of energy independence and back-

up power are sufficiently high. The exact value people assign to these is unknown, but current marketing for Tesla's Powerwall home energy storage product suggest it is a significant reason why people buy home energy storage, as their website quotes to prospective buyers how much a Powerwall can reduce grid use and how many days of back-up power are provided, but does not quote expected energy costs [12]. Despite this, a survey of potential consumers of home energy storage in Australia found that most ranked a reduction in energy cost as more important than reduced reliance on the grid, and much more important than back-up power [13]. Additionally, the amount of power outages seen by the average US consumer is low (1.3 times per year with average outage time around 3 hours in 2015) [14], and the upfront cost of the battery is likely higher than most customers are willing to pay for backup power [11]. Thus, the demand for home energy storage devices with second use batteries may not match the price of the batteries under the currently proposed functions of energy shifting, demand charge reduction, solar energy storage, and back-up power.

1.4 Proposed Solution – Addition of DC Fast Charging

As discussed, the large supply of used electric vehicle batteries expected in the future will require many applications for second-life use to accommodate the large influx of used batteries in the future. One such application is home energy storage, however the economics of energy shifting, demand reduction, solar energy storage, and back-up power may not offset the cost of batteries. Thus, to increase the value of the using second life EV batteries as home energy storage, we propose an additional use case for such a system: vehicle direct current fast charging (DCFC).

Most electric vehicle charging is done with AC power at two levels, level 1 and level 2 [15]. Level 1 is equivalent to plugging your car into any standard outlet, which provides about 2-5 miles of charge per hour. Level 2 requires a dedicated electric vehicle supply equipment (EVSE) but can provide 10-20 miles of range per hour. Both take several hours to fully charge a vehicle, which requires the driver to plan their use of the vehicle around these charging events and contributes to a constant concern not to strand oneself by running out of charge, often referred to as “range anxiety” [16]. Charging with direct current on the other hand, referred to as DC fast charging or level 3, can supply up to 60-80 miles of range in 20 minutes [15]. Faster charging is more attractive to consumers as it can increase the utilization of electric vehicles and can reduce range anxiety. However, DC fast chargers are only sparsely available in commercial locations and are rarely found in residential locations due to the need to install higher voltage, higher current, and possibly multi-phase power lines which makes installation expensive [15].

One way to resolve this issue is to use battery storage for DC fast charging to reduce the amount of grid infrastructure required for installation [17]. The batteries can be charged up slowly and then discharged quickly which smooths out the power draw on the infrastructure. Such a system may make providing DC fast charging in one's home practical. Stationary energy storage systems with new batteries could be used for this however most of these are designed for low power (~10 kW) compared to the high power (25-100 kW) that may be required for home DCFC. Used electric vehicle batteries could be particularly well suited to this application because they are design for high power draw and have built in thermal management mechanisms like fluid cooling channels to handle the increased heat generation. These thermal management systems imbedded in EV battery packs may be reused at comparatively low cost and allow for higher power discharge. Several companies have already proposed reusing electric vehicle batteries for DC fast charging of electric vehicles in commercial locations, however to date we have not found any systems designed for use in residential locations [18-20].

In this thesis we propose a generalized design for a system with used electric vehicle batteries to be repurposed to pair residential energy storage with electric vehicle fast charging. We put emphasis on how thermal management strategies for the system can incorporate the parts of the existing systems in EV batteries to allow for greater discharge power at reduced cost. We study the thermal performance of our system with different thermal management strategies for varying degrees of discharge to determine feasibility and optimal design. Additionally, we run simulations of such systems in realistic usage scenarios for three households in Los Angeles, Phoenix, and Chicago respectively to

determine performance in terms of energy savings, increased energy independence, and vehicle charging speed.

CHAPTER 2. BACKGROUND

This chapter will provide an overview of the relevant technical concepts, review the related literature and industry projects, and provide a background on the electric vehicle batteries chosen for this study. In Section 2.1, we start by reviewing the theoretical background on lithium-ion batteries for topics that are necessary to understand the later analysis. These topics include the basics of lithium-ion batteries in electric vehicles, heat and temperature considerations, and battery degradation. In Section 2.2, we review the recent literature on reusing electric vehicle batteries for residential energy storage and electric vehicle charging, including studies on economic feasibility, expected battery lifetime, and experimental tests and prototypes. In Section 2.3, we summarize similar products from industry including the current market of home energy storage products and battery reuse pilot projects done by automakers and others in industry. In Section 2.4, we present information on the three electric vehicle batteries selected for this study, the Chevy Volt, the Nissan Leaf, and the Ford Focus Electric. This includes information on battery pack construction and thermal management strategies, which will be important for designing and analyzing our concept device.

2.1 Technical Background

2.1.1 Lithium-ion Batteries

The most popular battery technology used in electric vehicles today is lithium-ion batteries [21]. These batteries are composed of a positive electrode (cathode) and a negative electrode (anode), which are submerged in an electrolyte solution and, kept electrically isolated via a separator. The electrodes are also attached to current collectors to carry electrons to and from the electrodes [2, 22]. A simplified diagram of the components of a lithium ion battery are shown in Figure 1.

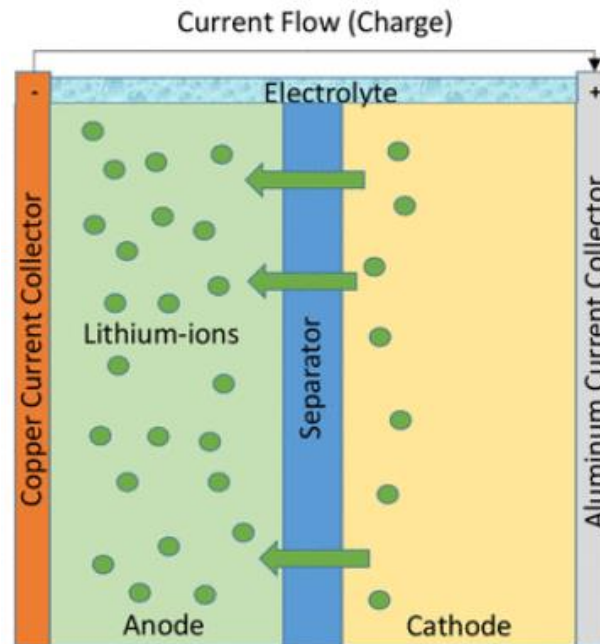


Figure 1 – General diagram of lithium-ion battery components [23]

The battery stores and releases energy through the storage and movement of lithium ions. An illustration of this process is shown in Figure 2. When a battery is fully charged, most of the lithium ions are stored in the negative electrode in a process called intercalation, where the lithium ions are inserted into the crystal structure of the electrode material [22]. When the battery is discharged, electrons are free to move from the positive electrode, through the current collectors and through some load circuit to the negative electrode. At the same time the lithium ions separate from the negative electrode, pass through the electrolyte and separator, to intercalate in the positive electrode [22, 24]. During charging the process is similar but run in reverse. It is through the movement and storage of these charged particles that energy is stored in the battery, thus the amp-hour capacity of the battery is determined by the number of lithium ions that are active in this process.

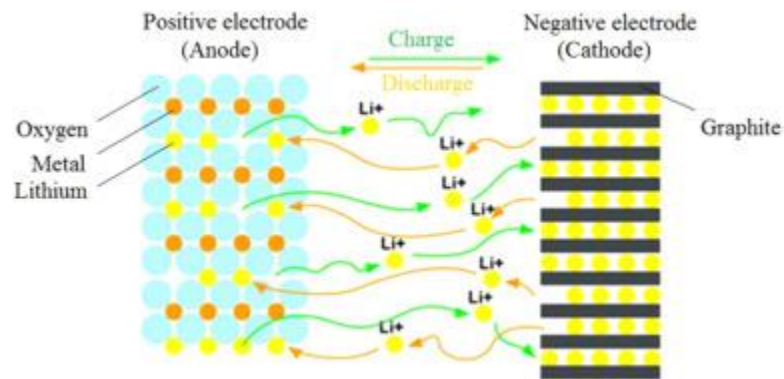


Figure 2 – Illustration of movement of lithium ions inside lithium-ion Battery [24]

There are many different types of lithium-ion batteries typically classified by the choice of electrode materials, although the choice of materials for other components such

as the electrolyte can also have impacts on the performance of the battery. Though most lithium-ion batteries today use graphite for the negative electrode, the choice for positive electrode material varies widely across the industry [22]. Some examples positive electrode materials include LiFePO_4 (LiFePO), LiMn_2O_4 (LMO), $\text{Li}(\text{NiMnCo})\text{O}_2$ (NMC), and $\text{Li}(\text{NiCoAl})\text{O}_2$ (NCA) [22]. Although operating through the same general principles the choice of positive electrode materials comes with advantages and disadvantages in terms of energy capacity, resistance, safety, and lifetime [22].

A single self-contained unit of positive and negative electrodes is referred to as a cell, which for lithium-ion batteries has an nominal voltage around 3.2-3.8 V depending on the choice of electrode materials [23]. These cells can come in different shapes such as:

- *cylindrical cells*: where the battery electrodes and separator are spun in a cylinder and enclosed in a hard case.
- *prismatic cells*: where the electrodes and separators are laid out in a rectangular shape and enclosed in a hard case.
- *pouch cells*: where the active materials are wound in to a flat shape and enclosed in a non-rigid case.

Figure 3, shows an example construction for each of these cell configurations.

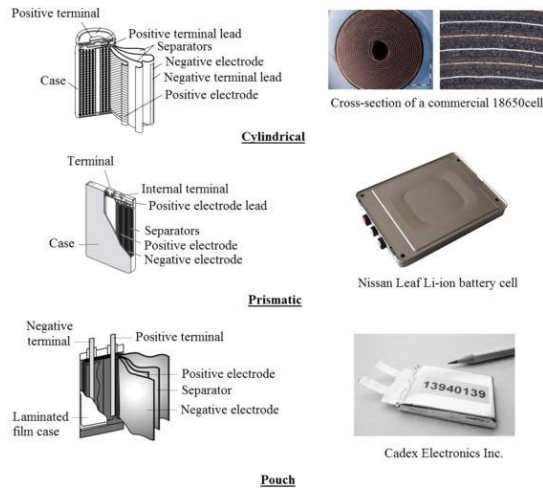


Figure 3 – Different battery cell configurations [24]

The voltage of a single cell depends on the cell chemistry and changes with cell state of charge [25]. Figure 4 shows the voltage of different lithium-ion cell chemistries versus capacity. The maximum voltage occurs at full charge and minimum at zero charge. The open circuit voltage can also vary from the closed circuit voltage due to internal resistance losses and electrode polarization [23].

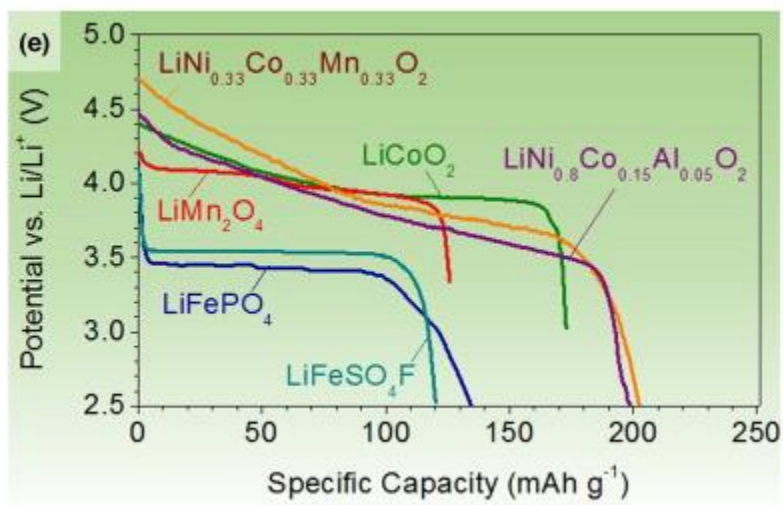


Figure 4 – Open circuit potential versus capacity for various lithium-ion chemistries [25]

For most high energy and power operations like electric vehicles and stationary storage systems, use of a single cell is unpractical and thus multiple cells are combined into a single unit called a pack [23, 24]. Typically, the phrase “battery pack”, does not refer to the collection of battery cells alone but also the integrated battery management circuits, electrical routing, and thermal management systems inside a self-contained box [24]. Additionally, sometimes small subunits of batteries inside the pack are referred to as modules, and further collections of modules may be referred to as arrays. These modules and arrays may or may not have their own integrated control and monitoring circuits as well as thermal management sub-systems such as cooling fins. Figure 5, shows an example of two electric vehicle batteries at the cell, module, and pack level.

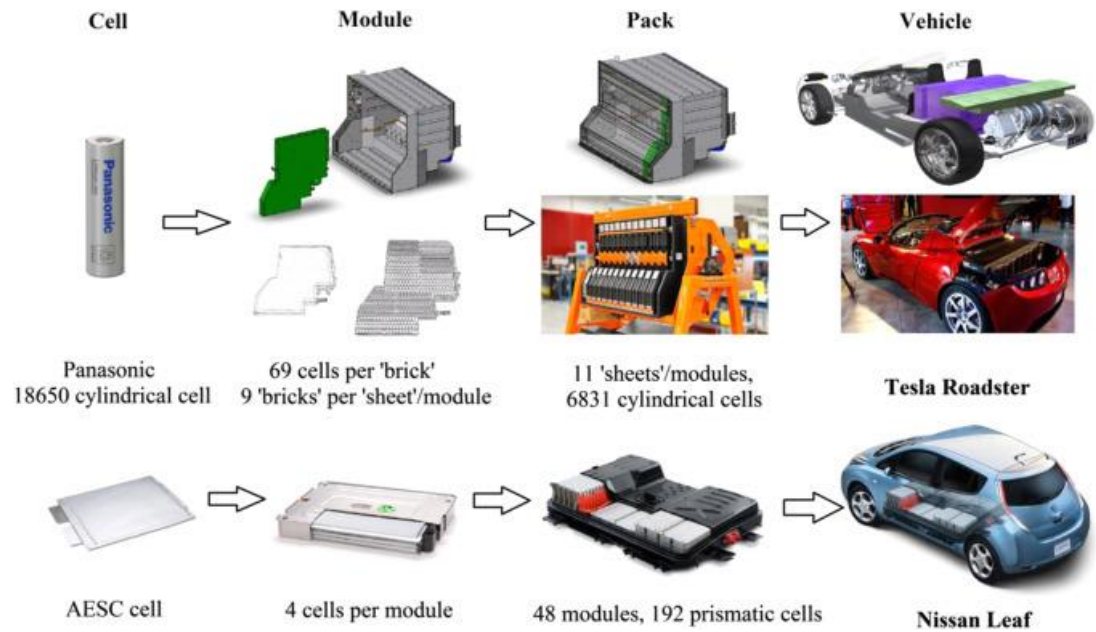


Figure 5 – lithium-ion batteries at the cell, module, and pack level for two vehicles [24]

There are several terms that are often used to describe the state and use of lithium-ion batteries. One is state of charge or SOC which is typically measured as the percentage of remaining capacity for a battery versus the capacity at full charge in amp-hours [26]. Thus, at full charge a battery is said to have 100% SOC while 0% SOC means the battery is completely depleted. It is typical for batteries to be operated only in a certain range of SOC for safety and to reduce effects of degradation, for instance electric vehicles may only be cycled between 20% and 100% SOC [27]. Another key term is depth of discharge or DOD, which describes the difference between the max and min SOC for a cycle [26]. For instance, if a battery is cycled between 90% and 40% SOC we would say the depth of discharge is 50%. To describe the rate of battery cycling the term c-rate is used where the c-rate is the rate of battery charging or discharging in amps relative to the battery's capacity

in amp-hours [26]. For instance, a 1C discharge of a 20 Ah battery means the current is 20 amps and the battery will go from 100% to 0% SOC in one hour. A 2C discharge rate yields a current of 40 amps and the battery can be fully discharged in 30 minutes.

2.1.2 *Heat and Temperature in Lithium-ion Batteries.*

Temperature has a significant effect on the performance of lithium-ion batteries in terms of efficiency, lifetime, and safety [22, 28]. Thus thermal analysis and management becomes essential for most lithium-ion systems [29]. As this thesis will focus heavily on thermal management design and analysis, this section will give a cursory introduction to heat generation and thermal management of lithium-ion battery packs.

Batteries generate heat through several mechanisms. A few of the main mechanisms of heat generation are [2, 24]:

1. ***Joule heating:*** heat generated by ohmic losses.
2. ***Reaction heat:*** reversible work and entropic heat from electrochemical reactions.
3. ***Heat of mixing:*** heat released or consumed due to non-uniform reaction rates across the battery.
4. ***Heat of phase change:*** heat from material phase changes.

It is common to simplify the heat generated in batteries to Equation 1 which focuses on the two dominant forms of heat generation, which are joule heating and reaction heating [24, 28, 30].

$$\dot{Q} = \dot{Q}_{joule} + \dot{Q}_{reaction} \quad \mathbf{1}$$

Joule heating is the heating caused by impedance on charge carrying particles and can be expressed by Equation 2, where I is current in amps and r is internal resistance of the battery in ohms.

$$\dot{Q}_{joule} = I^2 r \quad \mathbf{2}$$

Reaction heat is a result of the exothermic or endothermic reactions that happen during the intercalation process [30]. Unlike joule heating, it can be negative, indicating an endothermic reaction. Reaction heat can be expressed as Equation 3, where I is current in amps, T is temperature in kelvin, and $\frac{dU_{ocv}}{dT}$ is the entropic heat coefficient in volts per kelvin. Note that the sign of reaction heat is flipped between charging and discharging (I is positive for discharging, negative for charging).

$$\dot{Q}_{reaction} = -IT \frac{dU_{ocv}}{dT} \quad \mathbf{3}$$

Equations 2 and 3 can be added together to form equation 4 for the total heat generation in the battery.

$$\dot{Q} = I^2 r - IT \frac{dU_{ocv}}{dT} \quad \mathbf{4}$$

Notice that joule heating is proportional to current squared while reaction heat is only proportional to current. For this reason, joule heating tends to dominate for charging and discharging at high current while reaction heat can dominate at lower currents [2, 30].

Temperature has various effects on lithium-ion batteries that often make thermal management a priority [2, 24]. This can include cooling to deal with the heat generated by the battery or heating the battery if it is too cold. One of the most important thermal concerns for lithium-ion batteries is thermal runaway [2, 23]. Thermal runaway happens when a battery's temperature goes beyond some unsafe point (70°C to 100^{+}C [24]), which triggers various exothermic reactions. Heat from each reaction fuels the next and creates a runaway reaction that can lead to the cell catching fire and possibly exploding [28]. If power load on a battery is high enough to make thermal runaway a concern, then thermal management systems are typically put in place to remove heat from the battery. Additionally, controls will usually cut off power to or from the battery if the temperature gets too high [2].

Another reason temperature is important for lithium-ion batteries is its effect on ageing of the cell. Many of the mechanisms that cause a lithium-ion cell to lose energy and power capacity are irreversible side reactions. The rate of these reactions increases with increased temperature and thus the rate of fade for the batteries is higher at elevated temperatures [2]. These mechanisms of battery aging and their dependence on temperature are covered in more detail in the next section.

There are also reasons to avoid keeping a battery from getting too cold. For one, a decrease in temperature increases the impedance on ionic conductivity and diffusion [28].

This leads to an increase in internal resistance with an associated drop in battery efficiency as well as a drop in capacity [2]. Another reason to avoid keeping lithium-ion batteries at cold temperature is lithium plating. This phenomenon mostly occurs when rapidly charging at cold temperatures, which causes lithium metal to form on the negative electrode in branching shapes called dendrites [2]. If the dendrites grow long enough to short the battery they could lead to sudden and possibly catastrophic failure of the battery. This will also be discussed in greater detail in the next section.

All these factors together make thermal management systems essential for most battery systems to maximize safety, lifetime, and performance [2].

2.1.3 Degradation of Lithium-ion Batteries

Like most physical systems, lithium-ion batteries degrade overtime. Because we are interested in the performance and lifetime of second-life batteries we are concerned with degradation that happens not only during the battery's first life in the vehicle, but also during its second life as stationary energy storage. For this reason, it is important to get a general background on mechanisms and trends associated with battery degradation.

Degradation in lithium-ion batteries is associated with performance losses in both capacity and power capabilities [2, 28, 31]. This occurs through several mechanisms that can depend on the battery chemistry such as the electrode materials. Degradation mechanisms can either progress with time (called calendar mechanisms), or can progress with cycling (called cycling mechanisms), or can be some combination of the two [2].

One common and typically dominant mechanism for degradation is the loss of lithium ions in a side reaction that creates what is called the solid electrolyte interphase (SEI) [2]. The SEI is a solid layer that is deposited on the surface of the negative electrode and degrades the battery both by consuming lithium ions so that they can no longer be used to carry charge, and by creating additional impedance on the flow of charge which increase battery resistance and reduces power capability [2]. This mechanism effects chemistries using graphite negative electrodes and because, most electric vehicles use graphite anodes this mechanism is present in most EV batteries [32]. The process of SEI formation is diffusion limited and thus is considered mostly a calendar mechanism where the rate of the associated degradation typically decreases with time [2]. However, several additional phenomena can increase the rate of SEI formation. One is crack formation in the SEI layer caused by expansion and contraction in the battery during cycling, exposing new area for SEI formation and speeding up degradation [2]. Another is when parts of the positive electrode migrate to the negative electrode and act as a catalyst for additional SEI growth [2]. shows an example were manganese from the positive electrode created SEI growth around it. These phenomena can give SEI formation a slight cycling dependence [33]. Figure 7 illustrates the process of SEI growth on the negative electrode (graphite) in different stages. Finally, SEI growth is a chemical reaction and thus its rate increases with increased temperature, this is one of the reasons why higher battery temperature leads to greater rate of capacity degradation [2].

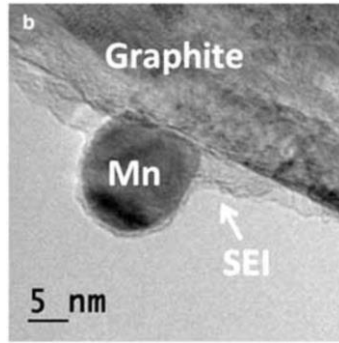


Figure 6 – Manganese from positive electrode catalyzing SEI growth on negative electrode [2]

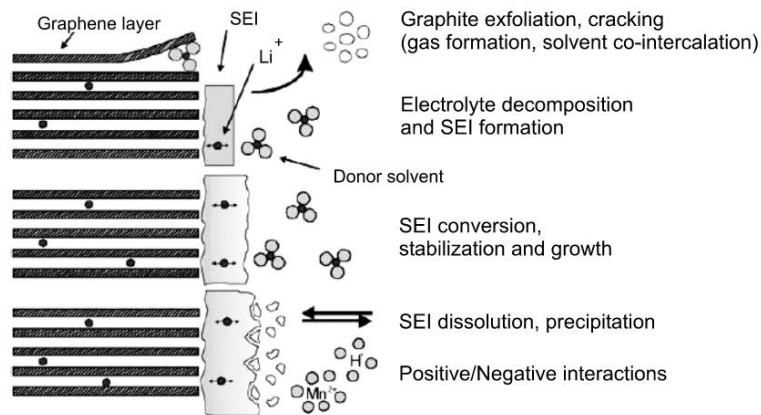


Figure 7 – SEI formation and growth process [2]

Another common mechanism for battery degradation is loss of active sites in the electrodes. The amount of lithium ions an electrode can accept is a property of the material used, and this directly correlates to the amount of charge that can be stored by the battery. Both electrodes can lose active sites over time due to things like mechanical damage from contraction and expansion in cycling, however the positive electrode can also be degraded due to structural disordering and dissolution [2].

An additional degradation mechanism, that can also be a safety concern, is lithium plating. As mentioned before, this is when metallic lithium begins to plate on the negative electrode, usually during fast charging at cold temperatures. This metallic lithium grows in the form of dendrites as shown in Figure 8. Once lithium plating occurs, some of this lithium can be reversely put back into cycling but the rest is irreversibly lost and thus reduces the amount of total cyclable lithium and reduces capacity. Of greater concern is if the dendrites grow long enough to break the separator in between the electrodes, where the dendrite can cause an internal short. In most cases this will lead to a cell fault which will drastically reduce pack capacity or render the whole pack unusable [23]. In rare cases however, if the dendrite is thick enough, it may cause rapid heating of the battery that can lead to thermal runaway, although such cases are rare [2].

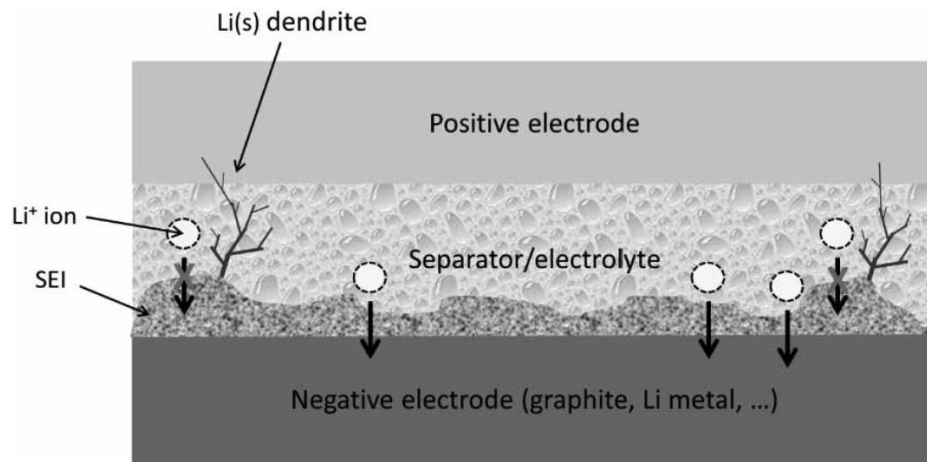


Figure 8 – Example of lithium plating with dendrite formation [2]

There are many other ageing mechanisms that may be present that we will not cover in detail. Though it is worth noting that there are mechanisms such as gas generation in the battery and decomposition of adhesives and binders that can lead to rapid drops in battery capacity especially late into a batteries life [2].

When all ageing mechanisms are combined, the capacity life of a lithium-ion battery can be separated into 3 general stages [2]:

1. An initial gain in capacity at beginning of life as some trapped lithium is freed during the first few cycles.
2. A decelerating decline in capacity typically dominated by SEI formation.
3. An accelerating decline in capacity toward end of life as there is shift in the dominant mechanism of degradation.

A hypothetical example of these stages is shown Figure 9. Depending on the construction, environment, and usage of the battery, not all these mechanisms will necessarily be present. For instance, for situations with only mild cycling of the battery, the region of accelerated fade may not be present. Understanding where these regions present in a battery's life is important for second-life batteries as a battery that only sees decelerating fade will have a much longer second life than one which has accelerating fade.

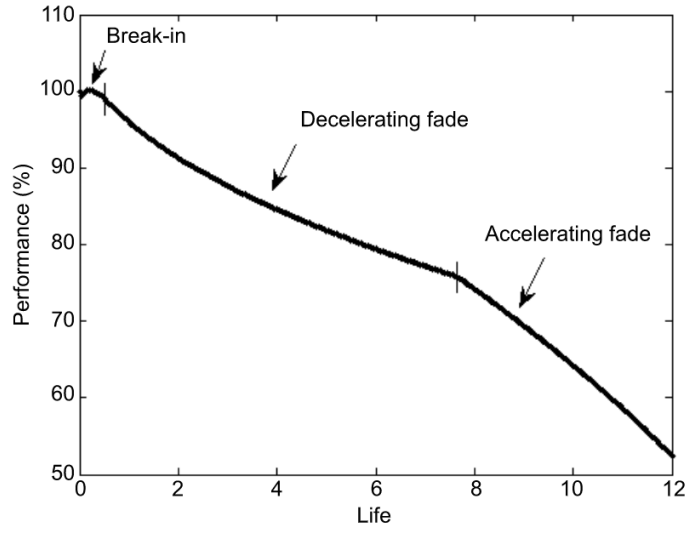


Figure 9 – Example of the possible stages of degradation for lithium-ion cells [2]

2.2 Literature Review

In this section we review the recent literature on second use batteries for home energy storage and vehicle charging. This includes simulation-based studies and experimental studies which analyze the economics, lifetime, environmental benefit, and cost of these systems.

2.2.1 *Simulation Based Studies*

A multi-faceted study by Neubauer et al. estimated the amount of capacity remaining at the end of vehicle life by simulating electric vehicle drive cycles with battery degradation for several locations across the US [4]. They found that calendar ageing was dominant over cycling aging during vehicle life and that loss of capacity ranged from 25-30% for battery electric vehicles (BEVs) and 30-33.5% for plug-in hybrids (PHEVs). Vehicles at the lower end of this range were from colder climates like Minneapolis, and vehicles at the higher end were from hotter climates like Phoenix. Similarly, resistance increased over vehicle life 27-35% for BEVs and 56-65% for PHEVs. They then used similar methods to estimate second use lifetime in a peak shaving application where the batteries discharge 2 hours during the day and charge 6 hours at night. They found that the second use lifetime was highly sensitive to the depth of discharge chosen, with lifetimes varying from 25 years at 40% DOD to 5 years at 70% DOD. Additionally, they generated an in-depth estimate of the cost of repurposing battery modules and the likely selling price of these repurposed batteries. They found the cost of repurposing the modules to be between 25 and 50 \$/kWh

while predicting they would be sold on the market at between 44 and 180 \$/kWh depending on the competing price of new batteries.

Kirmas and Madlener studied the economic viability of using second-life EV batteries for residential energy storage by simulating their use for households in South Germany [6]. They modeled battery temperature with a lumped capacitance model assuming only passive cooling, and modeled degradation with a semi-empirical model from literature. Data was collected for household demand, solar irradiation, and ambient temperature for Stuttgart, Germany. They calculated the profit based on battery prices between 34 and 117 €/kWh and increased electricity prices between 2% and 6% per year. They found most scenarios to be profitable with a NPV between -326 and 825 € for a 10-year lifetime depending on the electricity and battery price, with the NPV being most sensitive to the feed-in tariff chosen. Additionally, they found that the energy capacity reduced from 80% of original capacity to roughly 60% over 10 years, while internal resistance doubled.

Heymans et al. analyzed the economics of second use batteries for load shifting in residential applications [7]. This included shifting demand from high cost times to low cost times but did not include PV generation. They simulated the performance of a Chevy Volt battery with 80% capacity remaining providing energy storage for a home in Ontario, Canada. The analysis did not include effects of temperature and assumed no degradation in second life. They found the return-on-investment to be marginal with a maximum profit of \$38 annually for a home with a higher than average electricity load. They conclude that additional economic incentives would need to be provided to make second use batteries for residential storage feasible, such as changes to the electricity pricing structure.

Assunção et al. estimated the performance of using second-life batteries to increase the utilization of rooftop solar [34]. They examined using both used Nissan Leaf and Citroen C0 batteries with 70% remaining capacity for homes in Portugal. They also included a semi-empirical model of degradation assuming an average temperature of 25°C. Both batteries lead to a roughly 80% reduction in grid use and lead to an energy savings of around €290 per year. The calculated payback period was around 9.5 years for the Leaf battery and 6.1 years for the C0 battery, which was less than the estimated lifetime of 13 and 11.5 years respectively.

Saez-de-Ibarra et al. conducted a study to determine the optimal storage capacity of a second use battery for residential use in Spain to generate the highest electricity savings [35]. They found the optimal storage size to be 1.8 kWh paired with a 1 kW PV system, generating a net profit of around €17 per month. The optimization method likely produced such a small system size to target the demand charge for peak power consumption. Such a size would not be suitable for back-up power.

Ahmadi et al. simulated battery degradation in LiFePO cells for both first use in a vehicle and second use in a stationary storage application providing one cycle per day at 75% DOD [36]. They found that the capacity remaining at the end of 8 years of vehicle life was 80%, and 65% after 10 years of second use. In an separate study Ahmadi et al conducted life-cycle analysis of re-using EV batteries for peak shaving applications and found that it leads to a 56% reduction in the net life-cycle CO₂ production of the EV batteries [37].

2.2.2 *Experimental Studies*

Several studies also used experimental methods to analyse second use batteries. This includes prototypes of home energy storage devices with second use cells, experimental studies of second use lifetime, and one study of a prototype vehicle charger using second use batteries.

Martinez-Laserna et al. conducted an experimental study on 20 Ah NMC cells to simulate degradation during both first and second life [38]. This included accelerated aging testing to simulate electric vehicle driving in first life, and either grid level or residential level use in second life. They found that many cells reached a point of accelerated aging either at end of first life or during second life and the aging did not slow down with lower C-rate once the accelerated ageing fade had started. They conclude that the remaining capacity of the cells is less important to second use lifetime than how close the cell is to reaching the point of accelerating fade. Thus, they stress the importance of collecting data on the cells first life to best estimate this phenomenon.

Tong et al. (2015) created a prototype second use battery energy storage system for a single-family home in California [39]. They produced an active battery balancing and management system to construct the device from 15 modules of varying remaining capacity. They demonstrated that the device was able to reduce the grid dependence of the home by 81% when paired with a 2.2 kW PV array.

Li et al. presented a methodology for generating a condensed lifetime testing profile for second use EV batteries in residential storage applications [40]. They demonstrate this method with a second use plug-in hybrid battery from a Ford C-max Energi, by simulating

15 days of use and found no variation in capacity or resistance. They have not yet published any results from longer testing periods.

Tong et al. (2013) created a prototype vehicle charging station using second-life EV batteries that were charged with a PV array [41]. The device had 139 LiFePO cells with a capacity of 13.9 kWh and charged an Electric vehicle through 1.5 kW AC power. The system was demonstrated to be effective and used to validate a model which predicted such a device could deliver about 10 kWh of vehicle charging per day at an estimated 50% cost reduction compared to a similar system with new batteries.

2.2.3 Discussion

In conclusion, several studies of reused batteries for home energy storage show that they can effectively reduce reliance on the grid and reduce energy costs, however the net profit is typically minimal. This supports the effort of this study to generate additional value from a second use battery home storage device by adding vehicle fast charging. Only one study was found about reusing EV batteries for vehicle charging, and that study did not examine fast charging, or pairing the system with home energy storage, which highlights the novelty of our study. Additionally, studies that modeled battery degradation with semi-empirical models found rather mild degradation of the battery in a second-life scenario. However, experimental testing by Martinez-Laserna et al. showed that second-life could be significantly reduced if the batteries reach a point of accelerated fade. This adds significant uncertainty to the lifetime of second use batteries which merits further study and should be considered when analyzing the results of this study.

2.3 Review of Industry

2.3.1 *Currently Available Products for Home Energy Storage*

There are several products currently on the market that offer consumers home energy storage using new lithium-ion batteries. Three of the main manufacturers of these systems are Tesla, LG Chem, and Sonnen [42].

Tesla offers a product called the Powerwall (Figure 10) which is currently in its second generation and offers 13.5 kWh of useable energy storage, a peak power output of 7 kW, 90% round trip efficiency, and a 10 year warranty [43]. A single unit including installation can cost as much as \$11,500 [42].



Figure 10 – The Tesla Powerwall 2 [43]

Unlike the first generation Powerwall, the Powerwall 2 AC comes with an internal inverter and the system is only AC coupled meaning there is no direct DC connection to solar panels [43]. It can either be configured to power the whole home during an outage or only certain appliances by creating a sub-panel just for back-up loads. The configuration for partial home backup is shown in Figure 11.

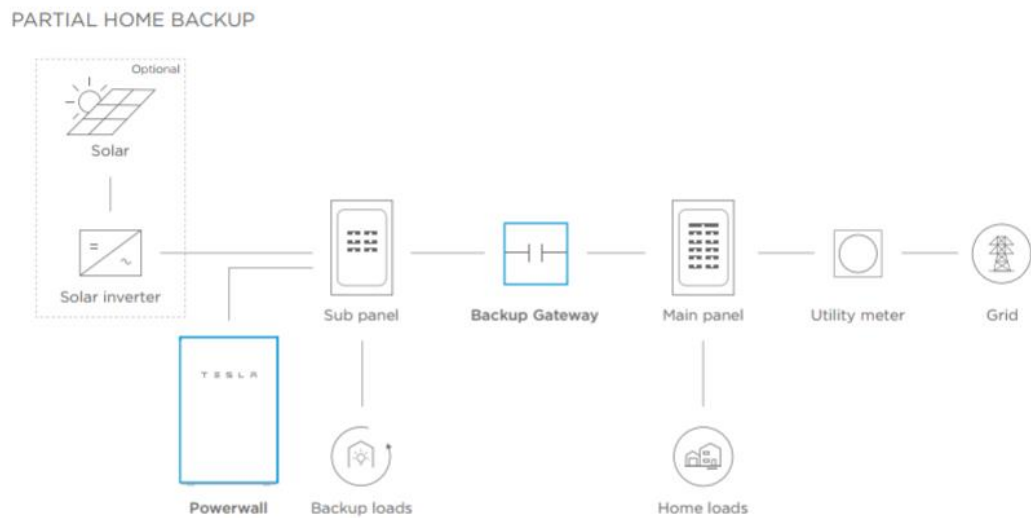


Figure 11 – Tesla Powerwall 2 installation configuration for partial home backup [43]

LG Chem offers similar home energy storage products with its RESU line of battery storage systems. They offer low voltage and high voltage systems, ranging from 2.9 to 9.3 kWh of usable energy [44]. Figure 12 shows the two-high voltage RESU models available. Unlike the Tesla Powerwall 2, the RESU battery needs to be paired with an inverter from a third party [44].



Figure 12 – High voltage LG Chem RESU residential storage products and specs [44]

Sonnen is a German company that has recently begun operating in the US and offers a home storage battery called the sonnenBatterie Eco. It includes up to 16 kWh of storage with a peak output of 8 kW and a 10-year warranty [45]. The system starts at \$9,950 including an inverter but without installation [42]. Figure 13, shows the sonnenBatterie Eco installed in a home.

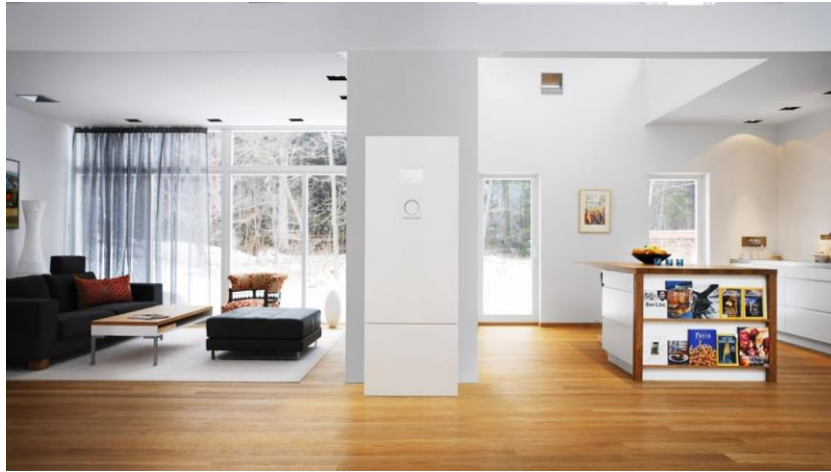


Figure 13 – The sonnenBatterie Eco [45]

2.3.2 Industry Projects for Home Energy Storage with Reused EV Batteries

There are several automakers testing reused electric vehicle batteries as residential energy storage. Nissan partnering with Eaton are currently accepting pre-orders for a product called XSTORAGE for home use (Figure 14) [46]. The consumer can choose between two options for the product, one is composed of new batteries and the other is composed of second-life Nissan Leaf batteries [47]. The second-life option provides 4.2 kWh of energy with a peak power of up to 6 kW [47].



Figure 14 – Nissan's XSTORAGE which is expected to have an option with reused Leaf batteries [46]

Similarly, BMW announced in 2016 a plan to sell reused i3 batteries as home energy storage with a capacity between 22 and 33 kWh (Figure 15) [48]. To date the product is not currently for sale.



Figure 15 – BMW's battery reuse project for home energy storage with i3 battery packs [48]

Finally, French automaker Renault announced in 2017 a partnership with Powervault to provide home energy storage with second-life batteries and have placed test products in 50 households [49].

In conclusion, these projects show that companies are interested in the reuse of batteries for home energy storage and that these products could be on the market soon. However, it is important to note that none of these systems are intended to provide vehicle charging, like we are proposing.

2.3.3 Industry Projects for DC Fast Charging Stations with Reused EV Batteries

There are some industry projects that involve using second-life batteries for DC fast charging stations at commercial locations. Renault announced in 2016 a partnership with UK based company Connected Energy to provide used EV batteries for fast chargers supplying 50 kW [18]. The system, named E-stor, is shown in Figure 16. Aside from Renault, there are also several other companies proposing to use second-life EV batteries for DC fast charging including EVgo and Freewire [19] [20].



Figure 16 – E-stor DC fast charging system with second life Renault batteries [18]

2.4 Background on Selected Electric Vehicles

The electric vehicles chosen in this study to analyze battery reuse are the Chevy Volt, the Nissan Leaf, and the Ford Focus Electric, all of which being from the 2013 model year. These vehicles were chosen for the following reasons:

1. Data is more readily available for these vehicles compared to others
2. These vehicles will reach their end of life within 5-10 years of the date of this study, meaning they will be some of the first available for second use.
3. More is known about how these vehicles will age because they have already been on the road for about 5 years.
4. The selections include different types of electric vehicles including both plug-in hybrid vehicles (PHEVs) and battery electric vehicles (BEVs).
5. The selections include both liquid cooled and air cooled thermal management strategies.

In sections 2.4.1 through 2.4.3 we will cover each of these batteries in depth, including general specifications like capacity, cell composition, and thermal management systems. In section 2.4.4 we summarize the parameters for these vehicles collected from literature and laboratory measurements that are necessary for our analysis.

2.4.1 2013 Chevy Volt Battery Pack

The 2013 Chevy Volt is a plug-in hybrid vehicle (PHEV), which means it contains both a gasoline and electric motor with a battery that can be charged by plugging into a wall outlet or charging station. The 2013 Volt has a Gen 1 Volt Battery Pack with 16.5

kWh of energy capacity [50] [51]. Figure 17 shows the Gen 1 Chevy Volt pack and Figure 18 shows the packs location in the vehicle.



Figure 17 – The Chevy Volt battery pack [50]



Figure 18 – Chevy Volt showing location of battery pack and motor [50]

The battery pack is made up of 288 lithium-manganese-oxide (LMO), pouch shaped cells as shown in Figure 19. These cells are grouped in to modules, which are then collected into a single pack.



Figure 19 – A Chevy Volt pouch cell [52]

The Volt battery pack utilizes an active liquid cooled thermal management system [51, 52]. 50/50 Ethylene-Glycol coolant is pumped through cooling fins with multiple channels which contact the largest face of the cell, with one cooling fin per every two cells [52]. Each cell is provided coolant in parallel through a manifold and because the pressure drop in the cells is much higher than that in the manifold, the coolant flow is uniformly distributed amongst the cells [52]. Figure 20 shows a single cooling fin along with the repeating frames which hold the cells and the manifold for porting coolant to and from each fin.

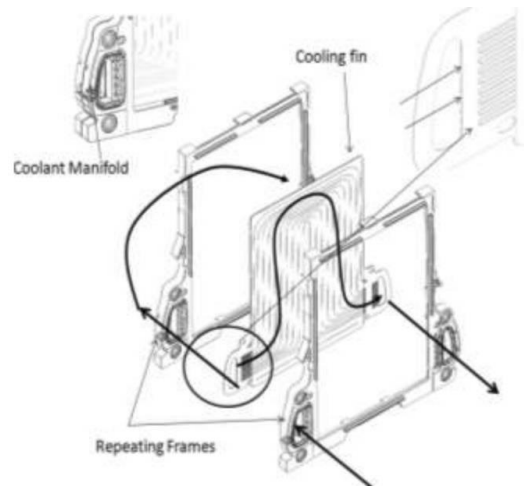


Figure 20 – Chevy Volt cell cooling fin and manifold

The battery is connected to a larger coolant circuit as shown in Figure 21, that removes or adds heat to the liquid coolant [2]. To reduce the coolant temperature the coolant can either be ported to the cars radiator to exchange heat with the ambient air, or heat can be removed via the vehicles refrigerant loop via a liquid to liquid heat exchanger [2]. To heat the coolant, the vehicle has a 1.6 kW heater for operating in cold temperatures [52].

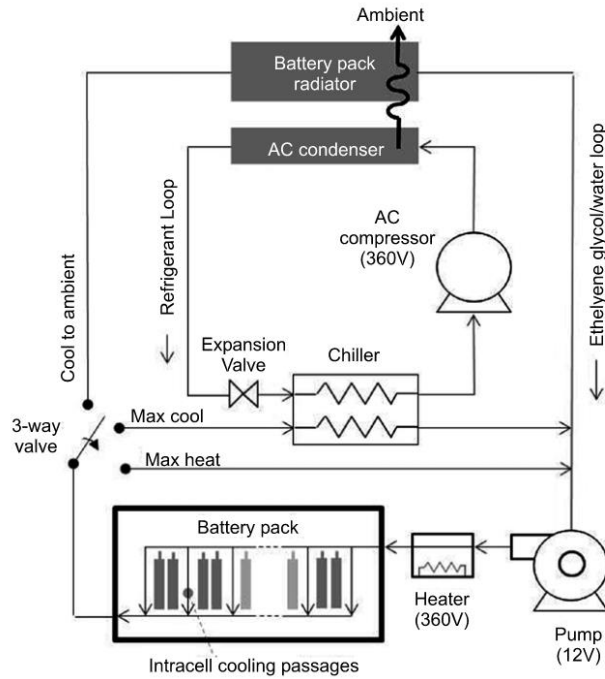


Figure 21 – Chevy Volt cooling circuit [2]

We purchased a single cell with a cooling fin for a 2013 Chevy Volt from a salvage yard. Figure 22 shows the cell in its plastic housing (Figure a), and the aluminum liquid cooling fin (Figure b). We used this sample cell to measure the dimensions and mass of the cell and fin.

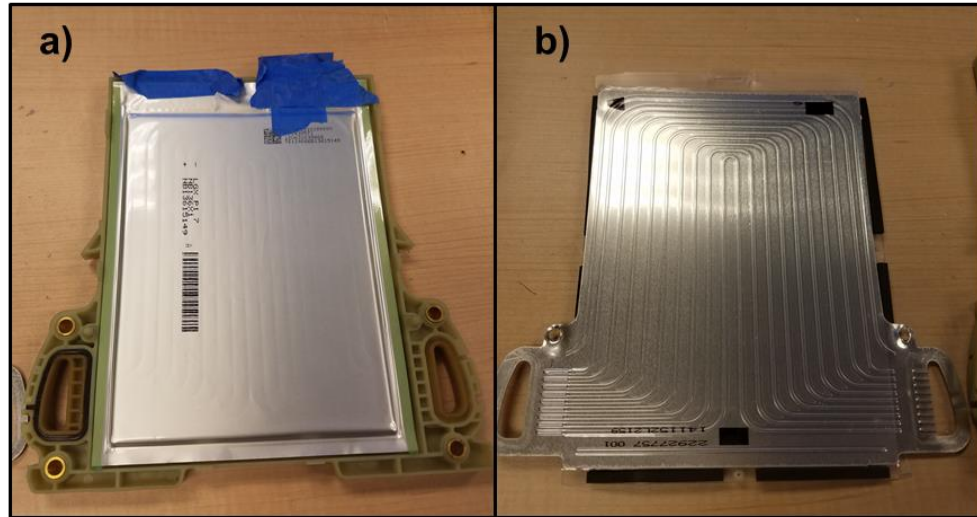


Figure 22 – a 2013 Chevy Volt cell inside its plastic frame (a) and the adjacent liquid cooling fin (b)

2.4.2 2013 Nissan Leaf

The 2013 Nissan Leaf is a battery electric vehicle (BEV) meaning the car is solely battery powered with no internal combustion engine. The battery pack has 24 kWh of capacity and 84 miles of range [51]. Figure 23, shows the Nissan Leaf battery location inside the vehicle.



Figure 23 – Nissan Leaf with battery pack location shown [53]

The battery is composed of 192 lithium-manganese-oxide (LMO) cells [51]. Four cells are combined to form a module which are enclosed in hard aluminium case. 48 of these modules are stacked to form the whole battery pack as shown in Figure 24.

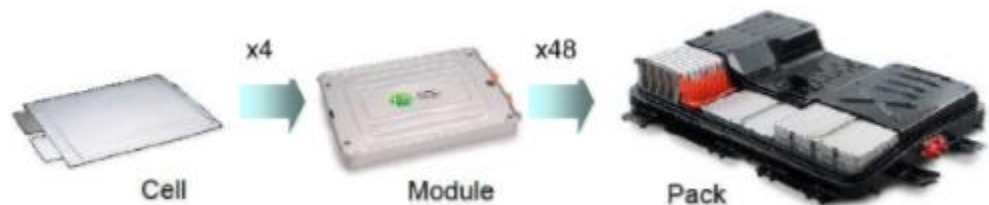


Figure 24 – Cell, module, and pack in Nissan Leaf [54]

The pack does not incorporate any active liquid or air cooling but instead relies on passive cooling of the battery [54]. The cooling is referred to as “passive” in that the pack is completely sealed and there is no air exchange between air inside and outside the battery,

however an internal fan circulates air inside the pack to aid in heat transfer and thermal balancing of the cells [55] [56].

Like the Volt, we purchased a module from a 2013 Nissan Leaf battery from a salvage yard. Figure 25 shows the module with its hard aluminum casing both on and with the top face of the casing removed to show the cells inside. The blue film seen in Figure b is a plastic spacer which is placed between each cell and between the cells and the case. The cells appear to be glued together in this cell-spacer-cell formation.

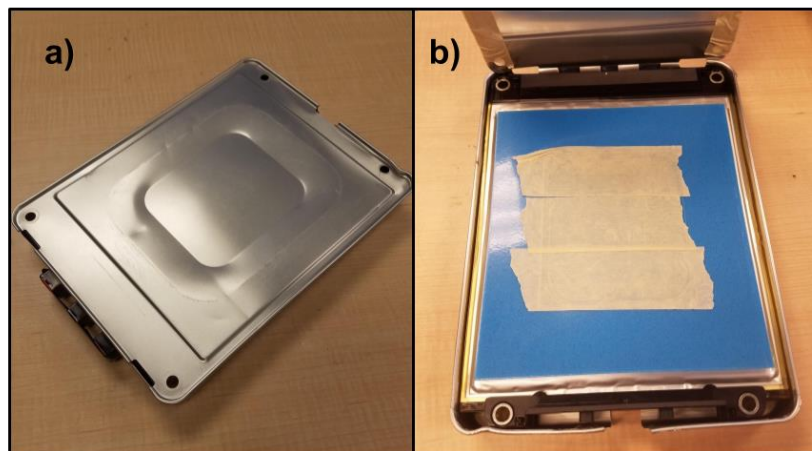


Figure 25 – The purchased module from a 2013 Nissan Leaf (a) and the same module with the front face of the aluminum cover removed to show the cells (b).

Examining the module, it seems to be constructed to accommodate some amount of air flow. Figure 26a shows what we assume to be the entry and exit points for air flow to the module and Figure 26b shows the hypothesized air flow through the module which

seems to only pass over the sides of the cell, as there is no air gap between the cells. This is only based on conjecture as we were not able to find any literature to support this.

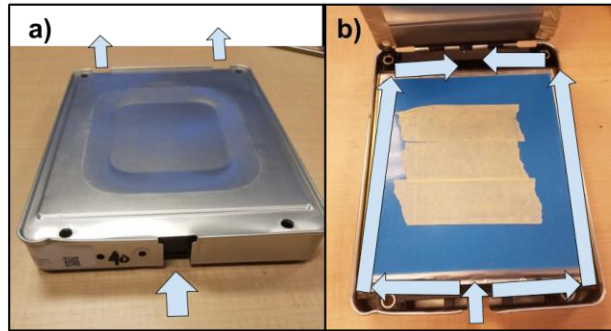


Figure 26 – Hypothosised air flow in and out of module casing (a); hypothesised air flow around edges of cells inside module (b)

2.4.3 2013 Ford Focus Electric

The Ford Focus Electric is also a battery electric vehicle like the Nissan Leaf. It has a 23 kWh battery and 76 miles of electric range [51]. Figure 27, shows the location of the battery pack in the rear of the vehicle behind and under the rear passenger seats.



Figure 27 – Ford Focus Electric with motor and battery pack shown [57]

The battery is composed of 430 LMO cells with 5 parallel strings of 86 cells in series [51]. Like the Chevy Volt, the Ford Focus Electric utilizes active liquid cooling and heating of the battery cells [51].

Unlike the Volt and Leaf, we were not able to find a sample of the Focus battery and we were not able to find references for the geometry of the cell, cooling fins, or cooling circuit. So, for our analysis we assume that the cells and cooling configuration is similar to that found in the Chevy Volt as seen in Figure 20 through Figure 22.

2.4.4 Summary of Battery Parameters

For our analysis, necessary parameters for the EV battery packs were found for both the pack and cell levels either from reference or measured directly from the samples collected.

Table 1 and Table 2 summarize these parameters on the pack and cell level respectively. We were unable to find references for some of these parameters so some were either estimated (marked “*”) or calculated (marked “+”) based on knowledge of other parameters. The parameters that come from estimates are subject to the highest amount of uncertainty and are treated as such in later analysis. Examples of these unknown parameters include the dimensions and mass of the Focus cell which was assumed to be the same as the Volt cell because they have similar capacity, and the mass of the Focus and Volt cells which were estimated by assuming the same energy density as the Leaf cell.

Table 1 – Summary of battery pack parameters for selected EV’s

<i>Parameter</i>	<i>Unit</i>	<i>2013 Ford Focus Electric</i>	<i>2013 Chevy Volt</i>	<i>2013 Nissan Leaf</i>	<i>Source</i>
Amp-hour capacity of pack	[Ah]	75	45	66.2	[51]
Energy capacity of pack	[kWh]	23	16.5	24	[51] for all, [52] for Volt
Mass of pack	[kg]	302.6	197.3	290.3	[51]
Volume of pack	[L]	268.3	153.8	350.6	[51]
Internal resistance of pack	[ohms]	0.065	0.098	0.111	[51]
Cooling type	-	Liquid Fin Cooling	Liquid Fin Cooling	Active – Air Cooled within Sealed Pack	[51] for all, [52] for Volt
Max cell voltage	[V]	4.2	4.15	4.2	[51]
Min cell voltage	[V]	3	3.00	2.5	[51]
Nominal system voltage	[V]	318.2	355.2	364.8	[51]
Number of cells per pack	-	430	288	192	[51]
Number of cells in series	-	86	96	96	[51]
Number of cells in parallel	-	5	3	2	[51]

Table 2 – Summary of battery cell parameters for slected EVs

<i>Parameter</i>	<i>Unit</i>	<i>2013 Ford Focus Electric</i>	<i>2013 Chevy Volt</i>	<i>2013 Nissan Leaf</i>	<i>Source</i>
Cell chemistry	-	LMO	LMO	LMO	[51]
Nominal cell voltage	[V]	3.7	3.7	3.7	[51]
Length of cell	[mm]	200 *	200	290	Volt and Leaf were measured in lab, Focus was assumed same size as Volt, Leaf also from [54]
Width of cell	[mm]	145 *	145	216	
Depth of cell	[mm]	5.5 *	5.5	7.1	
Internal resistance of cell	[ohms]	0.0038 ⁺	0.0031 ⁺	0.0023 ⁺	= (N _{parallel} / N _{series}) * r _{pack}
Amp-hour cell capacity	[Ah]	15 ⁺	15 ⁺	33.1 ⁺	= (1/N _{parrallel}) * Cap _{pack}
Mass of cell	[kg]	0.359 *	0.359	0.787	Volt and Leaf were measured in lab, Focus was assumed same mass as Volt, Leaf also from [54]

CHAPTER 3. METHODS

3.1 Summary of Methods

In this chapter, we will summarize the variety of methods that we adopted to analyze the performance of our concept second-life home battery storage system. We start in Section 2.1 by outlining the general layout of the design and the components necessary for the device to achieve the desired functions of providing solar storage, load shifting, back-up power, and fast vehicle charging for a single-family home. We also outline the various thermal management strategies that could be adopted and how they would operate.

With the general design set, in Section 2.2 we create several thermal modeling techniques for predicting the temperature of the battery cells under different cycling rates and thermal management methods. This includes a heat generation model for the cell, an isothermal model for adiabatic conditions and passive thermal management, and a multi-nodal model for active thermal management.

In section 3.4 we cover the electrical model for the batteries which includes SOC and voltage estimation. This will be paired with the thermal models to calculate battery SOC, efficiency, and the relationship between battery current and power at load.

In section 3.5 we outline the fluid analysis conducted on the flow required for thermal management. This includes pressure drop calculations which we use to estimate the power consumption of the thermal management systems.

Section 3.6 details the degradation model adopted from literature for LMO cells. The model includes capacity and cycling degradation effects on capacity. Adaptations to the model are made to calculate the expected lifetime of our system and the effects of different thermal management strategies.

In Section 3.7 we develop a model to simulate the devices performance under realistic situations for three sample houses with rooftop solar and an electric vehicle in the US cities of Phoenix, Arizona; Chicago, Illinois; and Los Angeles, California. These cities were chosen because they represent a wide variety of climates, household energy use, and utility rates. First, we create profiles for expected electricity load, solar generation, and electric vehicle charging. Then we define control algorithms to define when the battery charges and discharges and when to run the thermal management system. We then simulate the systems performance by utilizing our thermal and electrical models that we created previously. From the results we estimate benefits provided to the user in terms of increased energy savings, decrease in grid consumption, the amount and rate of DC fast charging provided to the vehicle.

Finally, Section 3.8 outlines how uncertainty in the input parameters was defined and the justifications for doing so. This includes uncertainty in the health of all three of the selected EV batteries including energy capacity and resistance at end of vehicle life, which were estimated based on information collected from vehicle warranties, test data, and literature. Additionally, uncertainty in thermal parameters such as mass, heat capacity, convection coefficients, and thermal conductivities was also included.

3.2 Proposed Device

This section will cover the conceptual design of the device including the necessary power electronics components and the different thermal strategies that can be adopted. Certain parts of the design will change based on which vehicle's battery is being used, however most of the components will remain constant. The components that will be varied most in this study will be the thermal management components and the components necessary for DCFC.

3.2.1 General Design

In designing our device, we first assume that it will be composed of one complete battery pack rather than a subset of modules or a combination of multiple packs. To combine EV modules or packs with various degrees of age would require additional battery balancing circuits or a massive sorting operation to pair batteries up with those of similar age. Also, keeping a pack together rather than breaking it into modules allows for a greater number of components from the original pack to be reused, such as electrical and cooling fluid connections as well as controls and balancing circuits. Thus, we assume that using a single EV pack to be the most economical way to reuse the batteries. Several studies in literature also make this same assumption [7] [58] and battery reuse projects by BMW seem to use only one vehicle pack as well [46, 48].

Next, we add additional components to the battery pack such that it will be able to provide a single-family home with the following core functions:

1. DC fast charging for one electric vehicle
2. Storage of rooftop solar generation for increased energy savings and reduced grid use
3. Energy shifting and demand charge reduction for decreased energy costs
4. Provide back-up power to house in the case of an outage

This includes the various power electronics and controls which will be described in the following sections.

We then assume the battery and additional components will be repackaged into a frame and installed in a single-family home where it will be connected to a rooftop photovoltaic system, the house loads, and the grid. We assume the device will be placed in a garage so that it can provide fast charging for an electric vehicle.

3.2.2 Electrical Design

To reuse electric vehicle batteries for home energy storage and vehicle fast charging will require various power electronics and controls components to interface the device with household loads, rooftop solar installations, the utility grid, and an electric vehicle. These components and their expected configuration are covered in this section.

3.2.2.1 Components for Solar Storage

The main component that is necessary for pairing a rooftop solar installation with the battery is a maximum power point tracking solar charge controller or MPPT. An MPPT

is a DC/DC converting device that helps to capture the maximum amount of solar power and use it to charge a battery. It is referred to as a maximum power point tracker because there is a voltage range at which PV modules are most efficient and the MPPT attempts to track this voltage point to ensure maximum power [59]. In addition to an MPPT, wired connections will need to be made between the MPPT and the energy storage system for both the transmission of power and for communication.

3.2.2.2 Components for Connection to Home and Grid

To power the AC loads of the home and to export power to the grid will require a bidirectional AC/DC inverter. We require the inverter to be bidirectional in the sense that power can flow in both directions. This will allow for the storage device to discharge to the home or grid, while also being able to charge from the grid if necessary. In addition to the inverter, the device will need a meter to measure electricity demand from the house and likely an internet connection to gain information on current energy prices or price and weather predictions for more advanced controls. This will allow the device controls to choose the best times to charge and discharge. However, the simplified control algorithm chosen in this study does not use this information.

3.2.2.3 Components for Back-up Power

Based on research of current home energy storage installations, providing back up power may require setting up a back-up load panel that is different from the normal home load panel [43]. The back-up load panel provides power to only the critical appliances in the home. Additionally, some sort of low voltage energy storage, such as an uninterruptible power source (UPS) will be necessary to run the system controller in the event of an outage.

The UPS will also contain an inverter that converts AC power to low voltage DC for running the thermal management system during normal operation. The thermal management system is not expected to run during back-up mode as power draw is relatively low.

3.2.2.4 Components for Vehicle Fast Charging

To port energy from the home storage battery to a vehicle battery at the proper rate will require a high-power DC/DC converter. Both the home battery voltage and vehicle voltage would change during the charging process as the SOCs rise or fall, and the device would need to vary the voltage supplied to the vehicle to provide a constant charging current. The DC/DC converter would also need to be rather large to handle high current, with operating power on the order of 20-100 kW. Additional to the DC/DC converter, the home storage device controller would need to communicate with vehicle to control the flow of power.

3.2.2.5 Full Electrical System Configuration

Figure 28 is a diagram showing the electrical topology of the system. Orange lines represent high voltage DC connections, green represents low voltage DC, and blue is AC power. Not displayed is the communication connections between the device controller and the other components for legibility. We can see that the battery through the bidirectional inverter is able to power both the full home and backup loads. Also, the battery can discharge to, or charge from, the electricity grid. Similarly, on a separate DC bus the battery can be charged from the rooftop solar instillation via the MPPT. A separate high voltage DC bus ports energy from the home battery to the vehicle battery through the high-power

DC/DC converter. The device controller and thermal management system are run via the low voltage pulled from the UPS which is connected to the main AC bus.

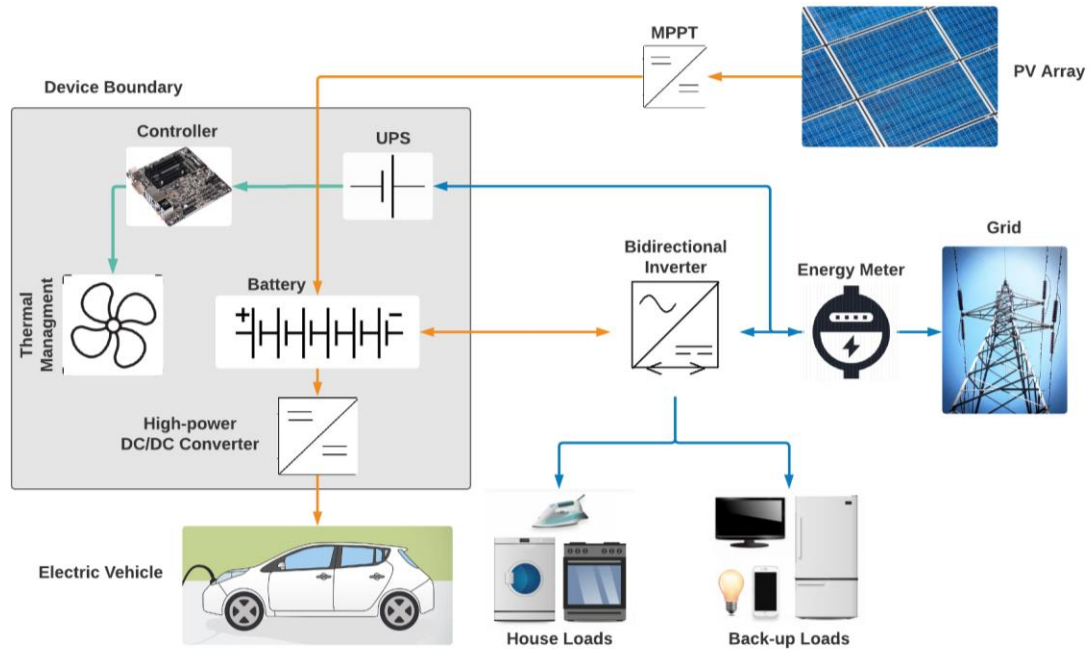


Figure 28 – Diagram of system electrical topology

3.2.3 Thermal Management Design

This thesis will explore the performance of different thermal management strategies for our device, the general design of these strategies will be discussed in this section. Possible strategies include passive thermal management, active liquid cooling, or active air cooling.

3.2.3.1 Passive Thermal Management Designs

The simplest thermal management strategy for the device is to adopt passive thermal management, where the only mechanism for heat rejection is natural convection. No fans or liquid cooling circuits are required for this strategy which reduces assembly and operating cost while sacrificing cooling performance.

The liquid cooled packs of the Ford Focus Electric and the Chevy Volt have modules with cooling fins structurally integrated and are not designed to accommodate air flow. To redesign the modules to allow more air flow to the cells would require module disassembly and reconstruction which would be costly in manufacturing. Thus, we will assume that if passive thermal management is used for the Volt and Focus batteries than the modules will be kept as is. The Leaf modules have air openings and channels into and through the module, which make them better suited for passive thermal management, however the small size of the module and the lack of air flow to the largest face of the cells impedes the rate of natural convection. Still, we assume the Leaf modules will be left intact for lower cost manufacturing.

Although the battery packs in vehicle are likely sealed, we assume that this will no longer be required as the device is stationary and indoors, thus waterproofing is less of a concern. We also assume that air exchange between the internal pack air and external air will be sufficiently high such that internal pack air temperature is equal to ambient temperature. This could be achieved with a small fan or large enough air openings.

3.2.3.2 Active Liquid Cooling Designs

For battery packs that employ liquid cooling channels, such as the Ford Focus Electric and the Chevy Volt, another option is to recreate the active liquid cooling circuit that is found in these vehicles (refer to section 2.4). These cooling circuits would be comprised of the following major components:

- **Coolant pump:** to circulate the coolant
- **Liquid to air heat exchanger:** to remove heat from the system
- **Liquid chiller:** either a secondary refrigerant loop or thermo-electric cell which provides additional heat rejection to the coolant
- **Coolant hoses:** to route in-between components
- **Diverter valve:** to switch flow between components
- **Expansion tank:** to allow for expansion of the coolant with temperature

A diagram of this configuration is shown in Figure 29. Coolant coming from the battery can be cooled either through the liquid to air heat exchanger and chiller or just the chiller if cooling below ambient temperature, with a diverter valve that controls flow between these two components. If heating is required for the battery, then a coolant heater is activated. The heater is placed close to the battery pack to minimize heat loss through the pipes. Another diverter valve is used here to bypass the cooling components when the heater is in use to prevent unnecessary heat loss. The expansion tank, serves the purpose of leaving room for the liquid to expand while also acting as the point where the coolant is first poured into the system. The coolant chosen for our design is a 50/50 water-glycol mixture, the same coolant used by the Chevy Volt [52].

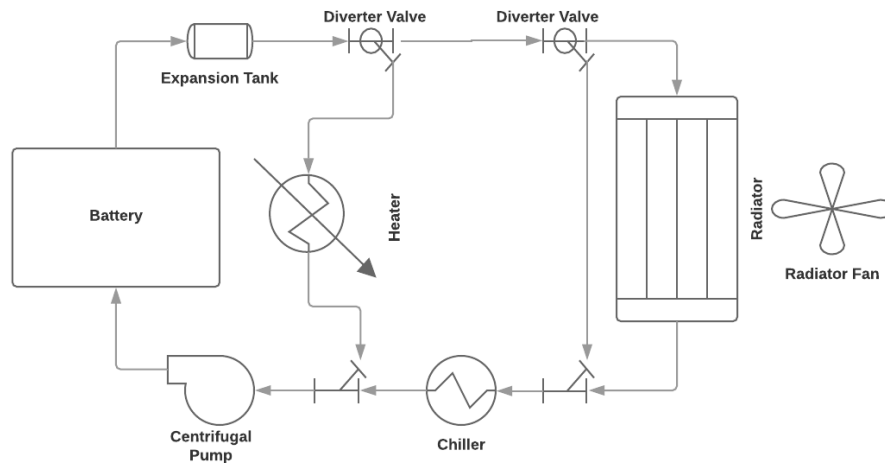


Figure 29 – Active liquid cooling concept circuit diagram

An alternative active liquid cooling thermal management design is to leave out the chiller and rely solely on the liquid to air heat exchanger to chill the liquid. Such a design would cut down significantly on cost but have less cooling capacity and would not be able to reduce the battery temperature below ambient temperature. Figure 30 shows the cooling circuit diagram for this configuration. Note that the diverter valve to bypass the radiator is unnecessary in this design.

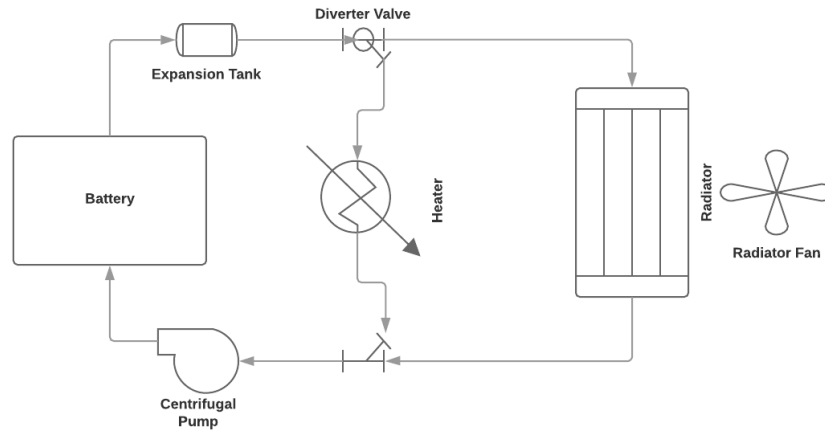


Figure 30 – Simplified active liquid cooling circuit with chiller removed

For both liquid cooling configurations, the cooling capacity of the liquid to air heat exchanger and chiller can be varied to match cost with cooling performance. For our study data on various liquid to air heat exchangers was taken from ATS Advanced Thermal Solution Inc, which publishes data on a variety of their fin-tube heat exchangers of various sizes [60]. Figure 31 shows an example of a fin and tube heat exchanger with and without fans. Figure 32 shows the pressure drop and heat exchange rate for a variety of heat exchanger sizes from ATS Inc.



Figure 31 – Example of heat exchanger from ATS Inc [60]

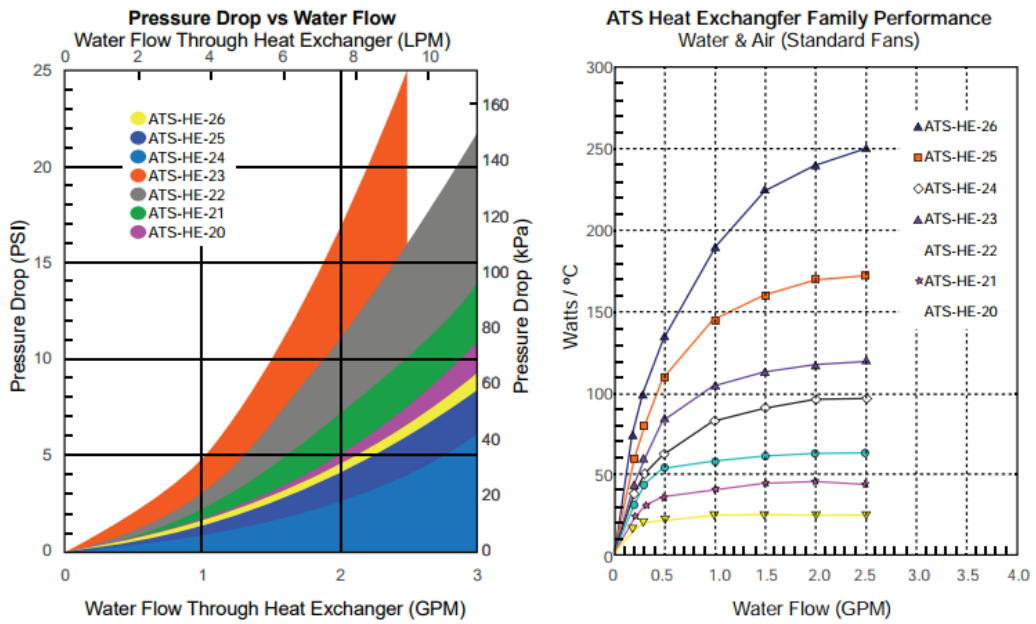


Figure 32 – Pressure drop and heat transfer coefficient for various sized heat exchangers from ATS Inc [60]

Similarly, data on chiller cooling capacity and power consumption was collected from Liard Technologies for their line of vapor-compression chillers (Figure 33).



Figure 33 – Example of coolant chiller from Laird Technologies [61].

In production it is unlikely that these exact heat exchangers and chillers will be used, however they serve as a good example for plausible amounts of cooling capacity and the trade-off with power consumption and cost.

3.2.3.3 Active Air Cooling Design

Another technique for thermal management is to implement forced air cooling with a fan, referred to as active air cooling. The only one of the three battery packs we study that is designed for air cooling is the Nissan Leaf battery, however it was not designed for active air cooling. Thus, we assume some changes are made to the pack construction to make forced air cooling more effective. First, we assume that air gaps are placed in-between the cells such that air can travel past the larger front faces of the cell rather than just the edges of the cell as in the current design as shown in Figure 34. This is consistent with other electric vehicles which are active air cooled [51, 62]. To make such a modification to the Nissan Leaf battery would likely be too costly to be feasible, but from

an analysis perspective, the results of this study can be useful for comparison with liquid cooling and for extrapolating to other battery packs which use air cooling.

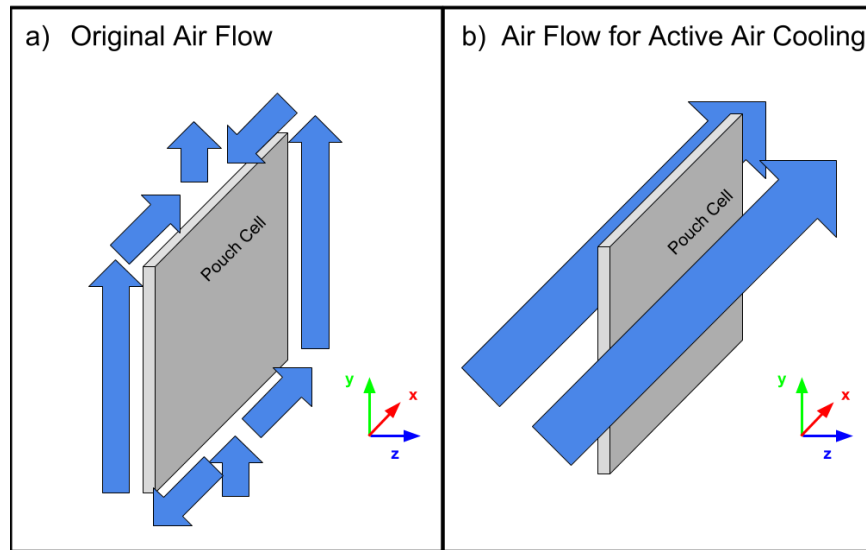


Figure 34 – Original air flow design around Nissan Leaf cell (a) vs the air flow assumed for active air cooling in our device (b)

We also assume that ambient air is passed through the pack, rather than circulating the same air inside the pack as in the original design. This is consistent with the same assumption made in section 3.2.3.1. Additionally, we assume the air is brought to the cells in parallel such that each cell receives uniform cooling to reduce the cell to cell temperature variation. This system will require a large fan to drive sufficient air flow and air filters to prevent contaminants from entering the battery pack. A basic diagram of air flow in the device under this configuration is shown in Figure 35.

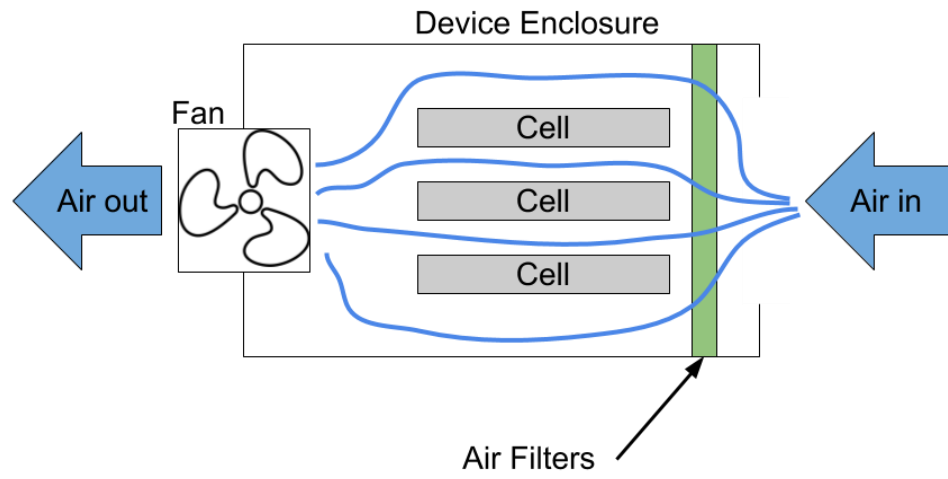


Figure 35 – Diagram of air flow for active air thermal management design

3.3 Battery Thermal Model

Now that the general design of the device electrical and thermal management systems is set, we look to analyze the performance of the different thermal management strategies. To do this we start by reducing the modeling domain to a single cell as we will discuss in Section 3.3.1. Because the cells are assumed uniform and cooling is provided in parallel we model a single cell and extrapolate the results to the entire pack. Next, in Section 3.3.2, we develop a model of cell heat generation based on the theoretical background and data from literature. In Sections 3.3.3 to 3.3.6, several different thermal modeling strategies are adopted to estimate the cell temperature depending on the thermal management strategy chosen. We start with a lumped capacitance model for analyzing battery temperature under adiabatic and weak convection (passive thermal management) conditions. For active liquid and air cooling we adopt a finite difference method to estimate cell internal temperature variation. Each of these methods is used to estimate the thermal performance of our device for a variety of charging and discharging rates.

3.3.1 Generalized Thermal Model Set-up

In the process of constructing the thermal models, we start by reducing the modelling domain to a single cell. We assume that each cell in the battery pack is identical in terms of heat generation, mass, and thermal properties and that each cell receives parallel cooling. If this is the case, we can assume each cell is equal temperature and extrapolate the results of modelling one cell to all the cells in the pack. Different cells may have aged differently inside a battery pack during vehicle life, and this would lead to different thermal

behaviour between cells. However, electric vehicle manufacturers implement mechanisms to help maintain uniform aging across the cells, like parallel thermal management and battery balancing, so it is likely that cells in a pack may be near uniform. Additionally, each cell is unlikely to receive exactly the same fluid flow rate but literature suggest that the pressure loss across the fins is sufficiently high to assume that each channel receives effectively the same cooling [52].

Next, we define the geometry of our cell model. We start by simplifying the cell geometry to a rectangular prism with thin fins on each side of the cell to represent the cell tabs. We define the largest dimension as the length, the second largest dimension as the width, and smallest dimension as the depth. Then we define the spatial axes with y along the length direction, x along the width, and z through the depth. The assumed orientation is that the cell is pointing up, with the length side vertical and gravity in the negative y direction. Figure 36, shows the geometric set up of our cell model.

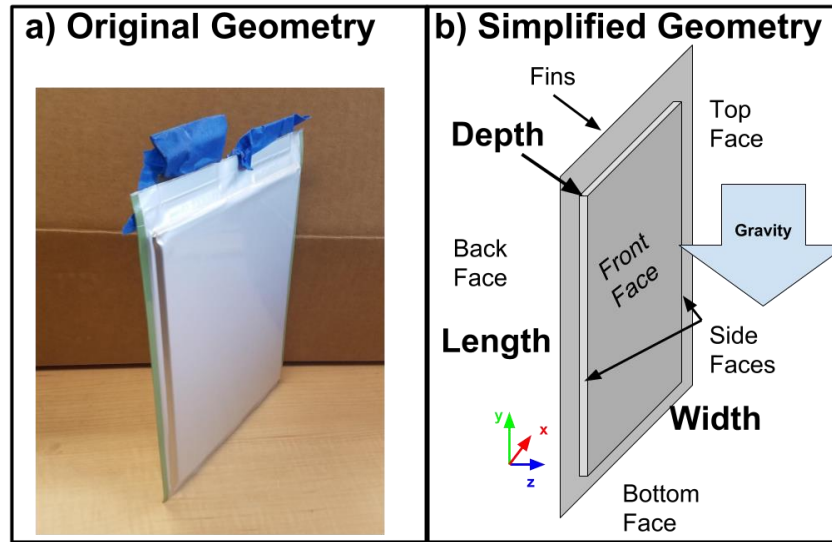


Figure 36 – Original geometry of the cells (a) (example shown is Volt cell); Defined geometry of the cell for thermal model with orientation and axis defined (b).

With geometry defined we next determine the heat flows and spatial domain for our model. Figure 39 shows the heat flows assumed for the cells under passive cooling. Since the front and back faces of the cells are adjacent to other cells, which we assume are the same temperature, we assume there is no heat transfer from these surfaces between cells. Thus, the only heat flows out of the battery are through passive convection from the cell side surfaces and fins.

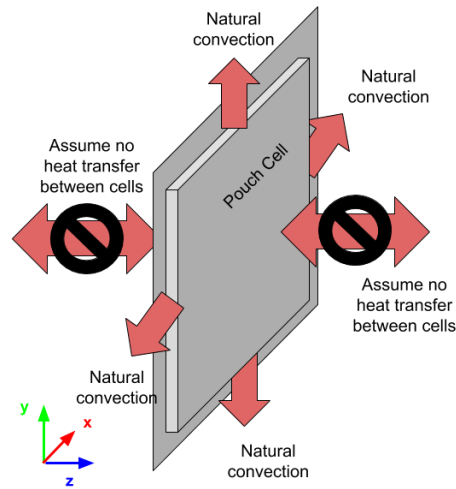


Figure 37 – Heat flows in thermal model for passively cooled cells

Figure 38 shows the heat flows and modelling domain for the Focus and Volt cells under liquid cooling. The cells transfer heat to the liquid cooling fin from the front face (z direction). The back face of the cell touches an adjacent cell, thus again we assume no heat is transferred between the cells. There will be natural convection from the side surfaces like in the passive cooled case, but we assume the liquid cooling will dominate and thus we neglect natural convection for simplicity. Because the pack configurations for the liquid cooled cells is assumed a repeated pattern of 2 cells and 1 cooling fin we can assume symmetry about a plane going through the centre of a cooling fin and a plane on the back face of the cell. Thus, the modelling domain includes one full cell and one half of a cooling fin.

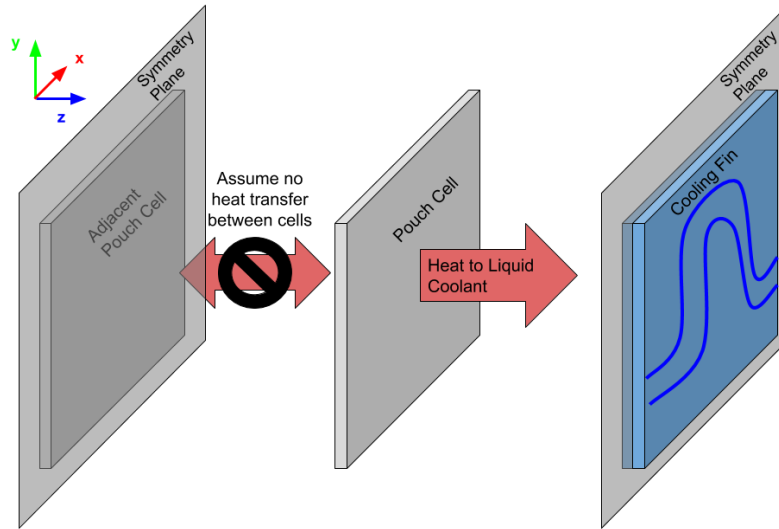


Figure 38 – Heat flows and model domain for liquid cooled cells

Figure 39 shows the heat flows and model domain for the active air-cooled Nissan Leaf cells. The cells transfer heat from both the front and back faces to the air cooling channels on either side of the cell. We assume that each side of the cell receives identical cooling and thus the temperature distribution in the cell is symmetric about a plane through its center. Thus, applying symmetry, the model domain for an air-cooled cell includes half of a cell and half of an air cooling channel.

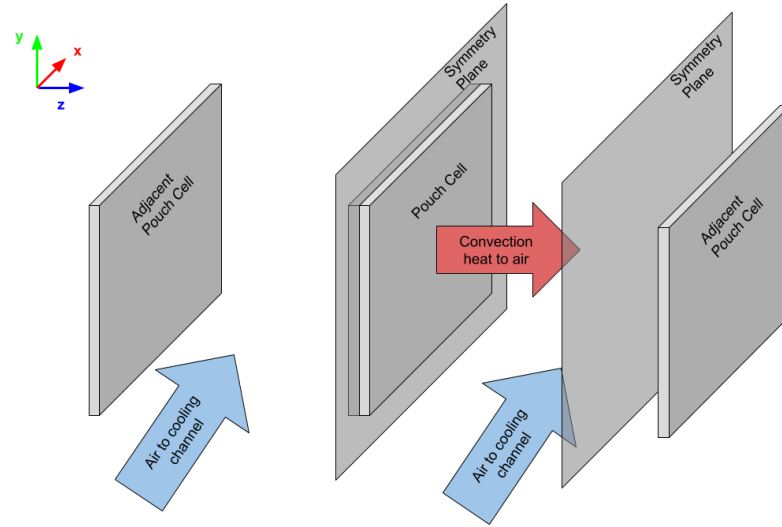


Figure 39 – Heat flows and model domain for air cooled cells

3.3.2 Battery Heat Generation Model

To accurately predict the temperature developed inside the battery cell we require an accurate model of battery heat generation. We start by assuming uniform heat generation within the cell. In real cells, heat is not generated uniformly but to accurately estimate internal differences in heat generation would require knowledge of the cell composition which is unknown for the batteries in study. Thus, we propose that assuming uniform heat generation is adequate for the system level analysis of this study.

To estimate heat generation, we adopt Equation 5, which is identical to Equation 4 from the background section. Where \dot{Q} is heat generation in watts, r is internal resistance in ohms, I is current in amps (positive if discharging), T is temperature in kelvin, and $\frac{dU}{dT}$ is the entropic heat coefficient in volts per kelvin [30].

$$\dot{Q} = I^2r - IT \frac{dU_{ocv}}{dT} \quad 5$$

The first term describes the irreversible heat due to joule heating and the second term describes the heat generated (or consumed) by the chemical reactions. This equation neglects heating from mixing and phase changes.

The entropic heat coefficient was taken from Liu et al. (2014), who measured this value at different SOC's for an aged 8.7 Ah lithium-manganese-oxide (LMO) cell [30]. Because the three electric vehicle packs in study are also LMO batteries, it is assumed that they have the same entropic heat coefficients. Figure 40 shows the entropic heat coefficient as a function of SOC as calculated by Liu et al. One modification we made to the data was to approximate the entropic heat coefficient with a 3rd order polynomial fit to improve computational speed.

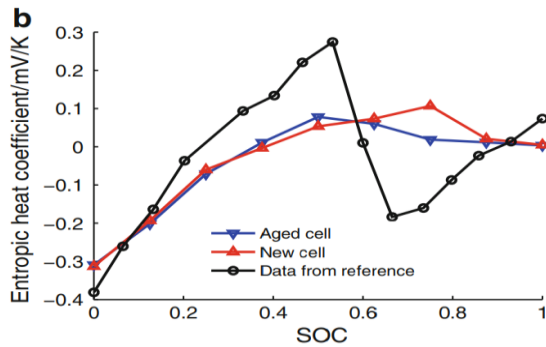


Figure 40 – Entropic heat coefficient for LMO cell [30]

The internal resistance of lithium-ion batteries also changes as a function of temperature and SOC. To calculate the resistance's dependence on temperature Equation 6 was used from [33], where r is the resistance at current temperature, r_{ref} is the reference resistance in ohms, E_a is an experimentally derived constant (found to be 28640 J/mol), R_{ug} is the universal gas constant (8.314 J/(K*mol)), T_{ref} is the reference temperature in K, and T is the temperature in K.

$$r = r_{ref} * \left[\exp \left(-\frac{E_a}{R_{ug}} * \left(\frac{1}{T} - \frac{1}{T_{ref}} \right) \right) \right] \quad 6$$

The parameter E_a was determined experimentally for a Nickel-Manganese-Cobalt (NMC) battery however this parameter was found to match well with the resistance temperature dependence found by Liu et al. (2014) for LMO batteries. Thus, this parameter was kept for modeling the LMO batteries of the three battery packs in study.

Figure 41 shows the change in resistance relative to the resistance at 25°C versus temperature of the battery. The resistance increases with decreased temperature exponentially, with a drop to -30 degrees from 25 degrees leading to near 4.5 times greater internal resistance. In the opposite direction, increasing the temperature to 40 degrees C nearly halves the resistance of the battery. Note from equation 5 that joule heating scales linearly with internal resistance, this means that joule heating increases at lower temperatures versus higher temperatures for the same current. This negative temperature coefficient phenomenon can be somewhat beneficial in the sense that when a battery is cold, more heat generation is desirable to heat it to a safer temperature, and when the battery is hot less, heat generation is desirable to cool the battery back down.

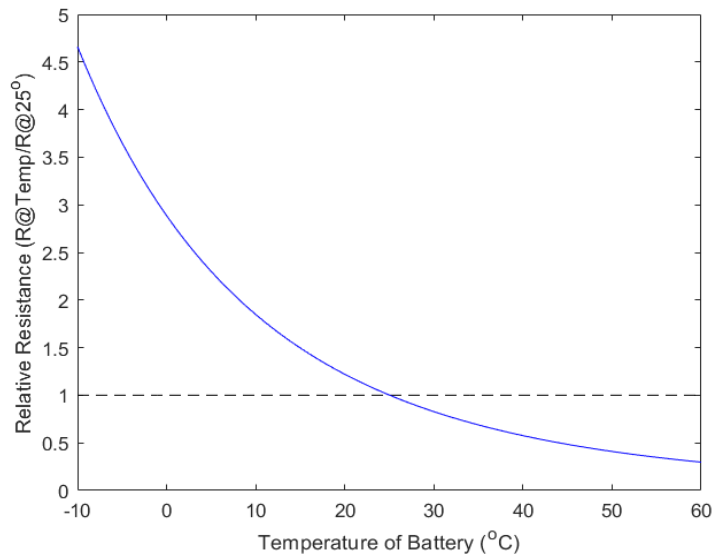


Figure 41 – Change in relative internal resistance with temperature

Internal resistance also varies with SOC; specifically for LMO cells, it increases greatly with low SOC [30]. However, we assume we will operate the batteries outside of these low SOC ranges [27], and battery testing from Idaho National Labs on the EV packs in this study show almost no variation in internal resistance within the expected SOC range [51]. Thus, for our analysis we assume that resistance does not depend on SOC.

To validate our model, we attempted to replicate the heat generation observed by Liu et al. (2014) for an 8 Ah LMO cell for various charging and discharging rates [30]. Figure 42 compares these results. The heat generation predicted by our model matches that found by Liu et al. thus we assume the model is valid.

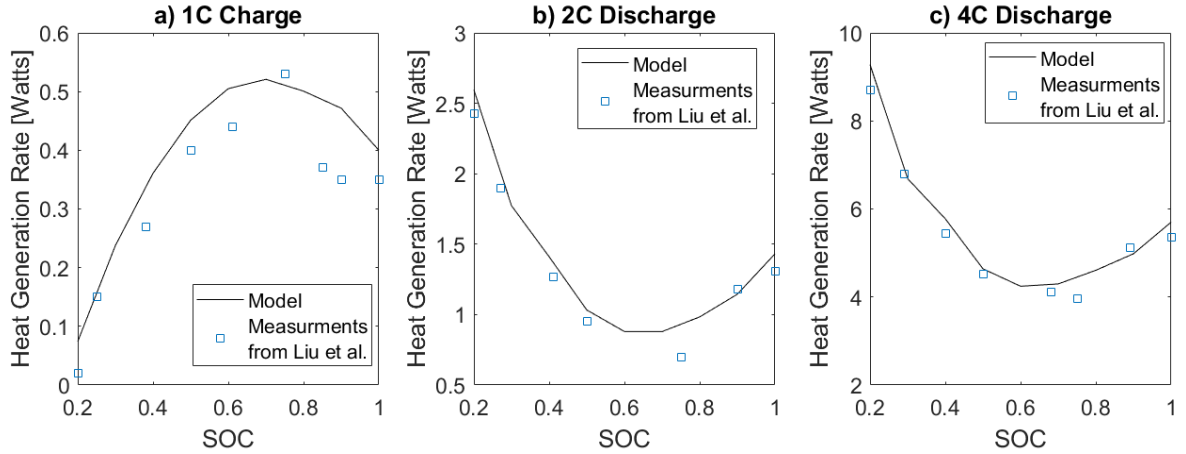


Figure 42 – Validation of heat generation model by comparison with Liu et al. (2014) [30]

3.3.3 Modelling for Adiabatic Conditions

With heat generation modelled, we start by calculating expected battery temperature under discharge and charge with adiabatic conditions, meaning no heat loss to the environment. Although such a usage case is not realistic, it can be useful for gauging the worst expected case of battery temperature under different discharge and charge rates.

We can estimate the temperature of the battery by applying an energy balance to the system as shown in Equation 7, where m is the mass of the battery cell in kg, C_p is the battery heat capacity in J/KgK, T_{batt} is the battery temperature in kelvin, and \dot{Q}_{gen} is the heat generated by the battery in watts. The left side of the equation is the rate of thermal energy stored inside the battery and the right side is the heat generated by the battery through ohmic losses and reaction heat. Because there is no heat transfer to the

environment, all heat generated in the battery is translated directly to heat stored in its thermal mass.

$$mC_p \frac{dT_{batt}}{dt} = \dot{Q}_{gen} \quad 7$$

An inherent assumption in this equation is that the temperature in the cell is uniform. This is typically considered a valid assumption when the Biot number is less than 0.1 [63]. Equation 8 shows the calculation of the Biot number, Bi , where V is the volume of the body in m^3 , h is the heat transfer coefficient on the surface of the body in W/m^2K , A is the surface areas of heat transfer out of the body in m^2 , and k is the thermal conductivity of the body in W/mK .

$$Bi = \frac{Vh}{Ak} \quad 8$$

Note that for adiabatic analysis the heat transfer coefficient h is assumed to be zero, thus the Biot number is also zero and the isothermal assumption is valid. Though the Biot number calculation is not critical for adiabatic analysis, it will be more important in later analysis where h is non-zero.

3.3.4 Modelling for Passive Thermal Management

Under a passive thermal management scenario, there is no forced flow of liquid or air and the only method of heat transfer is through natural convection. As described in

section 3.3.1, it is assumed that convection only occurs from the sides but not the largest faces of the cell.

To calculate heat transfer due to natural convection we use Equation 9, where \dot{Q} is the heat transfer rate in watts, h is the convection coefficient in $\text{W}/\text{m}^2\text{K}$, A is the area in m^2 , T_{surf} is the surface temperature in kelvin, and T_{air} is the air temperature in kelvin [63].

$$\dot{Q} = hA(T_{surf} - T_{air}) \quad 9$$

3.3.4.1 Natural Convection Coefficient Estimates

To get an estimate for the heat transfer coefficient h we use Equation 10, where Nu is the dimensionless Nusselt number, k is the thermal conductivity of air in w/mK , and L is the characteristic length in meters.

$$h = \frac{Nu * k}{L} \quad 10$$

Experimentally derived correlations exist for the Nusselt number in different scenarios. For the vertical faces of the cell, Equation 11 was used to calculate the Nusselt number. It is an experimentally derived correlation for natural convection from an isothermal vertical plate, where Ra and Pr are the dimensionless Rayleigh and Prandtl numbers respectively [64]. The characteristic length for this equation is the length of the cell.

$$Nu = \left[0.825 + \frac{0.387 * Ra^{\frac{1}{6}}}{\left[1 + (0.492/Pr)^{\frac{9}{16}} \right]^{\frac{4}{9}}} \right]^2 \quad 11$$

For the horizontal faces, Equation 12 was used and is an experimentally derived correlation for natural convection from a horizontal isothermal plate [64]. The characteristic length for this equation is the surface area of the face over the perimeter.

$$Nu = 0.54Ra^{0.25} \quad 12$$

Using Equations 10-12 and the cell dimensions specified in section 2.4.4, natural convection coefficients were calculated for a range of air temperatures and surface temperatures. We used air temperatures of -23°C, 27°C, and -77°C to represent extreme low, medium, and extreme high temperatures. The properties of dry air at these temperatures was taken from reference [65]. For each of the air temperatures selected, the cell temperature was set to either 5°C or 50°C higher than the air temperature to represent a small temperature and large temperature difference respectively.

Table 3 shows the resulting convection coefficients for each EV cell under each scenario. Note that the values for the Volt and Focus are equivalent because they are assumed the same size. The values range from 2.8 to 7.5 W/m² with values increasing with increased delta temperature and decreased air temperature. These results are used to

estimates the convection coefficient including uncertainty as will be described in Section 3.7.7.

Table 3 – Natural convection coefficients for a variety of air and cell temperatures

	Cell temperature above ambient	Focus and Volt			Leaf		
		-23°C Air	27°C Air	77°C Air	-23°C Air	27°C Air	77°C Air
Horizontal Surfaces	5°C	3.5	3.0	2.8	3.5	3.0	2.8
	50°C	6.3	5.5	5.1	6.3	5.5	5.1
Vertical Surfaces	5°C	3.3	3.2	3.1	2.9	2.8	2.7
	50°C	5.1	4.9	4.8	4.5	4.3	4.2

3.3.4.2 Modeling Convection from Fins

To model convection from the fin we assumed the fin thickness (around 0.3 mm) was much smaller than its length (around 10 mm). Thus we can use Equation 13 to calculate the heat transfer from the fin, where h is the natural convection coefficient in W/m^2K , P is the fin perimeter in meters, k is the fin thermal conductivity in W/m , A_c is the cross sectional area of the fin in m^2 , and L is the length of the fin in meters [63].

$$\dot{q}_{fin} = \sqrt{hPkA_c} * (T_{cell} - T_{amb}) * \tanh(mL)$$

13

$$m = \sqrt{\frac{hP}{kA_c}}$$

Equation 13 can be used to form Equation 14 for the efficiency of the fin, defined as the ratio of heat transferred relative to the heat transferred if the fin were uniform temperature.

$$\eta_{\text{fin}} = \frac{\tanh(mL)}{mL} \quad 14$$

3.3.4.3 Isothermal Assumption and Governing Equation

Next, we determined if the cells can be assumed isothermal by calculating the Biot number for the cells under natural convection. To do so we need values for the thermal conductivity of the pouch cells. Lithium-ion cells are reported to have anisotropic thermal conductivities, with the conductivity through the electrode layers (z direction) being much smaller than the conductivity parallel to the layers (x and y directions). The exact thermal conductivities of the electric vehicles cells in this study are unknown so to make an inference we collected values from literature where the in-plane thermal conductivities range from 18 to 45 W/mK and the through-plane conductivities range from 0.34 to 1 W/mK. This will be discussed further in Section 3.8.2.

The Biot number was then calculated for each of the electric vehicle cells using a convection coefficient of 10 W/m²K, which is higher than any natural convection coefficient we expect, and an in-plane thermal conductivity of 18.4 W/mK, which is the lowest across all the studies observed. We only use the in-plane thermal conductivity because we assume no heat transfer in the through-plane (z) direction. The resulting Biot number is 0.008 for the Focus and Volt cells and 0.014 for the Leaf cell, which is sufficiently small to assume isothermal conditions.

Since the isothermal assumption is proved valid, we adopt a lumped capacitance model to predict the cell temperature over time. Applying an energy balance to the system produces the differential equation shown in Equation 15, where the left side is the change in thermal energy stored in the battery and the right side is the heat generated minus the heat lost via convection.

$$mC_p \frac{dT_{batt}}{dt} = \dot{Q}_{gen} - hA(T_{batt} - T_{air}) \quad 15$$

3.3.5 *Modelling Active Liquid Cooling*

In this section we develop the methods used to model the active liquid cooled battery packs.

3.3.5.1 Derivation of Governing Equations

To model active liquid cooling of the cells, the isothermal assumption cannot be made because the fluid heats up during its path through the cooling fin and creates a temperature distribution across the cell surface [62]. Additionally, the convection values are much higher and thus the Biot number is likely to be very large, which would mean a large temperature distribution through the thickness of the cell. Thus for this analysis we adopt the heat equation as shown in Equation 16, where T is temperature in kelvin, α is the thermal diffusivity in m^2/s , \dot{q}_v is the volumetric heat generation in W/m^3 , ρ is density in kg/m^3 , and C_p is heat capacity in J/kgK , and x, y, z are the spatial dimensions in meters.[66].

$$\frac{dT}{dt} = \alpha * \left(\frac{d^2T}{dx^2} + \frac{d^2T}{dy^2} + \frac{d^2T}{dz^2} \right) + \frac{\dot{q}_v}{\rho C_p} \quad 16$$

Because the geometry of our cell and fin system is rather complicated, we approximate the spatial derivatives with the central difference method by discretising the domain into multiple isothermal, uniform property nodes. This transforms the partial differential equation, Equation 16, into an ordinary differential equation, Equation 17, for the temperature at cell node (i,j,k) where i is the x coordinate, j is the y coordinate, and k is the z coordinate.

$$\begin{aligned} \frac{dT_{i,j,k}}{dt} = \alpha * & \left(\frac{T_{i+1,j,k} - 2T_{i,j,k} + T_{i-1,j,k}}{\Delta x^2} + \frac{T_{i,j+1,k} - 2T_{i,j,k} + T_{i,j-1,k}}{\Delta y^2} \right. \\ & \left. + \frac{T_{i,j,k+1} - 2T_{i,j,k} + T_{i,j,k-1}}{\Delta z^2} \right) + \frac{\dot{q}_v}{\rho C_p} \end{aligned} \quad 17$$

Equation 17 only models internal conduction within the cell. To model the interaction with the fluid, an additional layer of fluid nodes is added on top of the cell nodes. Equation 18 describes the dynamics of the fluid nodes and is formed by applying an energy balance to a discrete volume of fluid, where h is the heat transfer coefficient in W/m²K, A is the heat transfer area between the cell and the fluid channel in meters, $m_{f,i}$ is the mass of a single fluid element in kg, $C_{p,f}$ is the heat capacity of the fluid in J/kgK, \dot{m} is the mass flow rate through the channel in kg/s, and $T_{f,i-1}$ is the temperature of the previous fluid element in the channel.

$$\frac{dT_{f,i}}{dt} = \frac{hA}{m_{f,i}C_{p,f}}(T_{i,j,k} - T_{f,i}) + \frac{\dot{m}}{m_{f,i}}(T_{f,i-1}) - \frac{\dot{m}}{m_{f,i}}(T_{f,i}) \quad 18$$

3.3.5.2 Creating a Multi-Nodal Model

Equations 17 and 18 can be combined to create a system of ordinary differential equations by breaking up the cell and fluid into any number of nodes. To illustrate how this is done we will go over an example where the cell is broken into 8 nodes with two layers in the Z dimension. Later analysis will use a higher number of nodes, however the methodology remains the same.

The first step is to simplify the geometry of the cell and fin by collapsing the multiple cooling channels into a single channel of equal heat transfer area. Figure 43, shows the cooling fin geometry of the Chevy Volt on the left and the simplified, analogous geometry on the right.

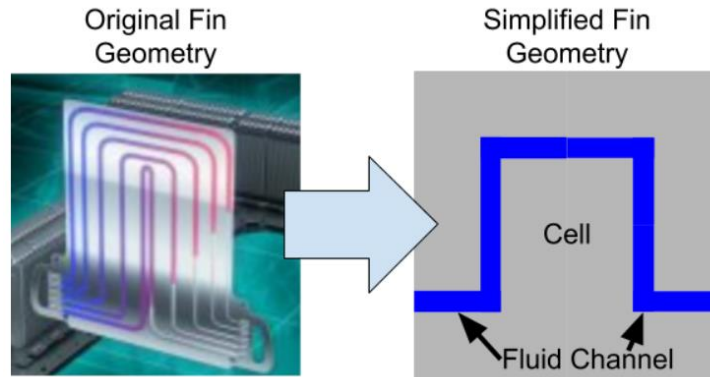


Figure 43 – Example of simplified fin and cell geometry for liquid cooled model

The next step is to break up the cell and fluid channel into nodes. The node numbers for this example are shown in Figure 44, where “F” denotes fluid nodes and “C” denotes cell nodes. The cell is broken into 4 “zones” in the x-y plane where each zone has one fluid, one cell surface, and one internal cell node. For simplicity we will assume that the cell nodes are square, that is $\Delta x = \Delta y$, and that the length of each fluid element is the same.

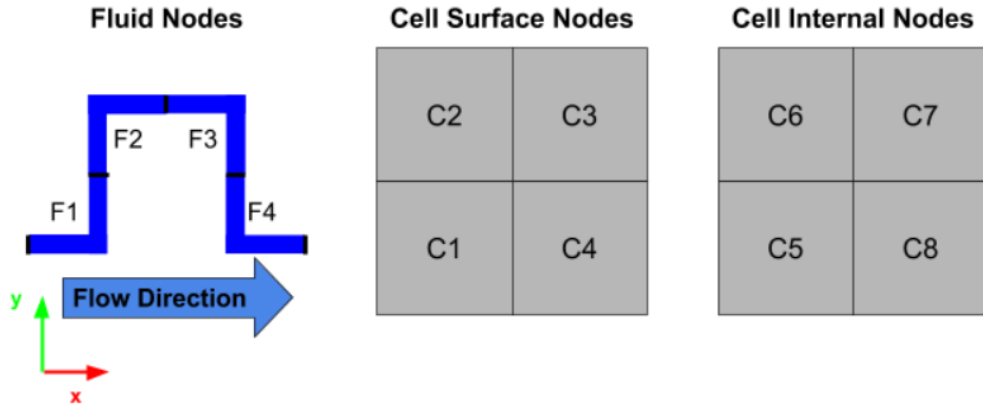


Figure 44 – Example of thermal node numbering

Once the nodes are created, we can generate the equations that represent the interactions between the nodes. We will do so in state space notation as shown in Equation 19, where the state vector \bar{X} includes the temperatures of the nodes and the inputs are the fluid inlet temperature (T_{fi}) and the volumetric heat generation (\dot{q}_{gen}).

$$\dot{\bar{X}} = A\bar{X} + B_q * \dot{q}_{gen} + B_{T_{fi}} * T_{fi} \quad 19$$

The state vector \bar{X} is structured with the cell surface nodes first, then the internal cell nodes and then the fluid nodes as shown in Equation 20.

$$\bar{X} = \begin{bmatrix} \bar{X}_{surface} \\ \bar{X}_{internal} \\ \bar{X}_{fluid} \end{bmatrix} = \begin{bmatrix} T_{C1} \\ T_{C2} \\ T_{C3} \\ T_{C4} \\ \overline{T_{C5}} \\ T_{C6} \\ T_{C7} \\ T_{C8} \\ \overline{T_{f1}} \\ T_{f2} \\ T_{f3} \\ T_{f4} \end{bmatrix} \quad \mathbf{20}$$

Matrix A , shown in Equation 21 defines the interactions between the nodes. For clarity we defined A in terms of the following submatrices: A_{xy} which defines conduction in the x-y direction, A_z which defines conduction in the z direction, A_{fc} and A_{cf} which define convection from the fluid to the cell and visa-versa, and A_f which defines mass transfer among the fluid elements. Each of these submatrices is of size 4×4 .

$$A = \begin{bmatrix} A_{xy} - A_z - A_{fc} & A_z & A_{fc} \\ A_z & A_{xy} - A_z & O_{4,4} \\ A_{cf} & O_{4,4} & A_f - A_{cf} \end{bmatrix} \quad \mathbf{21}$$

Matrix A_{xy} is a tridiagonal matrix composed of the thermal diffusivity in the x-y direction, α_{xy} . Note that the thermal diffusivity in the x-y direction is different than in the z direction due to the anisotropic thermal conductivity of the cell. For each row in A_{xy} there is a term for the interaction of that node with the nodes around it.

$$A_{xy} = \begin{bmatrix} -2\alpha_{xy} & \alpha_{xy} & 0 & 0 \\ \alpha_{xy} & -2\alpha_{xy} & \alpha_{xy} & 0 \\ 0 & \alpha_{xy} & -2\alpha_{xy} & \alpha_{xy} \\ 0 & 0 & \alpha_{xy} & -2\alpha_{xy} \end{bmatrix} \quad 22$$

Matrix A_{xy} is a diagonal matrix in terms of the thermal diffusivity in the z direction.

$$A_z = I_4 * \alpha_z \quad 23$$

Matrices A_{fc} and A_{cf} are diagonal matrices as shown in Equation 24, where h is the convection coefficient in W/m²K, A is the heat transfer area in meters, $m_{c,i}$ and $m_{f,i}$ are the mass of the cell and fluid elements in kg, and $C_{p,c}$ and $C_{p,f}$ are the heat capacity of the cell and fluid in J/kgK.

$$A_{fc} = I_N * \frac{hA}{m_{c,i}C_{p,c}}; \quad A_{cf} = I_N * \frac{hA}{m_{f,i}C_{p,f}} \quad 24$$

Matrix A_f is a tri diagonal matrix in terms of the mass of the fluid element, $m_{f,i}$, in kg, and the mass flow rate, \dot{m} , in kg/s.

$$A_f = \begin{bmatrix} 1 & 0 & 0 & 0 \\ -1 & 1 & 0 & 0 \\ 0 & -1 & 1 & 0 \\ 0 & 0 & -1 & 1 \end{bmatrix} * \frac{\dot{m}}{m_{f,i}} \quad 25$$

Next, we construct the B matrices. Matrix B_q applies the input internal heat generation to each of the cell nodes as shown in Equation 26.

$$B_q = [1,1,1,1,1,1,1,1,0,0,0,0]' / \rho C_{p,c} \quad 26$$

Matrix B_q applies the effects of the input fluid temperature to the first fluid node as shown in Equation 27

$$B_q = [0,0,0,0,0,0,0,0,1,0,0,0]' * \frac{\dot{m}}{m_{f,i}} \quad 27$$

For most situations we analyze, the input fluid temperature is not constant but rather a function of the output fluid temperature and the heat dissipated through the heat exchanger and liquid chiller as shown in Equation 28, where T_{fo} and T_{fi} are the fluid temperature out of and into the fin respectively, h_{HX} is the heat transfer capacity of the heat exchanger in W/K, and \dot{q}_{chill} is the heat pumped from the fluid via the liquid chiller in watts.


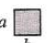
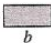
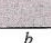
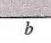
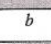




$$T_{fi} = T_{fo} - \frac{h_{HX}(T_{fo} - T_{amb}) + \dot{q}_{chill}}{\dot{m}C_{p,f}} \quad 28$$

Note that this equation does not account for lag created as the water flows to and from the heat exchanger, but rather assumes an instantaneous change in water temperature. This is a conservative assumption for cooling as the fluid in the non-battery components acts as a reservoir which absorbs some heat at the start of the charge or discharge. Additionally, we are assuming no heat loss in the pipes that connect the battery pack to the heat exchanger. This is also a conservative assumption.

3.3.5.3 Convection Coefficient Estimation

Later analysis which will be covered in Section 3.5 will show that the flow fluid flow in the cooling channels is laminar, thus by also assuming the cooling channel cross section is rectangular, we can pull the Nusselt number from Table 4. Because our situation is neither uniform heat flow nor uniform surface temperature, we use both correlations and use them to create an uncertainty distribution as will be described in Section 3.7.7.

Table 4 – Nusselt number correlations for laminar flow in rectangular ducts [64]

Cross Section	$\frac{b}{a}$	$Nu_D = \frac{hD_h}{k}$	
		(Uniform q_s'')	(Uniform T_s)
	—	4.36	3.66
	1.0	3.61	2.98
	1.43	3.73	3.08
	2.0	4.12	3.39
	3.0	4.79	3.96
	4.0	5.33	4.44
	8.0	6.49	5.60
	∞	8.23	7.54
	∞	5.39	4.86
	—	3.11	2.49

3.3.5.4 Validation

To validate our model, we attempted to replicate the results of Chen et al. (2016) who studied the temperature response of an electric vehicle cell with fin liquid cooling using a finite element model in Ansys Fluent [62]. The model Geometry setup is shown in Figure 45. The parameters used by Chen et al. in their model are shown in Table 5.

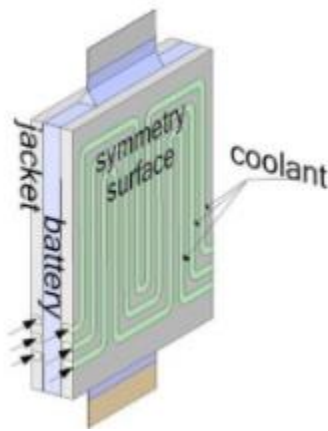


Figure 45 – Model geometry used by Chen et al. [62]

Table 5 – Parameters used by Chen et al. [62]

Parameter	Value
Cell dimensions	169mm x 197mm x 7mm
Fin and channel thickness	1 mm
Discharge rate	2.71 C
Average cell heat generation	15.7 W
Fluid type	50/50 Ethylene-Glycol

We create an analogous geometry with only one cooling channel, with the same heat transfer area and number of turns. Due to symmetry, we only model one-half cell and one-half cooling channel. We break the cell up into 3 layers in the z direction with each layer having 20 nodes and break the cooling fin into 20 fluid nodes. We use the same parameters shown in Table 5, plus we assume the thermal conductivity in the x-y and z directions to be 25 and 0.7 W/mK respectively. The cell heat capacity was judged to be 1300 J/kgK based on results reported by Chen et al.

This model was run with a variety of mass flow rates from 0 to 1 g/s to the cooling fin and cell temperature at the end of the discharge was compared with the results from Chen et al. Figure 46 compares the results from the finite difference model and Chen et al. at the end of the 2.71 C discharge and Figure 47 compares the surface temperature for both models at 0.29 g/s of coolant flow. There are slight differences in the results which are likely due to our assumption of uniform heat generation and differences in the heat transfer

coefficients and cell thermal conductivity used, however, the models agree well, and the finite difference model is assumed valid.

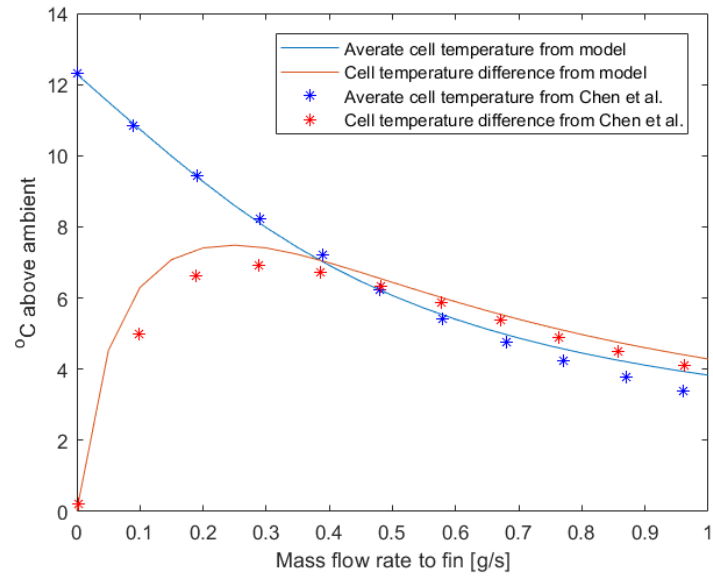


Figure 46 – Comparison of cell average temperature and temperature difference between our model and the model from Chen et al. for the end of a 2.71 C discharge.

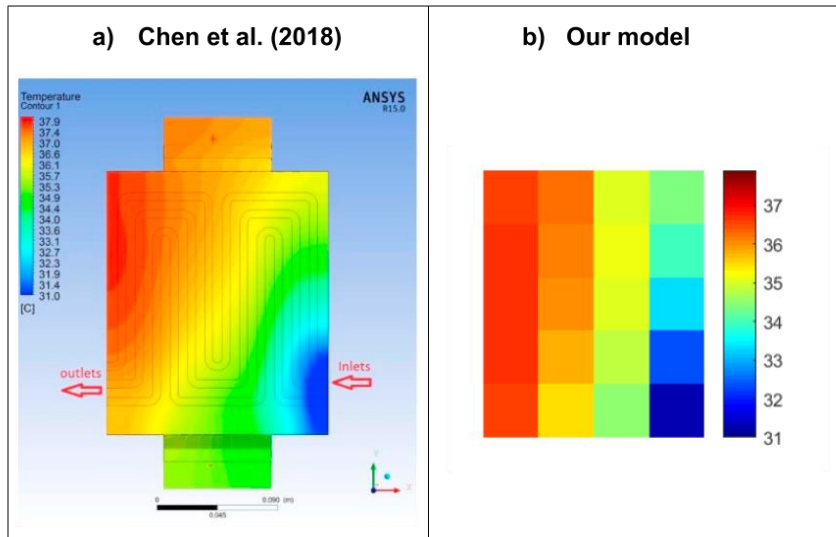


Figure 47 – Comparison of cell surface temperature from our model (b) and the model from Chen et al. (a) for the end of a 2.71 C discharge and 0.29 g/s of coolant flow

3.3.5.5 Convergence Study and Mesh Selection

To determine the appropriate number of nodes to use in our cell model we conducted a convergence study to observe the effect of node number on the resulting cell average temperature and temperature gradient. We created the following geometries each meant to approximate the actual cell and fin geometry at increasing levels of detail:

- Geometry 1: 6 nodes per cell layer and one cooling channel
- Geometry 2: 20 nodes per cell layer and two cooling channels
- Geometry 3: 42 nodes per cell layer and three cooling channels

We varied the number of cell layers in the z direction for each of these geometries and observed their effect on the cell average temperature above ambient and the cell

temperature gradient. Figure 48, shows these results for a Volt cell after a 3C discharge and 50 cm³/min of coolant flow. Increasing the number of layers in the z-direction from 1 to 2 has a great effect on the accuracy of the solution due to low thermal conductivity of the cell in this direction, while increasing beyond 2 layers sees diminishing increases in accuracy. Similarly, increasing the number of nodes per layer also increases the accuracy of the solution. Based on the convergence study we determine that using 5 layers of 20 nodes each for the cell model is a good balance between accuracy and computational efficiency.

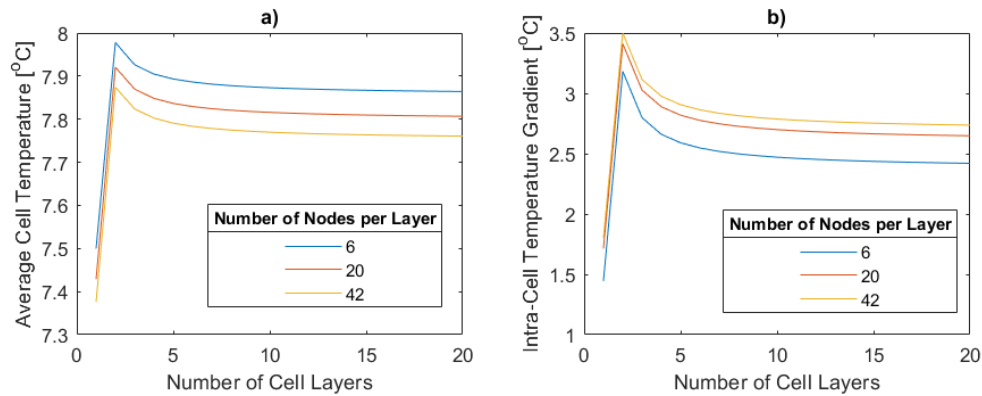


Figure 48 – Convergence study for average cell temperature and cell temperature gradient for liquid cooled Volt cell after 3C discharge.

3.3.6 Modelling Active Air Cooling

To model air cooling we adopted the same multi-nodal, finite-difference model used for liquid cooling, only we change the fluid channel and fluid parameters to match the air-cooled design. Figure 49 shows how the fluid channel and cell are broken up for this

model. The number of nodes in this figure is reduced for clarity compared to the actual model. Note that as air is provided in parallel along the length of the cell we assume no temperature variation in the y direction and thus there is only one layer of nodes in this direction.

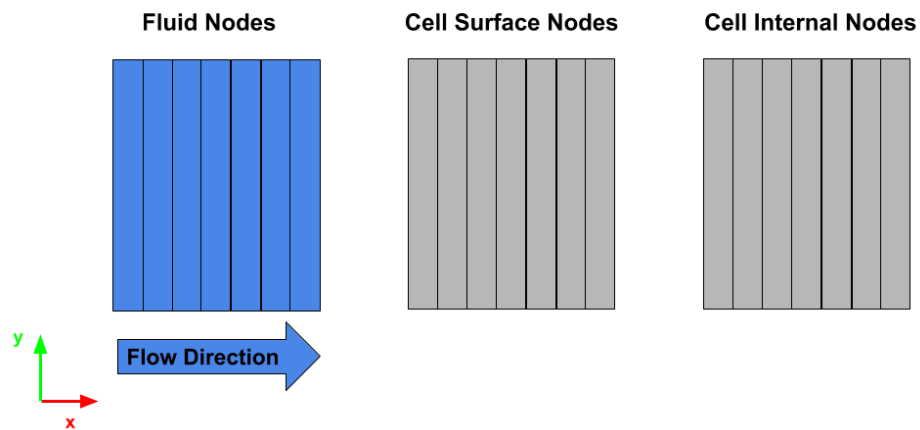


Figure 49 – Example of model geometry for active air cooled case

3.3.6.1 Convection Coefficient Estimation

Just as in the liquid cooling case we found that the air flow in the cooling gap was also laminar for the flow rates in study. Also, we assume the channel formed between two cells is a rectangular duct. Thus, we use the Nusselt number correlations from Table 4 shown previously.

3.3.6.2 Validation

To validate our model, we again compared our results with those of Chen et al. (2016) who simulated air cooling of a battery cell with a finite-element model. The parameters they used were the same as those for the liquid cooled battery from Table 5 except the cooling fluid was air. We apply the same parameters to our model with 3 cell layers and 20 nodes per layer. Figure 50 shows the results from our model and the model from Chen et al. for different air mass flow rates and Figure 51 compares the surface temperature for both models at 0.9 g/s of air flow. Again, differences between the models could be due to our assumption of uniform heat generation and differences in the heat transfer coefficients and cell thermal conductivity used, however the results are similar and the model is assumed valid

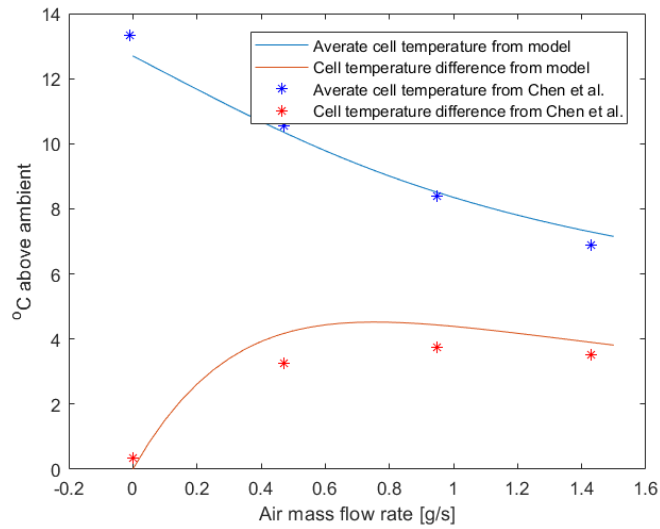


Figure 50 – Comparison of cell average temperature and temperature difference between our model and the model from Chen et al. for the end of a 2.71 C discharge.

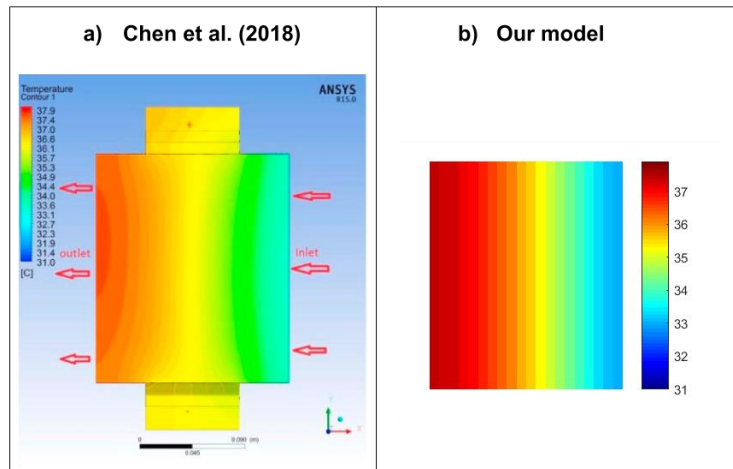


Figure 51 – Comparison of cell surface temperature from our model (b) and the model from Chen et al. (a) for the end of a 2.71 C discharge and 0.9 g/s of air flow.

3.3.6.3 Convergence Study and Mesh Selection

Like the liquid cooled case, we conduct a convergence study to determine the appropriate number of nodes to use in our model. Figure 52 shows the resulting average cell temperature and cell temperature gradient after breaking the Nissan Leaf cell into 1,3, and 5 layers, while varying the number of nodes per layer. From this study we determined that using 3 layers with 20 nodes each was a good balance between accuracy and computational efficiency.

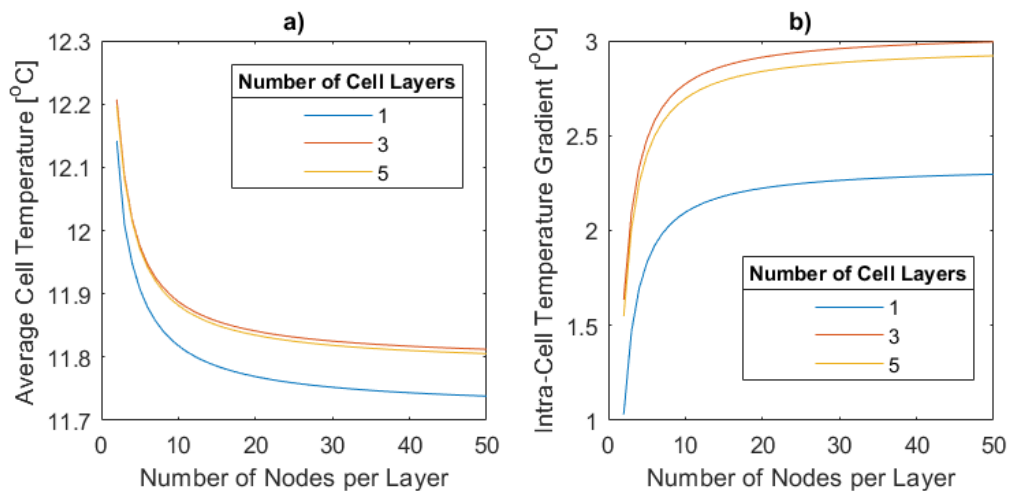


Figure 52 – Convergence study for average cell temperature and cell temperature gradient for air cooled Leaf cell after 3C discharge.

3.4 Electrical Model

To get an accurate estimation of the battery SOC, power output, and efficiency during operation, simple methods were adopted to model the electrical performance of the batteries. We start by modeling state of charge of the battery. Lithium-ion cells have a very high coulombic efficiency for most cases, though the coulombic efficiency can change with temperature and C-rate. We neglect these factors for our analysis and assume the coulombic efficiency is 100% [67]. With this assumption we can determine the SOC of the battery via the differential equation, Equation 29, where I is the current from the battery in amps, Q_{Ah} is the capacity of the battery in amp-hours, and t is time in hours [68].

$$\frac{dSOC}{dt} = I/Q_{Ah} \quad 29$$

Equation 29, works for when the current draw from the battery is known but it will be more useful to define current draw from the battery in terms of power delivered at load. To do this we assume that the voltage drop in the battery is solely due to internal resistance, then we can solve for the closed-circuit voltage of the battery with Equation 30, where U is the voltage of the battery in volts, U_{ocv} is the open circuit voltage of the battery in volts, and r is the internal resistance.

$$U = U_{ocv} - Ir \quad 30$$

The power applied to the load from the battery is calculated from Equation 31, which can be combined with Equation 30 to form Equation 32 which describes the relationship between power and current from the battery if U_{ocv} is known.

$$Power = U * I \quad 31$$

$$Power = IU_{ocv} - I^2r \quad 32$$

Next, we must model the battery open circuit voltage. Although the open-circuit voltage of batteries varies non-linearly, especially at low and high SOC, data from Idaho National Labs shows that the voltage for the EV batteries we have chosen varies nearly linearly within the 100%-20% SOC range we propose to use. Thus, we solve for the open-circuit voltage at any given SOC with Equation 33, where α is the slope of the voltage versus SOC curve, and SOC_{nom} and U_{nom} are the nominal voltage and SOC respectively.

$$U_{ocv} = \alpha * (SOC - SOC_{nom}) + U_{nom} \quad 33$$

Table 6 contains the parameters used in Equation 33 which were derived from data from Idaho National Labs [51].

Table 6 – Parameters for calculating open circuit voltage

	Ford Focus Electric	Chevy Volt	Nissan Leaf
α [V]	62.7	67.8	55.7
U_{nom}	358	394	398
SOC_{nom}	1	1	1

Applying Equations 31 and 33 is equivalent to modeling the battery pack with the equivalent circuit shown in Figure 53. Where the constant voltage source (U_{min}) is the minimum open circuit potential of the battery, the capacitor (C) models the linear change in open circuit potential with SOC, and the resistor ($R_{internal}$) models the voltage drop due to internal resistance.

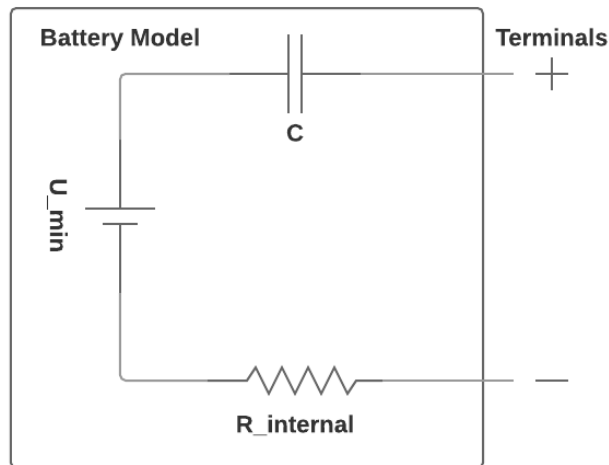


Figure 53 – Battery equivalent circuit model

3.5 Fluid Model

To understand power usage of the thermal management system, we wish to calculate the pressure drop that is produced across the cooling circuit. For liquid cooling, if we take the pressure drop across the cooling fins as the dominate pressure drop for the battery pack (as suggested by Parrish et al. [52]) then we can assume that the two are equal. For both liquid and air cooling, the fluid is supplied to the cooling channels in parallel, thus if we assume that each cooling fin receives the same amount of flow, then the pressure drop through one channel should be the pressure across the pack. This can be explained via a circuit analogy as shown in Figure 54 where each of the cooling fins or air channels is like a resistance in an electrical circuit. In the electrical system the potential is a voltage difference and we can see that the voltage drops across one resistor is the same as the drop across the whole circuit. In the fluid system the potential is pressure and we can see it follows the same behavior.

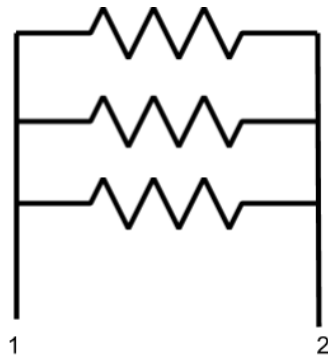


Figure 54 – Fluid-circuit analogy for pressure drop

To calculate the pressure drop across a cell we use Equation 34, where ΔP is the pressure drop in Pa, f is the friction factor, D_h is the hydraulic diameter of the channel in meters, $K_{L,i}$ is a minor loss coefficient, ρ is density in kg/m³, and V is the velocity of the fluid in the channel in m/s.

$$\Delta P = \left(f \frac{L}{D_h} + \sum K_{L,i} \right) \left(\frac{\rho V^2}{2} \right) \quad 34$$

Because the cooling channels are assumed to be of rectangular cross section the hydraulic diameter is defined as Equation 35 where A is the cross-sectional area of the channel in meters and P is the perimeter of the channel cross section in meters.

$$D_h = \frac{4A}{P} \quad 35$$

To determine the friction factor, we must first solve for the Reynolds number in the channel as shown in Equation 36, where Re is the Reynolds number, and ν is the kinematic viscosity of the fluid in m²/s.

$$Re = \frac{D_h V}{\nu} \quad 36$$

The transition to turbulent flow occurs at Reynolds numbers around 2300. To determine if the flow in the cooling channels is laminar or turbulent we calculate the Reynolds number for both air and liquid cooling for the range of flow rates we would be testing. This includes up to 12 liters per minute of liquid cooling and 3000 m³/hr for air cooling. We found that the liquid and air cooling channels typically yielded Reynolds

numbers around 100 and 1000 respectively, thus we assumed that all flow in the cooling channels is laminar.

Now that the flow is known to be laminar, the friction factor can be solved via Equation 37 where beta is a constant that ranges from 61-96 depending on the channel dimensions [69].

$$f = \frac{\beta}{Re} \quad 37$$

Additionally, the minor loss coefficients were taken from literature for both sharp turns and pipe entrances and exits. These values are shown in Table 7. Based on pictures of the Chevy Volt cooling fin (Figure 20) we assume that each cooling fin has four turns and one entrance and one exit. This leads to a total minor loss coefficient of 6.9. For air cooling we assume each cooling channel has one sharp entrance and sharp exit, which yields a minor loss coefficient of 2.5.

Table 7 – Minor loss coefficients for pipe flow from literature [69]

	Sharp 90°Bend	Sharp Pipe Entrance	Sharp Pipe Exit
Minor Loss Coefficient (K _L)	1.1	0.5	2

To calculate the power associated with pumping of fluid in the circuit, Equation 38 defines the ideal power consumption in watts for a given pressure drop (ΔP) in Pascals and mass flow rate (\dot{m}_f) in kg/s [70].

$$Power_{ideal} = \Delta P \cdot \dot{m}_f \quad 38$$

To convert from an ideal power consumption to a more realistic power consumption we account for inefficiencies of the pump or fan with Equation 39, where γ is the efficiency of the device as a percentage [70].

$$Power_{real} = \gamma \cdot Power_{ideal} \quad 39$$

Typical values for centrifugal pumps and fans were taken from reference for analysis and are shown in Table 8.

Table 8 – Typical values of pump and fan efficiencies from literature

	Centrifugal pumps	Axial Fan 5in diameter
<i>Typical Efficiency Range</i>	60-85% [70]	25-45% [71]

3.5.1 Validation

To validate our pressure drop calculations we attempted to replicate the results from Chen et al. (2016) who calculated pressure drops for both liquid and air battery cooling

channels at various mass flow rates with a CFD model. The parameters for the cell and cooling channels are the same as those shown previously in Table 5. Figure 55 shows the comparison of the results, which match closely, and our pressure drop model is assumed valid.

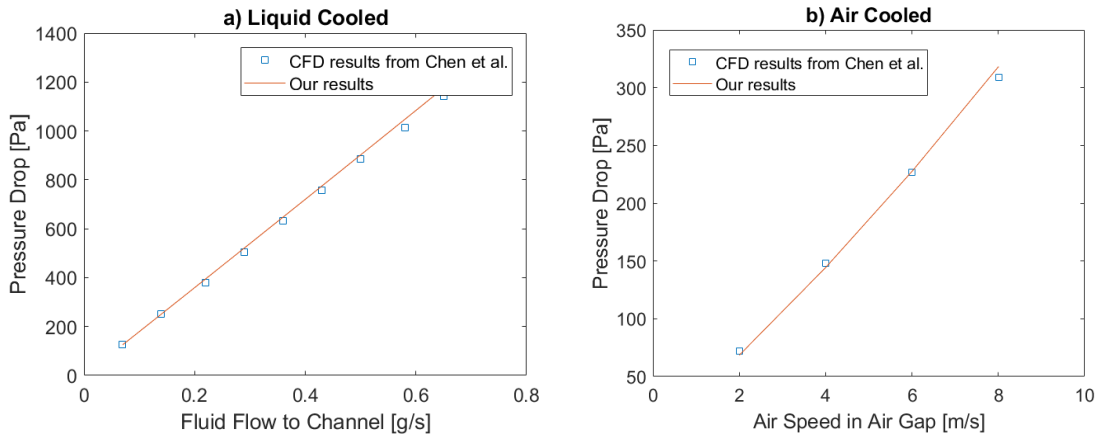


Figure 55 – Comparison of results from our model and the CFD model from Chen et al. for coolant channel pressure drop of a liquid fin cooled battery (a) and an air cooled battery (b)

3.6 Degradation Model

Part of our analysis is to investigate the expected lifetime of the second use energy storage devices and what effects different thermal management strategies have on that life time. To model degradation in EV battery cells in study we adopt the semi-empirical model proposed by Xu et al. 2018 [72]. This model was chosen because it was fit to test data on a lithium-manganese-oxide (LMO) battery which is the same chemistry as the EV battery cells in study, and because it was fit to data extending out to ten years which is more than most other studies.

The model is formed by the following equations. Equation 40 expresses the loss in capacity, L , expressed as a percent with respect to cycles, in terms of both calendar and cycling fade, where t_{cyc} is the time it takes to complete one cycle. Equation 41 represents calendar fade which is a function of time (t) in seconds, SOC, and temperature (T) in kelvin, where k_t is an experimentally derived constant. Equation 42 represents the cycling fade in terms of the number of cycles (N), DOD, SOC, and temperature. Equations 43-45 represent stress factors which effect the rate of cycling and calendar fade. Equation 43, is the stress factor for SOC where SOC_{ref} is the reference SOC, and k_{soc} is an experimentally derived constant. Equation 44, is the stress factor for temperature where T_{ref} is the reference temperature in kelvin, and k_T is an experimentally derived constant. Equation 45, is the stress factor for DOD where k_{DOD1} , k_{DOD2} , and k_{DOD3} are experimentally derived constants.

$$\frac{dL}{dN} = (1 - L) * \left(f_{cal}(t_{cyc}, SOC, T) + f_{cyc}(1, DOD, SOC, T) \right) \quad 40$$

$$f_{cal}(t, SOC, T) = k_t t * S_{SOC} * S_T \quad 41$$

$$f_{cyc}(N, DOD, SOC, T) = N * S_{DOD} * S_{SOC} * S_T \quad 42$$

$$S_{SOC} = e^{k_{soc}(SOC - SOC_{ref})} \quad 43$$

$$S_T = e^{k_T(T - T_{ref})\left(\frac{T_{ref}}{T}\right)} \quad 44$$

$$S_{DOD} = (k_{DOD1} * DOD^{k_{DOD2}} + k_{DOD3})^{-1} \quad 45$$

The cycles we will study will include variations in SOC and temperature with time. To calculate an equivalent temperature and SOC stress factor for these cycles we calculate a time averaged stress factor using Equations 46 and 47 where t_i is the initial time in seconds, t_f is the final time in seconds, and $SOC(t)$ and $T(t)$ is state of charge and temperature as a functions of time.

$$S_{SOC_avg} = \frac{1}{t_f - t_i} \int_{t_i}^{t_f} e^{k_{soc}(SOC(t) - SOC_{ref})} dt \quad 46$$

$$S_{T_avg} = \frac{1}{t_f - t_i} \int_{t_i}^{t_f} e^{k_T(T(t) - T_{ref})\left(\frac{T_{ref}}{T(t)}\right)} dt \quad 47$$

3.7 Case Studies for Performance in Realistic Scenarios

3.7.1 Summary

To predict the performance of our home storage device, we simulate its use in single-family homes for three US locations. The locations chosen were Phoenix, Arizona; Los Angeles, California; and Chicago, Illinois, which represent a wide range of weather conditions and utility rates. For each location, ambient temperature and solar irradiation is collected from the National Renewable Laboratories' Typical Meteorological Year (TMY) database, which represents typical conditions in these locations. The data represents one full year but because it is typical of long term behavior, results can be extrapolated to multiple years. House energy demand was taken from a data set from the Department of Energy which represents typical load conditions based on the TMY dataset. These datasets are on an hourly level, but it was deemed necessary to include sub-hourly variation to more appropriately capture how the storage system is used. Thus, methods are developed to generate synthetic sub-hourly variation for both solar irradiation and household energy use. A simple control algorithm is developed to determine when to charge and discharge the battery and run the thermal management system. The thermal and electrical models are run according to the chosen charge and discharge schedule. Results are processed to predict the devices performance in terms of decreased grid reliance, energy cost savings, and amount of vehicle fast charging delivered,

3.7.2 *Household Demand and PV Modelling*

A main function of our home energy storage device is to store solar power when solar generation is higher than household demand and use it to power the home when demand is higher than generation. To study this effect, we need to model both household demand and solar generation.

3.7.2.1 Data Source

For solar irradiance and ambient temperature data we used NREL's Typical Meteorological Year database (NREL TMY, 2005). This database includes weather data for a typical year at thousands of locations across the US. Each dataset for a particular location is constructed by concatenating months from 1991-2005 that are considered most typical, by the statistical methods documented in the TMY user manual [73]. Because the data represents typical conditions, the dataset for one year is meant to represent operation of systems over a long period of time.

For residential electricity load data, we used the Department of Energy's "Commercial and Residential Hourly Load Profiles" (Department of Energy, 2013). This dataset is created by applying building energy models to the TMY data set to create a typical house load profile. Because it is based on TMY data, the DOE residential load profiles should pair well with temperature and solar data, so correlations like ambient temperature's effect on electricity load are already present in the data. The house parameters used in the model to generate the data are shown in Figure 56. One change we made to the dataset was to assume the homes would be 100% electric and thus we converted any gas usage for water or space heating to an equivalent electrical load by assuming an

efficiency of 80% for gas appliances and a COP of 3.5 for an equivalent electric heat pump [74].

	Selected Building Fuel Types				
	Very Cold/Cold	Mixed-Humid	Mixed-Dry/Hot-Dry	Hot-Humid	Marine
Space Heating	Natural Gas	Natural Gas	Natural Gas	Electric	Natural Gas
Air Conditioning	Yes	Yes	Yes	Yes	No
Water Heating	Natural Gas	Electric	Natural Gas	Electric	Natural Gas
	Selected Building Structure Types				
	Very Cold/Cold	Mixed-Humid	Mixed-Dry/Hot-Dry	Hot-Humid	Marine
Total Size (sq. ft.)	2696	2546	2000	2023	2090
Urban and Rural	Urban	Urban	Urban	Urban	Urban
Metropolitan and Micropolitan	Metro	Metro	Metro	Metro	Metro
Number of Stories / Levels	1 Story	1 Story	1 Story	1 Story	1 Story
Major Outside Wall Construction	Siding (Aluminum, Vinyl, Steel)	Siding (Aluminum, Vinyl, Steel)	Stucco	Brick	Wood
Major Roofing Material	Ceramic or Clay Tiles	Ceramic or Clay Tiles	Ceramic or Clay Tiles	Ceramic or Clay Tiles	Ceramic or Clay Tiles
Foundation/Basement of Single-Family	Basement	Concrete Slab	Concrete Slab	Concrete Slab	Crawlspace
Bedrooms	3	3	3	3	3
Full Bathrooms	1	1	2	2	1
Half Bathrooms	None	None	None	None	None
Basement Single-Family Homes	Yes	No	No	No	No
Finished Basement	No	No Basement	No Basement	No Basement	No Basement
Type of Glass in Windows	Double-pane Glass	Double-pane Glass	Single-pane Glass	Single-pane Glass	Double-pane Glass

Figure 56 – Parameters used to create the DOE residential load profiles [75]

3.7.2.2 Justification for Adding Sub-Hourly Variation

Both datasets have a temporal resolution of one hour, however household demand and solar irradiance can vary widely over the course of an hour which will affect our analysis for energy storage. For household demand, most household appliances, such as HVAC systems, water heaters, clothes washer/dryers, etc., operate with on-off schedules in intervals far shorter than one hour. For example, Figure 57 shows high resolution energy demand data for a house with the specific appliance loads marked. The sporadic on-off nature of each appliance leads to a total load profile that includes much more variation than

an hourly averaged load profile would suggest. This is illustrated in Figure 58, which compares 5-min load data to hourly averaged data.

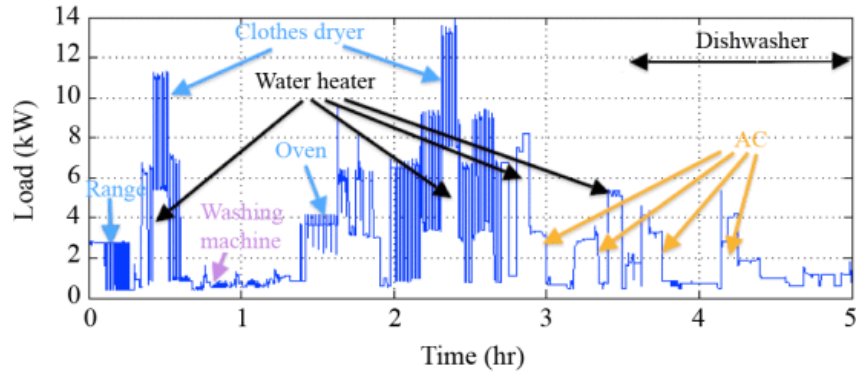


Figure 57 – Example house load profile with appliances marked [76]

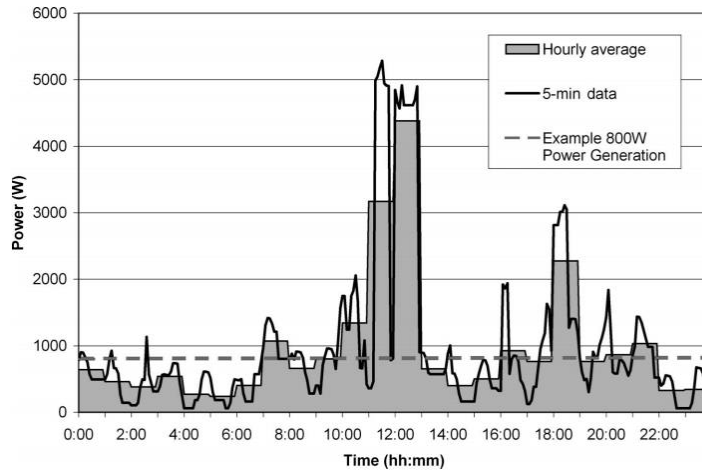


Figure 58 – Comparison of 5-min load data to hourly averaged load data [77]

In a similar nature, PV generation can also vary periodically due to cloud cover. Such variation may be muted for large grid-level solar installations, but not so for small footprint rooftop solar installations [78]. These variation can be important for the analysis of certain renewable energy systems [78, 79].

This sub-hourly variation is important when estimating the usage of energy storage systems, as illustrated in the simplified example shown in Figure 59. Figure 59a shows a hypothetical load and solar generation averaged over an hour. Figure 59b and c show different higher resolution datasets that the hourly averaged data might represent. By solely looking at the hourly averaged data, it appears that there is more than enough solar generation to offset the load, however Figure 59b shows a situation in which the true load and solar generation are completely out of phase with one another. This would be a situation where clouds block the sun at the same time a high-power appliance is turned on. In such a scenario the solar generation can only meet the load half of the time, the rest of the time power would have to be pulled from the grid. Although this exact scenario is unlikely, it is also unlikely that variation in solar and load will match exactly, as shown in Figure 59c. This is the best-case scenario in that the grid usage matches what would be estimated from the hourly averaged data. Because, any real data will exist between these hypothetical best and worst cases, we can say that using hourly averaged data will almost always underestimate the temporal disparity between residential demand and residential solar generation, and similarly will underestimate the amount of energy storage usage.

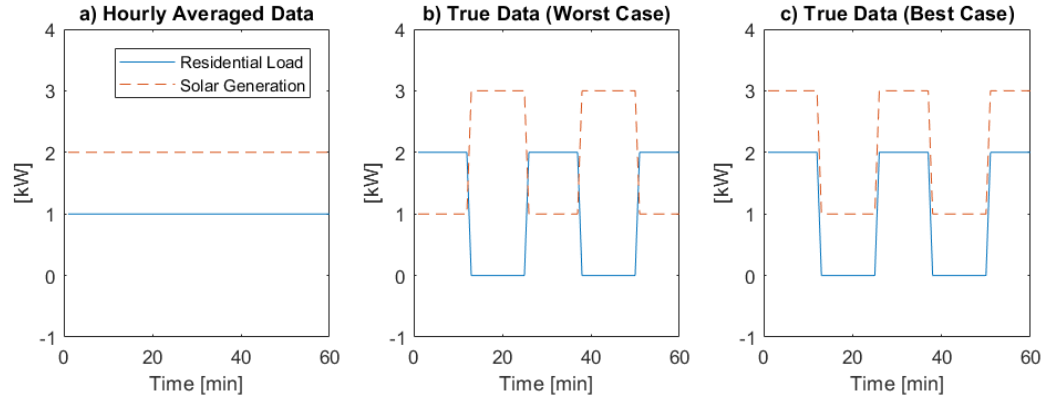


Figure 59 – Example of sub-hourly variations effect on energy storage use

For these reasons, it is clearly important to use sub-hourly data for accurate estimation of how our energy storage device will be used. Thus, we decided to add synthetic variation to our hourly datasets.

3.7.2.3 Generating Sub-Hourly Variation in Data

For adding variation to the solar irradiation data, the model proposed by McCracken (2011) was used, which involves stochastic generation of synthetic 5-min irradiance from hourly irradiance data through a Markov chain process [78]. The model takes the coordinates, elevation, and the average monthly temperature and humidity for a specific location and uses this to estimate the variation in the irradiance. An example of the model output versus the TMY hourly data is shown in Figure 60 for a cloudy day in Los Angeles.

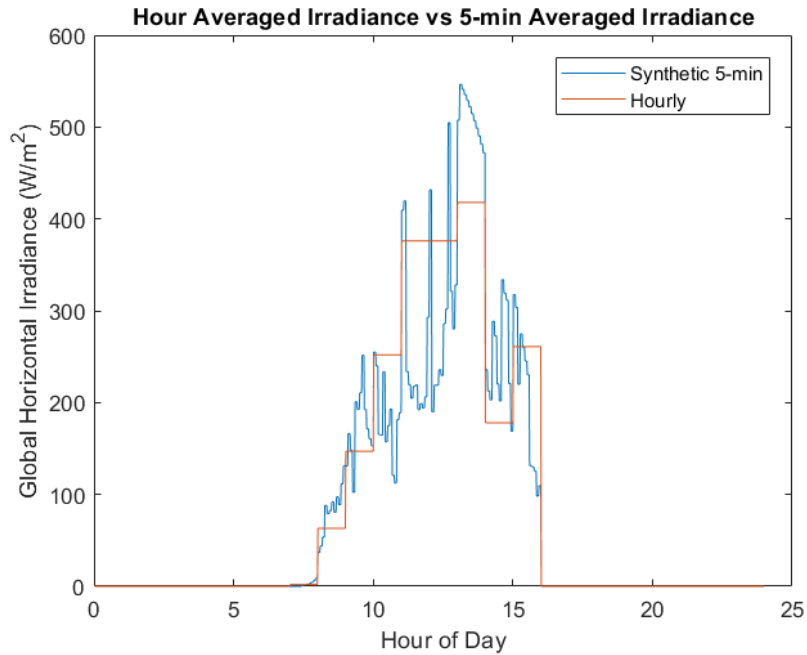


Figure 60 – Example of TMY hourly data vs 5-min synthetic model output

To add synthetic sub-hourly variation to the residential electricity data, we superimposed different appliance load profiles at a high resolution on top of the hourly data. First we collected appliance load profiles from Pipattanasomporn et al (2014) [76], for an AC unit, a heat pump, a refrigerator, a domestic hot water heater, and a clothes washer/dryer, and a stove. Then we used the energy demand predicted for heating, cooling, and large appliances from the DOE dataset to decide where to overlay the appliance load profiles. The method for doing so goes as follows. For each hour, if the hourly data includes energy expended on the AC unit then the load profile of a single AC run is overlaid on that hour at a randomly selected starting point. The AC runs at a constant power draw and the length of time the AC runs is set such that the total energy used equals that seen in the hourly data. An identical method is used for the hot water heater and the heat pump used

to heat the house. For the clothes washer/dryer and stove, if the amount of appliance usage from the hourly data is low, then only one of the devices load profiles is included. If the appliance load is high (>90% of maximum appliance load for year) then both devices load profiles are overlaid for the hour. The refrigerator is slightly different in that it is assumed to run constantly throughout the year in cycles of 7 minutes on and 20 minutes off. For all cases where an appliance load is added, the rest of the load for the hour is reduced such that the total energy consumption for the synthetic data matches the energy consumption of the hourly data.

An example of the output synthetic variation of this method for a summer day in Phoenix is shown in Figure 61. Comparing with the house load profile seen in Figure 57 from [76], this result is much closer to a realistic house load profile than the hourly data.

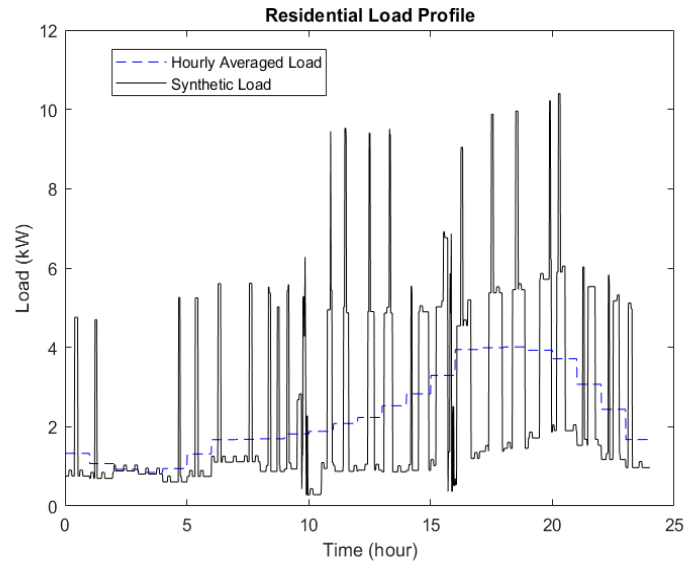


Figure 61 – Example of the synthetic variation in residential demand

3.7.3 Vehicle Charge Modelling

Because DC fast charging of the vehicle is assumed to be of significant value to the customer, we wish to study the actual amount of fast charging a customer can expect from our device under realistic conditions. To do this we generate a vehicle charging schedule for one year based on charging behavior observed in literature.

We collected information from the EV Project which was conducted by the U.S. Department of Energy and studied the driving and charging behavior of Nissan Leaf and Chevy Volt drivers [80]. Figure 62 shows the distribution of the number of charge events per day for the Nissan Leaf drivers in 2011. 82% of these charges were at home versus 82% away from home.

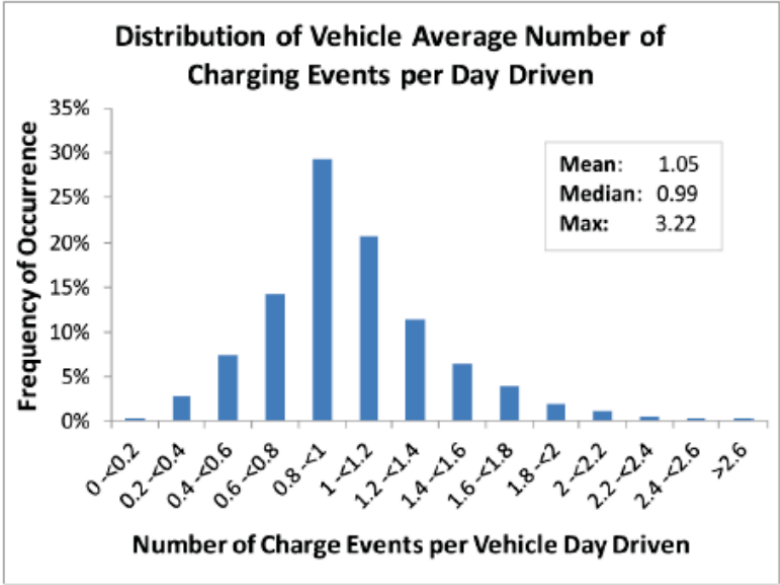


Figure 62 – Number of charge events per day in 2011 for Nissan Leaf owners in EV Project [80]

Figure 63 shows the distribution for the state of charge at the beginning of the charge events for the Nissan Leaf’s in 2011.

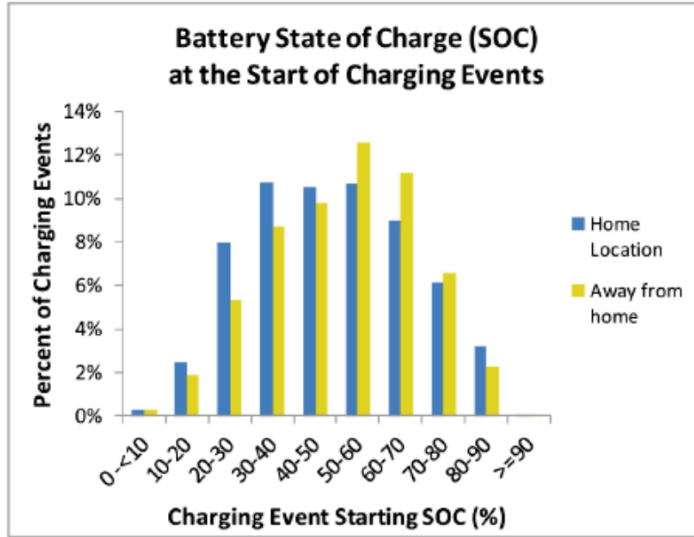


Figure 63 – State of charge at start of charge event for Nissan Leaf owners in EV Project [80].

We adopt this information to form distributions which we sample to generate a synthetic home charging schedule including the SOC at the start of charging. We start by creating a partially geometric distribution for the number of home charging events per day. Based on the distribution in Figure 62 and the fact that 82% of trips are at home, we chose a mean for our distribution at 0.86 trips per day. Two different distributions were created for weekdays and weekends, with the weekends having a higher likelihood of multiple trips per day. The chance of one to ten trips per day follows the geometric distribution and the chance of zero trips is set such that the mean matches the desired mean. Figure 64 shows the probability density functions of these distributions. We can see that on weekdays the driver is likely to have a single charge event whereas on weekends they are more likely to take multiple trips or no trips.

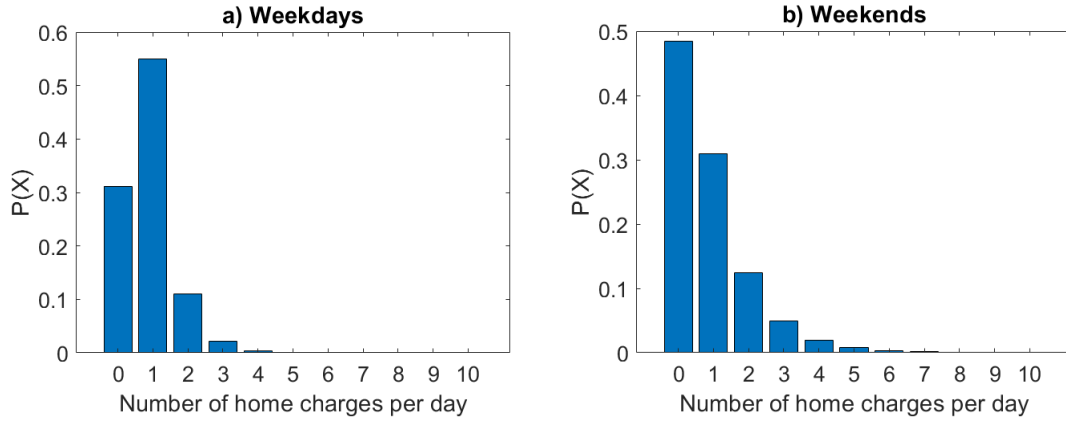


Figure 64 – Probability density functions for number of home charge events per day for weekdays (a) and weekends (b).

Next we assumed that weekday trips are mostly commuting, so the vehicle would charge later in the day on return from work, and that weekend trips are more widely distributed over the day. Thus to choose a start time for the charge event we sampled from two normal distribution: one for weekdays with a mean of 6 PM and a standard deviation of 1 hour, and one for weekends with a mean of 4 PM and a standard deviation of 2 hours. These travel times match observations from the National Household Travel Survey [81]. If there are additional charge events per day then they are also sampled from this distribution and a spacing of 3 hours is added on weekdays and 4 hours added on weekends.

With the charging times generated we add a starting SOC for each charge event by sampling the distribution from Figure 63. Figure 65, shows an example set of charge events created for one week by sampling these distributions, with the first day being Monday. We can see that the weekdays mostly have one charge event per day around 6 PM whereas

Saturday had no events and Sunday had three. The state of charge varies greatly from near zero to nearly full.

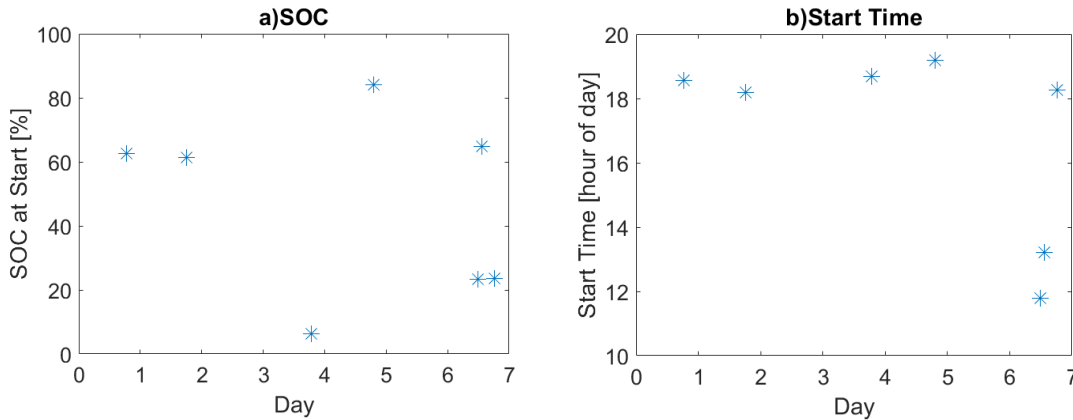


Figure 65 – Example charge events for one week. Figure a) is the beginning state of charge. Figure b) is the start time.

There are limitations to this method. For instance, the data used was collected on Nissan Leaf drivers in 2011, but it is uncertain how closely this would match future EV driver behavior. Higher range EVs and greater accessibility to public chargers would likely change how often EV owners drive and their state of charge on return. Additionally, we are assuming that the start time of a charge event and the beginning state of charge of an event are independent, whereas they are likely not. It is likely that distributions for beginning state of charge would be different between weekends and weekdays, and by time of day.

Additionally we should note that there is concern that frequent fast charging of an electric vehicle can accelerate the rate of its degradation, however it is uncertain to what degree [82]. One study by Idaho National Labs compared Nissan Leafs that were fast charged at 50 kW twice daily to those that were only charged at 6 kW and found minimal accelerated degradation [55]. However, it is yet to be shown if this result matches vehicles outside of the lab environment. We will not analyze degradation of the vehicle battery in this study.

3.7.4 *Simplified Battery Thermal Model*

The active cooling thermal models proposed in Section 3.3 have a relatively small number of nodes, however since we will be modelling performance on the order of a year, it was necessary to produce a simpler thermal model to increase computational speed. Thus, we reduce complexity by assuming the cell is isothermal for both the active liquid and active air-cooled scenarios. This sacrifices accuracy, but we assume it is sufficient for system level analysis. The next two sections will cover the details for the active liquid and air cooled simplified models.

3.7.4.1 Active Liquid Cooled Simplified Model

To derive our simplified model we start with Equation 48 which is an energy balance that matches the change in stored thermal energy of the battery as the sum of heat generated and the heat removed by the coolant, where $T_{batt,avg}$ is the mass-averaged temperature, m is the cell mass in kg, C_p is the cell heat capacity in J/kgK, \dot{Q}_{gen} is the cell heat generation,

$C_{p,f}$ is the heat capacity of the fluid in J/kgK, \dot{m}_f is the mass flow rate of the fluid in kg/s, and $T_{f,in}$ and $T_{f,out}$ are the fluid inlet and outlet temperatures.

$$mC_p \frac{dT_{batt,avg}}{dt} = \dot{Q}_{gen} - C_{p,f} \dot{m}_f (T_{f,out} - T_{f,in}) \quad 48$$

Equation 48 cannot be solved because both the battery averaged temperature and the fluid outlet temperature are unknown. To remediate this, we applied several assumptions. First, we assumed that the fluid outlet temperature is equal to the maximum battery surface temperature. This matches observations from our own model as well as studies from literature and occurs because the heat transfer rate to the fluid is sufficiently high compared to the mass flow rate such that the fluid has enough time to heat up to very near the battery temperature. Applying this first assumption we can form Equation 49 from Equation 48.

$$mC_p \frac{dT_{batt,max}}{dt} \left(\frac{dT_{batt,avg}}{dT_{batt,max}} \right) = \dot{Q}_{gen} - C_{p,f} \dot{m}_f (T_{batt,max} - T_{f,in}) \quad 49$$

Equation 49 now has two unknowns, $dT_{batt,avg}/dT_{batt,max}$ and $T_{batt,max}$. Next, we assume that $dT_{batt,avg}/dT_{batt,max}$ is unity. This is equivalent to saying that the batteries maximum temperature and average temperature change at the same rate. This assumption is valid if the rate of change for temperature variation across the cell is much slower than the rate in the rise of the average temperature of the cell. Applying this assumption produces Equation 50, which can be solved for the maximum battery surface temperature if the heat generation and input fluid temperature are known.

$$mC_p \frac{dT_{batt,max}}{dt} = \dot{Q}_{gen} - C_{p,f} \dot{m}_f (T_{batt,max} - T_{f,in}) \quad 50$$

For our analysis the fluid inlet temperature is not a constant but rather a function of the amount of heat that is dissipated through the liquid to air heat exchanger. To account for this, we assume that the fluid exit temperature from the cell is equal to the fluid inlet temperature to the heat exchanger. This means that there is no heat transfer in the pipe connection between the two which is a conservative assumption. Applying this assumption to Equation 50, gives Equation 51 where H is the heat transfer capacity of the heat exchanger in W/K and T_{amb} is the ambient air temperature.

$$mC_p \frac{dT_{batt,max}}{dt} = \dot{Q}_{gen} - H(T_{batt,max} - T_{amb}) \quad 51$$

3.7.4.2 Active Air Cooled Simplified Model

For active air cooling, later results of the multi nodal model will show that both the internal cell temperature variation and fluid temperature change is typically low (<2°C) for the air speed chosen. Thus, we simplify by assuming the cell is isothermal and losses heat via a constant convection coefficient and with constant ambient air temperature. Thus, the dynamics of battery temperature for the active air cooling scenario can be modeled with Equation 52 below.

$$mC_p \frac{dT_{batt}}{dt} = \dot{Q}_{gen} - h(T_{batt} - T_{amb}) \quad 52$$

3.7.5 *Battery Control Scheme*

Once the load profile, solar generation, and vehicle charging schedule have been generated, we needed to create control algorithms for the battery and thermal management system to define their operation.

Figure 66, shows the logic flow for the battery control algorithm which determines the charge and discharge rate. At the start of each timestep we first check to see if there is vehicle plugged into the device for fast charging. If there is, then the battery is discharged at the DC fast charging rate until depleted or when the car battery is fully charged. If there is no vehicle charging, then we determine if energy storage is required for the home. We shape our algorithm based on the assumption that using the maximum amount of solar power is more important to the user than energy cost savings, thus the algorithm attempts to maximize the amount of solar self-utilization. To do this, we first check the load relative to the PV generation. If the PV generation is greater than the load, we charge the battery with the excess PV power unless the battery is at maximum SOC. If the PV generation is less than the load, we run the excess load off the battery unless the battery is at the “reserve SOC”. The reserve SOC is a point we define above the absolute minimum SOC to save a small portion of the battery capacity only for DC fast charging and backup power. This is to ensure that the vehicle will always have some amount of DC fast charging or backup capability, which we expect to be desirable for the customer. If none of the other conditions are met, then the battery is placed in the “hold” state which means there is no charge or discharge.

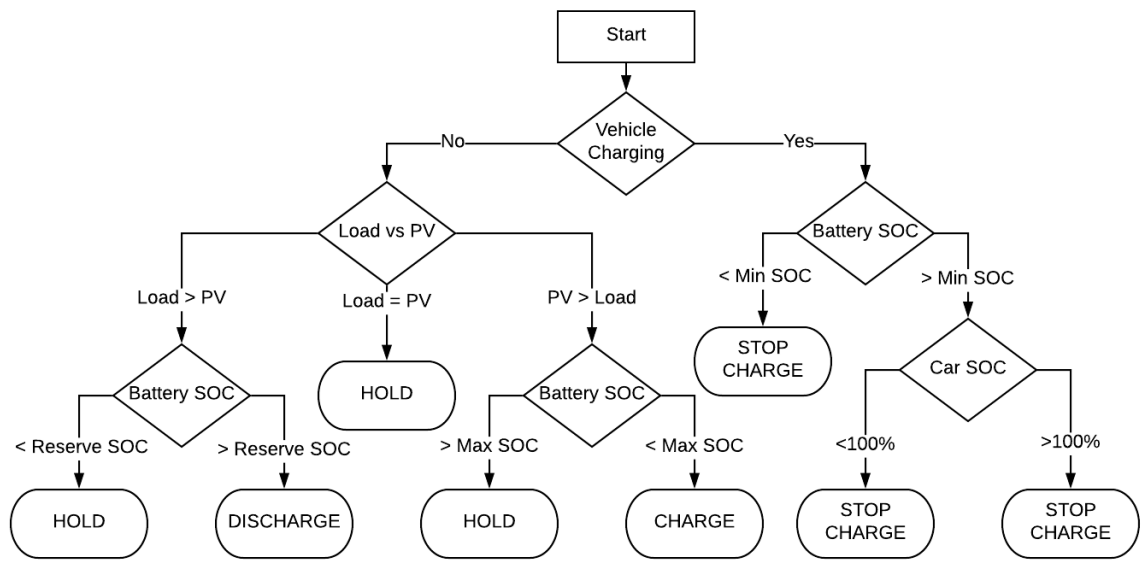


Figure 66 – Battery control algorithm

Figure 67, shows the logic flow for the thermal management system control. It is designed with the assumption that the thermal management system includes either a liquid or air-cooled battery that does not have a chiller but does have a battery heater. This means that the batteries cannot be cooled below ambient temperature, but they can be heated above ambient temperature. For each timestep we start by checking to see if a vehicle is currently being DC fast charged. If it is then we turn on the cooling system unless the ambient temperature is low enough to make heat desirable. If the battery is not currently charging the vehicle then we check the temperature of the battery. If it is below the defined minimum battery temperature (0°C), then the heating system is turned on. If the battery temperature is above the defined maximum battery temperature (50°C) and above the ambient temperature by some “buffer”, then the cooling system is run. The buffer is

included to prevent the system from attempting to cool the battery below the maximum temperature when the ambient temperature is also above the maximum temperature. Because there is no chiller, attempting to cool the battery below ambient temperature would be a waste of energy. When the heating or cooling systems are turned on, they stay on for a predefined duty cycle (30 minutes), to prevent the system from rapidly cycling on and off, and to cool off the battery after DC fast charging. If neither system is turned on, then the thermal management is kept in the 'hold' state till the next time step.

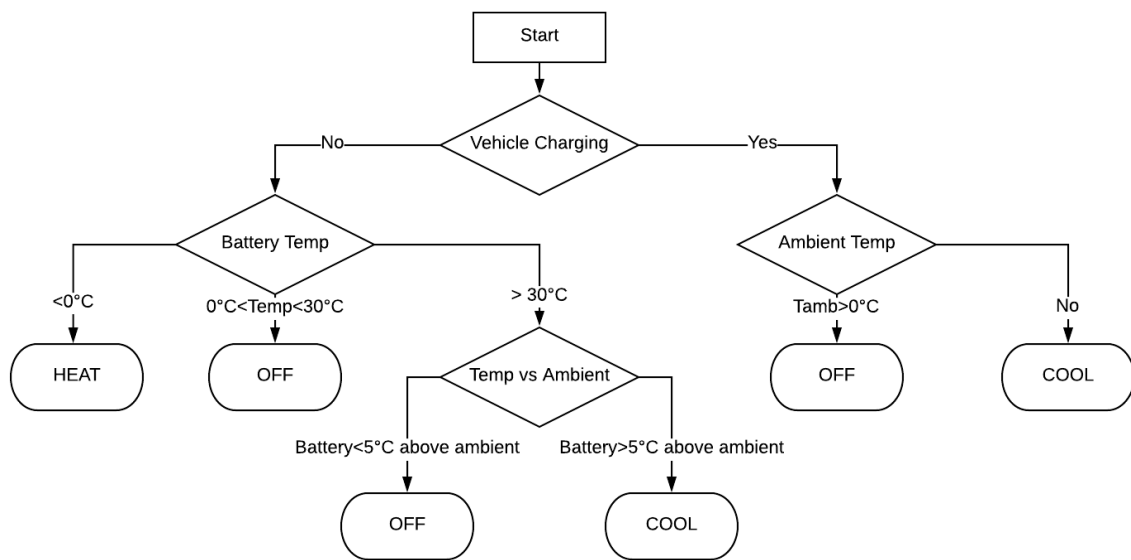


Figure 67 – Thermal management control algorithm

3.7.6 Simulation Process

With the load conditions and control algorithms set for the battery, we now layout the process used to simulate its performance. We run our simulation based on a 5-minute timestep, which was considered a good balance between accuracy and computational speed. For each time step we complete the steps shown in Figure 68. We start by checking the load conditions for the battery. This includes checking the house energy demand, the rooftop solar generation, and checking if a vehicle is requesting fast charging. Then we use the battery control algorithms specified in Section 3.7.6, to determine the amount of power we request from the battery, and the amount of heating or cooling that should be provided by the thermal management system. Once the cooling and power draw is determined, we run our thermal-electrical model to calculate the power delivered or received by the battery, and the change in battery SOC and temperature. Note that the timesteps used to numerically solve the thermal-electrical model may be smaller than the 5-minute timestep used by the whole simulation. Finally, we add the battery power consumed or delivered to the home or vehicle.



Figure 68 – Simulation process

Equations 53 through 55 outline how the energy flows are calculated in our system. If the power is requested from the battery to power the house the amount of power is defined by Equations 53. The battery attempts to match the net load of the house, which is the power demand of the house (P_{house}) minus the solar generation (P_{PV}) while taking into account the efficiency of the inverter ($\eta_{inverter}$)

$$P_{battery,requested} = \frac{P_{house} - P_{PV}}{\eta_{inverter}} \quad 53$$

The thermo-electrical model returns the battery power delivered ($P_{battery,delivered}$) which may be different than the power requested from the battery if SOC or temperature limits are reached mid-timestep. Then we update the amount of power requested from the grid via Equation 54 by adding the power delivered by the battery as well as the power consumed by the thermal management ($P_{thermal}$) and battery controls system ($P_{controls}$)

$$P_{grid} = P_{house} - P_{PV} - P_{battery,delivered} + P_{controls} + P_{thermal} \quad 54$$

If the battery is supplying charging to a vehicle then the power requested from the battery is set to the specified DC fast charging rate and the car's SOC is updated via Equation 55, where $\frac{dSOC_{car}}{dt}$ is the change in car state of charge per hour, η_{DCDC} and η_{car} are the efficiency of the DCDC converter and car battery respectively, and $Q_{car kWh}$ is the capacity of the car in kilowatt hours.

$$\frac{dSOC_{car}}{dt} = \frac{P_{battery}}{(\eta_{DCDC} * \eta_{car})(Q_{car kWh})} \quad 55$$

3.7.7 Simulation Parameters

In this section we cover the parameters chosen for our case study simulation and the justification for each. Tables 9-12 summarize the parameters chosen for the thermal management, battery controls, power electronics, and electric vehicle respectively.

Table 9 – Simulation parameters for thermal management

Parameter	Unit	Value chosen	Justification
Heat Exchanger Cooling Capacity	W/K	170	Good balance of cooling performance, cost, and size
Battery Heater	W	500	Sufficient to maintain battery temperature above 0°C
Heater Efficiency	-	0.9	
Duty Cycle	Minutes	30	Long enough to cool down battery post DCFC
Temperature Buffer	°C	5	Allows operation up to 45°C
Battery Shut-off Temperature	°C	50	Sufficiently below thermal runaway temperature
Minimum Battery Temperature	°C	0	Based on recommendations for battery temperature range
Maximum Battery Temperature	°C	30	

Table 10 – Simulation paramters for battery controls

Parameter	Unit	Value chosen	Justification
Maximum SOC	-	100%	Based on [27]
Minimum SOC	-	20%	Based on [27]
Reserve SOC	-	50%	Chosen as a balance between DCFC and home energy storage
Vehicle Charging Rate	kW	50	Typical DC fast charging speed

Table 11 – Simulation paramters for power electronics

Parameter	Unit	Value chosen	Justification
Inverter efficiency	-	97%	Based on currently available battery inverters [43, 83, 84]
DC/DC converter efficiency	-	97%	Based on currently available high power DC/DC converters [85]
Level 2 charging rate	kW	7	[15]

Table 12 – Simulation paramters for electric vehicle

Parameter	Unit	Value chosen	Justification
Capacity	kWh	40	Gen 2 Nissan Leaf battery capacity [86]
Charging efficiency	-	96%	Assuming only resistance losses for 50 kW charging of Nissan Leaf [51]
Range per charge	Miles/kWh	3	Based on Department of Energy estimates [87]

3.8 Handling Uncertainty

There are many parameters in our analysis that are uncertain, which yield uncertainty in our results. For instance, there is a large amount of uncertainty in the state of health of the battery packs at end of vehicle life as none of the vehicle being analysed have reached this point and thus they cannot be directly measured. Additionally, there is uncertainty in parameters like the heat capacity of the cell and convection rates which will generate additional uncertainty.

We incorporate these uncertainties by modelling them as probabilistic distributions, which we pair with Monte Carlo simulations to estimate the uncertainty in the thermal model's output and the model's sensitivity to different parameters. In this section we will cover how we defined our uncertainty distributions and our justification for doing so. We also define the base case for the parameters we use for analysis when not accounting for uncertainty.

3.8.1 *Estimating Battery Health at End of Vehicle Life*

An important factor affecting the performance of the reused electric vehicle batteries is their health at end of vehicle life in terms of capacity remaining and resistance growth. All 2013 model year vehicles we are analysing have yet to reach the 10-year mark, when we assume a significant fraction of the vehicle battery will reach end of life. This is consistent with the average life reported for automobiles [88]. Thus, the health of these future batteries is not directly measurable, and we must make a prediction. To inform our

prediction, we reviewed other predictions from literature, as well as laboratory testing on the vehicles, and vehicle warrantee information.

Table 13 summarizes the battery warranties for the three vehicles selected. The batteries are all warrantied for a specific period against “non-gradual capacity loss”, which most take to mean any drop below 70% of original capacity although this is not directly specified in the warranties [89]. The Volt and the Focus have longer battery warrantee periods than the Leaf, which likely means it is expected that Leaf batteries will degrade faster, probably due to its passive thermal management system.

Table 13 – Battery warranty for selected electric vehicles

	Battery Warranty	Reference
<i>2013 Chevy Volt</i>	8 years or 100,000-mile	[4]
<i>2013 Ford Focus</i>	8 years or 100,000-mile	[90]
<i>2013 Nissan Leaf</i>	5 years or 60,000-mile	[89]

For experimental data on these vehicles we pulled from Idaho National Labs (INL) Advanced Vehicle Testing Project which conducted battery test of 4 vehicles of each model at various stages in their age and mileage. Table 14, shows the approximate testing conditions for each of the electric vehicles. Note that the vehicles were driving in a very hot climate, which will accelerate their degradation relative to most other locations.

Table 14 – INL Advanced Vehicle Testing conditions

	Unit	2013 Volt	2013 Focus	2013 Leaf
<i>Testing Period</i>	years	3	1.3	2.5
<i>Miles Driven</i>	mi	130,000	17,000	24,000
<i>Full Electric Miles Driven</i>	mi	15,000	17,000	24,000
<i>Mixed Electric and Gasoline Miles</i>	mi	33,000	NA	NA
<i>Average Ambient Temperature</i>	C	30	NA	30

Figure 69, shows the measured drop in relative battery capacity in each vehicle over the course of the test. In general, the Volt degraded the slowest with only around a 10% drop in capacity over 3 years and 100,000 miles. The Focus and Leaf degraded more rapidly, likely because they are BEVs rather than PHEVs. Also, the Focus seems to degrade slightly slower than the Leaf, likely due to its active thermal management system.

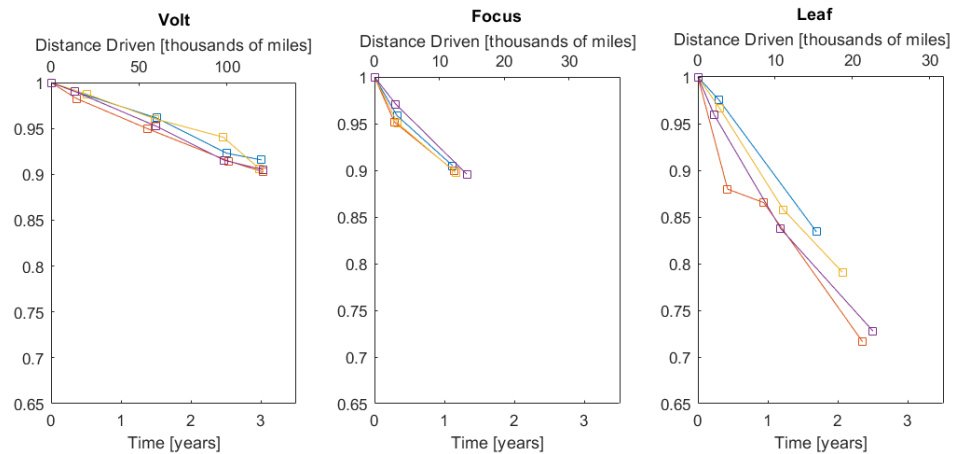


Figure 69 – Relative capacity loss for vehicles in INL’s Advanced Vehicle Tests

Figure 70, shows the relative resistance growth of the vehicles during the INL testing. In general, the behavior does not follow a clear trend like the capacity loss, with the measured resistance decreasing at points. This could be due to break-in mechanisms which can decrease resistance [2]. However, it appears the Leaf might have an accelerated rate of resistance growth but there is not enough data to confirm this.

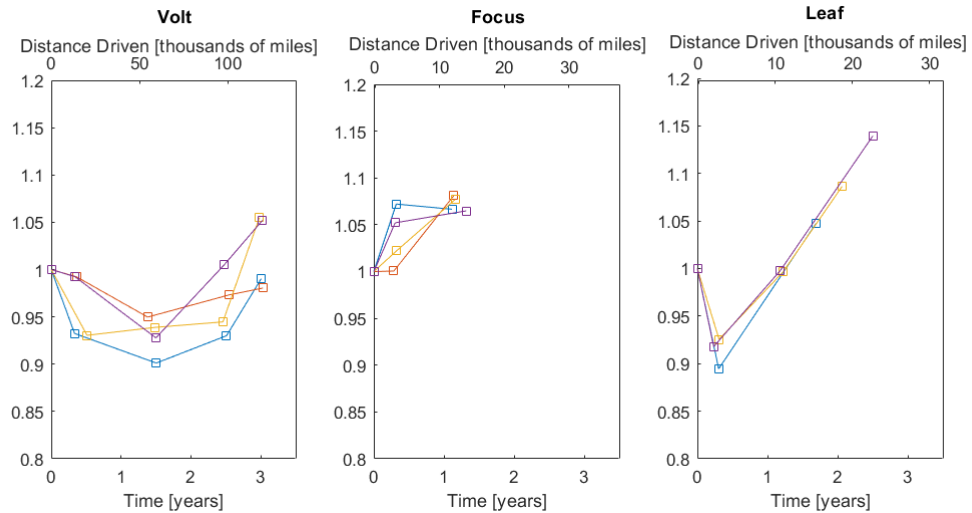


Figure 70 – Relative resistance growth for vehicles in INL’s Advanced Vehicle Tests

For estimations of battery age from literature we turned to Neubauer et al. (2015) who estimated the amount of aging in electric vehicles by simulating the battery degradation with realistic driving profiles in various locations [4]. They simulate both a BEV with 75 miles range (similar the Focus and Leaf) and a PHEV with 20 miles range (similar to the Volt), both having an active thermal management system. Table 15,

summarizes their results for battery degradation and resistance growth for these vehicles at various locations after a 15-year vehicle life.

Table 15 – Estimations from Neubauer et al (2015) for battery health at end of vehicle life

		Geographic Location		
		Minneapolis, MN	Los Angeles, CA	Phoenix, AZ
Capacity Loss	BEV	24.7%	28.8%	29.8%
	PEV	30.2%	32.9%	33.4%
Resistance Growth	BEV	27.5%	32.3%	35.2%
	PEV	56.1%	64.1%	65.4%

We combine the information we have gathered to form a hypothesis on battery health. Starting with the Volt, from the INL testing the Volt only lost 90% capacity after 3 years and miles in an extremely hot environment. Although the vehicles reached 100,000 miles, Neubauer et al 2015 predict calendar fading to dominate ageing, thus a vehicle at 10 years of age will likely have higher capacity loss. However, most location will not see the same temperatures that the INL Volts were tested at and thus will have a slower rate of decline. Thus, we assume for our base case that the Volt will have 80% capacity remaining at EOL. The Focus and Leaf seems to have a steeper decline compared to the Volt in the INL data, but the Focus’s active thermal management system and longer battery warranty suggest it will undergo less degradation than the Nissan Leaf. Thus, we assume for the base case that the Focus will have 70% remaining capacity after 10 years and the Leaf will have 60%.

For resistance growth, the INL test data does not show as clear of a trend for the early years, thus we rely more heavily on the estimate from Neubauer et al. which predicts higher resistance growth in PHEVs versus BEVs. Thus, we assume the Focus and Volt have 30% and 40% of resistance growth in the base case, whereas the Leaf has a higher 60% growth due to its lack of active thermal management. These values are very uncertainty however and thus we include a large range between minimum and maximum values.

Next, we construct uncertainty distributions for the ageing parameters of each vehicle. These distributions are summarized in Table 16. For all vehicles we can be almost 100% certain that some capacity loss and resistance growth will occur, thus the minimum for both is slightly above 0. For capacity loss we assume that the maximum capacity fade is 50%, as at this level, second-life usage is impractical, and the batteries will likely be recycled instead.

Table 16 – Base case and uncertainty distributions for vehicle ageing

Parameter	Distribution	2013 Ford Focus Electric			2013 Chevy Volt			2013 Nissan Leaf		
		Minimum	Base Case	Maximum	Minimum	Base Case	Maximum	Minimum	Base Case	Maximum
Capacity Loss	Custom	15%	30%	50%	5%	20%	50%	15%	40%	50%
Resistance Growth	Custom	10%	30%	130%	5%	40%	140%	20%	60%	150%

Because we predict the results to be particularly sensitive to these ageing parameters it was determined that assigning a distribution such as a normal or triangular distribution would not be accurate. Thus, we generated a custom distribution for these parameters using the methods of elicitation questions, where the likely hood of certain events is determined through a mock betting process to as closely as possible capture our beliefs [91]. The distributions created for both capacity loss and resistance growth are shown in Figure 71 and Figure 72 respectively.

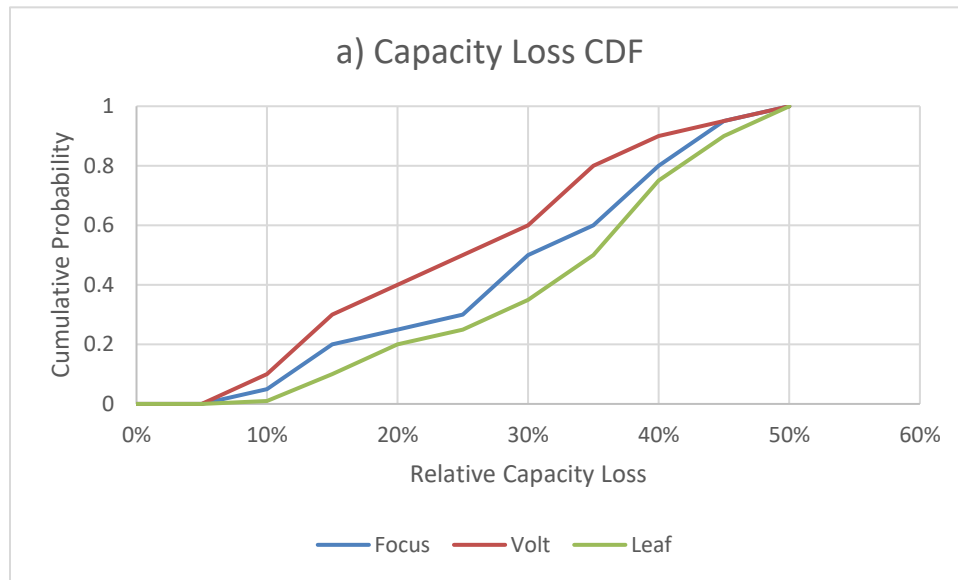


Figure 71 – Uncertainty distribution CDF generated for capacity loss at end of vehicle life

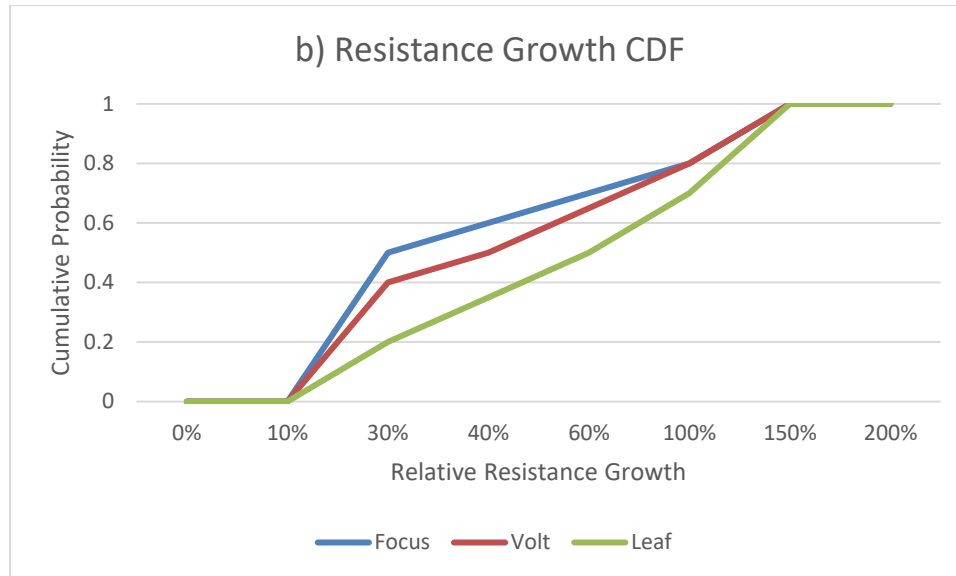


Figure 72 – Uncertainty distribution CDF generated for resistance at end of vehicle life

Note that although we are representing the ageing parameters as a single value with uncertainty, the capacity and resistance of vehicles coming off the road will have their own distribution as each battery will age differently. Future analysis should determine how to best handle this variability, but for this analysis we will consider the uncertainty distributions to model the average case for these parameters.

3.8.2 Uncertainty in Thermal Parameters

In addition to the ageing of the battery there is also uncertainty in the thermal parameters of the cells such as the mass, heat capacity, natural convection rate, and so on. Because we were unable to measure properties like thermal conductivity and heat capacity

we surveyed literature for measurements on other pouch type lithium-ion cells. Although the exact construction of the cells varies, we assume that the thermal properties of our cells are similar to those found in literature. Table 17, summarizes the properties found in the other studies we surveyed.

Table 17 – Thermal properties of large pouch lithium-ion cells from literature

Type of cell	In plane thermal conductivity (K _{xy}) [W/mK]	Through plane thermal conductivity (K _{xy}) [W/mK]	Heat Capacity (C _p) [W/mK]	Reference
20 Ah LiFePO ₄ Pouch Cell	25	1	1027	[92]
25 Ah LMO Pouch Cell	21	0.48	1243	[93]
Unspecified Large Pouch Cell	45	0.65	1000	[94]
20 Ah NMC Pouch Cell	26.57	0.97	-	[95]
10 Ah LiFePO ₄ Pouch Cell	18.4	0.34	1200	[96]

The results of these studies were used to generate the base case and uncertainty distributions for the thermal parameters of the electric vehicle cells as shown in Table 18. The thermal conductivity and heat capacity were assumed close to the average of the results from Table 17, with a slightly higher range of minimum and maximum values. The cell mass was assumed most uncertain for the Ford Focus because it was not directly measured, but all cells include maximum values above the cell mass to account for surrounding thermal masses that may also heat up such as module casings.

Table 18 – Base case and uncertainty distributions for thermal parameters.

Parameter	Distribution	2013 Ford Focus Electric			2013 Chevy Volt			2013 Nissan Leaf		
		Minimum	Base Case	Maximum	Minimum	Base Case	Maximum	Minimum	Base Case	Maximum
Cell Mass [kg]	triangular	0.300	0.359	0.460	0.359	0.359	0.410	0.787	0.787	0.837
Natural Convection Coefficient [W/m ² K]	triangular	1	3	7	1	3	7	1	5	10
In plane thermal conductivity (K _{xy}) [W/mK]	triangular				15	25	50			
Through plane thermal conductivity (K _{xy}) [W/mK]	triangular				0.3	0.7	1.2			
Cell Heat Capacity [J/kgK]	triangular				900	1100	1300			
Active Liquid Convection Coefficient [W/m ² K]	triangular	500	870	1100	500	870	1100	-	-	-
Active Air Convection Coefficient [W/m ² K]	triangular	-	-	-	-	-	-	20	27	35

- Parameters shown for only one vehicle are assumed the same across all vehicles

CHAPTER 4. RESULTS

4.1 Thermal Performance Under Adiabatic Conditions

We start by examining performance of the reused EV packs under adiabatic conditions at various levels of discharge. This gives an estimate for the upper bound on temperature that can be expected since any real scenario will have some amount of heat loss to the environment.

4.1.1 Step Response to Various C-rates

Figure 73 shows the step response of cell temperature to various C rates under adiabatic conditions, using the base case parameters defined in Section 3.7.7. We assume a starting SOC of 100% and an ending SOC of 20% and the simulation is ended once the minimum SOC is reached. The ambient temperature and initial temperature of the battery are both assumed to be 25°C. The resulting temperature profiles all show a slightly nonlinear trend, with the nonlinearity mostly due to the entropic heat generation and less so due to change in resistance with temperature. The temperature rise varies from around 20°C above ambient for the Leaf pack at 4C discharge, to around 3°C for the Volt pack at 1C. For each case, the Leaf and Focus batteries see higher maximum temperatures mostly due to their higher capacity relative to the Volt, which yields higher currents for the same C-rate.

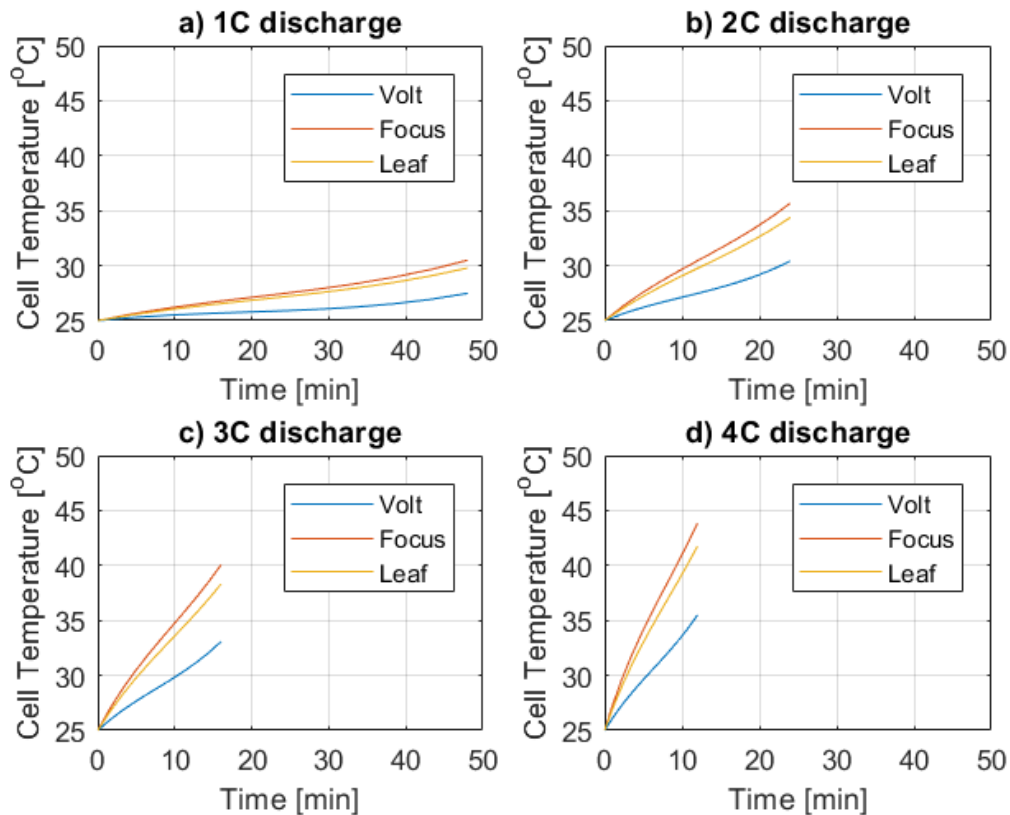


Figure 73 – Battery cell temperature for different rates of discharge under adiabatic conditions under 1C discharge (a), 2C discharge (b), 3C discharge (c), and 4C discharge (d)

For 1C discharge as shown in Figure 73a, the battery temperature rises to less than 5°C above the ambient for all battery packs. This estimate matches results from literature which suggest a batteries temperature rise is limited for batteries under 1C discharge even with no heat loss [97]. This can be attributed to the large thermal mass of the battery relative to the heat generated. Increasing the C-rate to 2C, 3C, and 4C respectively nearly doubles, triples, and quadruples the temperature increase above ambient. This is due to the resistive heat generation being proportional to current squared, while the time spent discharging is

proportional to the inverse of current, meaning the total heat energy generated is nearly linear with current.

4.1.2 Step Response to Various Discharge Powers

Battery cell temperature relative to C-rate is useful for generalized characterization and comparison with literature, but a more useful metric is cell temperature versus the power delivered by the battery. This is shown in Figure 74 for discharges varying from 10 to 100 kW in power measured at load. For a 10 kW discharge, around the maximum that would be required to power a home, the cell temperature rise for the battery packs is minimal as shown in Figure 74a. However, getting into the higher discharge rates that would be required for DC fast charging like 25, 50, and 100 kW, leads to much higher cell temperatures. In general, the Volt pack sees a high rate of temperature increase because it experiences a higher power relative to its energy capacity, compared to the Focus and Leaf. However, the Volt battery also drains earlier, which leads to a lower max temperature relative to the other batteries. Because we assume that the Leaf has degraded more in terms of energy capacity and resistance growth, the Leaf pack sees faster, and higher temperature increases compared to the Focus pack. Still, all batteries see max temperatures between 5 and 15°C above ambient for 25 and 50 kW, which will not lead to unsafe temperatures unless ambient temperatures are very high. Discharging at 100 kW, on the other hand, would very likely lead to dangerous battery temperatures.

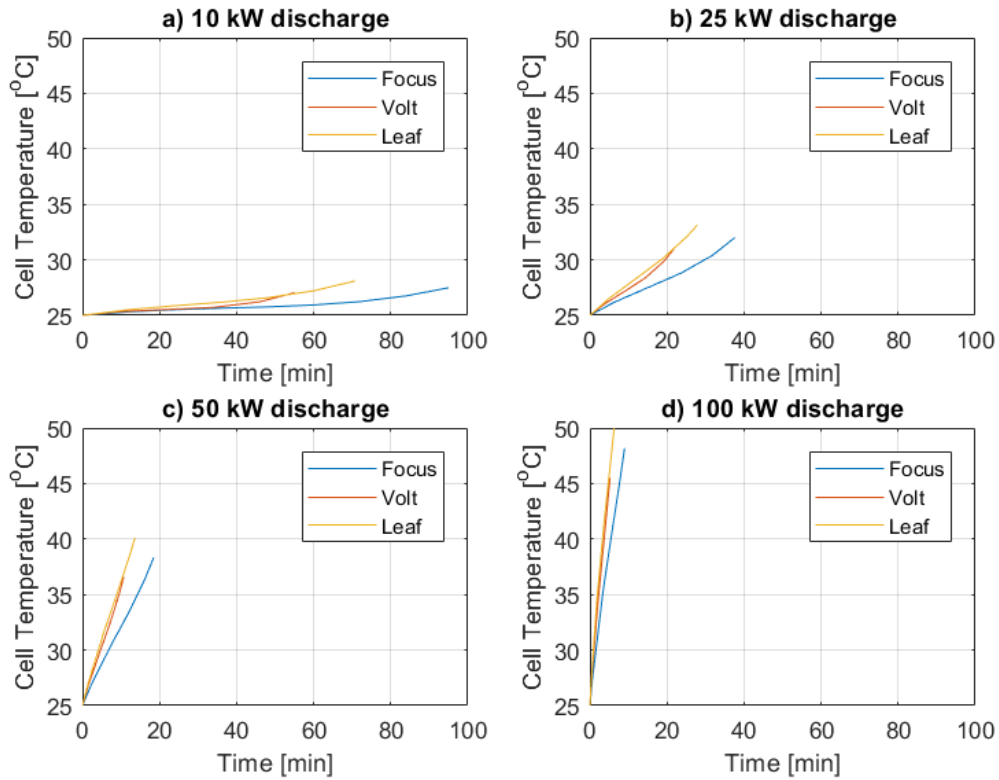


Figure 74 – Battery cell temperature for different rates of discharge under adiabatic conditions under 10 kW discharge (a), 25 kW discharge (b), 50 kW discharge (c), 100 kW discharge (d)

4.1.3 Discussion

The results from the adiabatic analysis suggest that for low power applications like offsetting the electricity demand of a home, the heat generated is small relative to the large thermal capacity of the batteries and thus the temperature rise is small even with no heat loss. This suggests that passive thermal management may be suitable for such applications. For higher power applications, like DC fast charging, the batteries see a larger temperature increase however the limited capacity of the batteries cannot sustain high power discharges

for long before running out of charge. Because such power levels are expected to be brief, passive cooling may still be adequate for 25 kW of discharge or higher at least in terms of the battery not reaching dangerous temperatures. However, such a system may not be able to operate in high ambient temperatures and the high temperatures reached would also affect battery life. Thus, it is still desirable to cool the battery with active thermal management.

4.2 Thermal Performance with Passive Thermal Management

After performing the analysis of the cell temperatures under adiabatic conditions we conducted a similar study but add heat loss due to natural convection to simulate passive thermal management strategy.

4.2.1 Step Response to Various Discharge Powers

Figure 75, shows the step response of each batteries cell temperature for different discharge rates in terms of power delivered at load with passive thermal management. Again, the SOC range was 100%-20% but for these runs the simulation continued after the battery was depleted to simulate the battery cooling down. There is assumed to be no current flow during this cool down period. Comparing with the results from the adiabatic scenario (Figure 74) shows that adding natural convection did not reduce the maximum temperature by a significant amount. This is because the convection coefficients are low, and only a small fraction of the cells surface area is exposed to convection. Additionally, we notice that the batteries are slow to cool down after reaching peak temperature, as the heat stored in the battery is large relative to the heat loss rate due to natural convection.

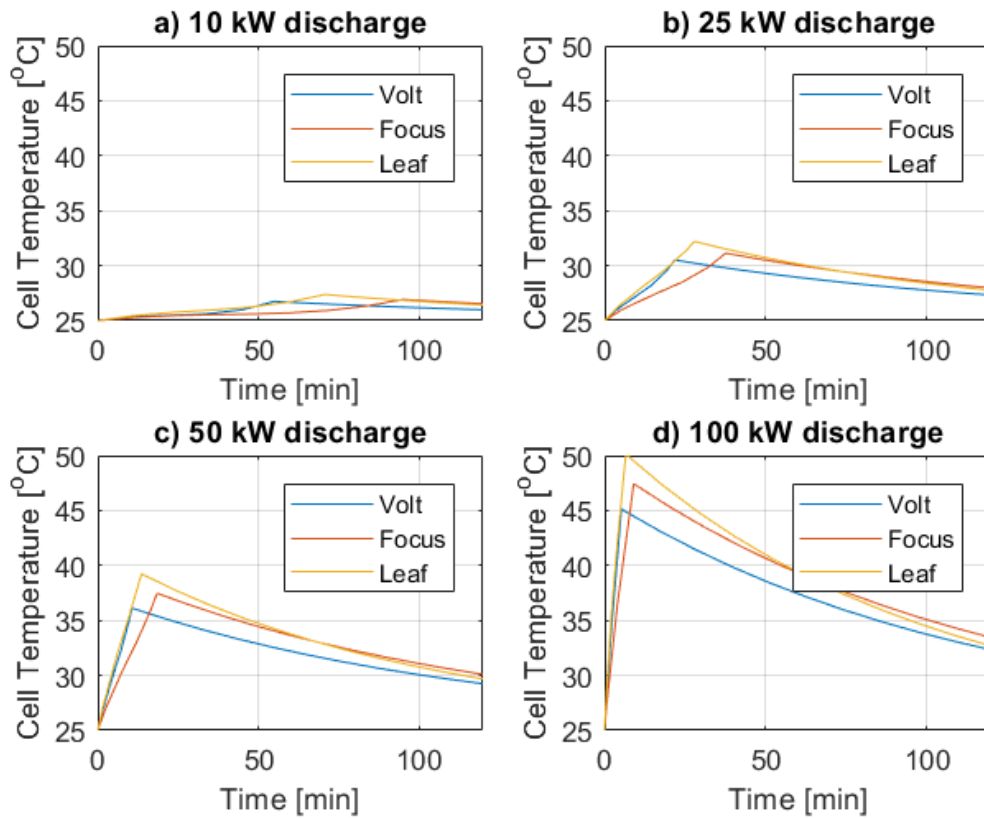


Figure 75 – Battery cell temperature for different rates of discharge under passive thermal management under 10 kW discharge (a), 25 kW discharge (b), 50 kW discharge (c), 100 kW discharge (d)

4.2.2 Cool Down Rate

As mentioned, the batteries take much longer to cool down than to heat up after high discharge with passive cooling. This can be significant, as the time at high temperature needs to be reduced to minimize battery degradation. Thus, we wish to find a way to describe the rate of battery cool down. The solution to the differential equation which describes the cooling of the battery (Equation 15) is an exponential decay with the time constant shown in Equation 56, where m is the cell mass in kg, C_p is the cell heat capacity

in J/kgK, h is the convection coefficient in W/m²K, and A is the heat transfer surface area in m².

$$\tau = \frac{m * C_p}{hA} \tag{56}$$

Using Equation 56, we calculate the time constant for the cooling of the battery cells in hours under the base case for natural convection as shown in Table 19. We can see that the Volt and Focus cells cool slightly slower than the Leaf which is attributed to the higher assumed convection rate from the Leaf cells. At one time constant we can say the cells have lost 63% of their temperature rise relative to ambient, and at four time constants we can say the cells have essentially returned to ambient temperature. Thus, to cool to ambient temperature is expected to take around 8 to 9.5 hours, which is a significant amount of time and may be a drawback to using passive thermal management.

Table 19 – Time constant for cooldown of battery cells

	Volt	Focus	Leaf
Time constant [hr ⁻¹]	2.3	2.3	2.0

4.2.3 *Uncertainty and Sensitivity Analysis*

To incorporate uncertainty into our results we conduct a Monte Carlo simulation with 1000 runs using the uncertainty distributions described in Section 3.7.7. This includes uncertainty in the battery’s remaining capacity, resistance growth, mass, heat capacity, and

convection coefficient. Figure 76 shows the resulting distribution of the max temperature for the three battery packs for a 50-kW discharge. The results show that we can be reasonably certain that the cell temperature will be less than 15°C above ambient temperature for both the Volt and Focus but could be as high as 20°C. The Leaf battery is likely to see higher max temperatures which could be over 20°C above ambient but are more likely to be less than 17°C. Meanwhile, the time constant for cooling is likely between 2 and 5 hours.

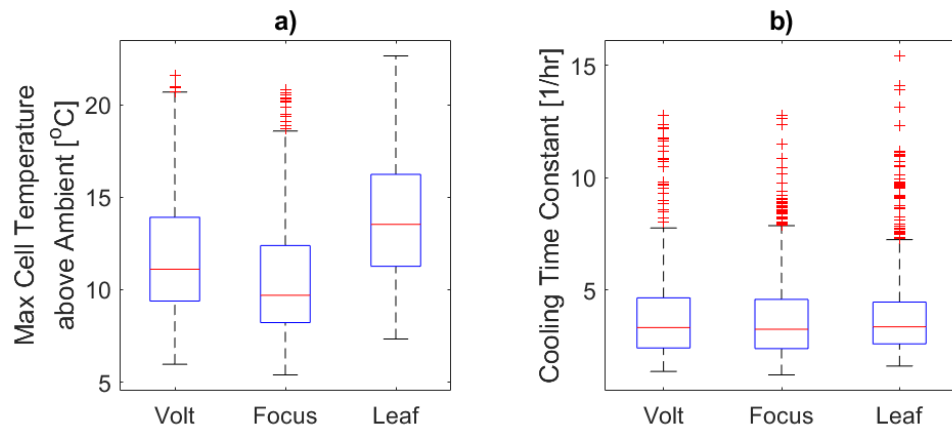


Figure 76 – Distribution of maximum cell temperature (a) and cooling time constant (b) for all monte-carlo runs for step discharge at 50 kW

Figure 77 shows the relative sensitivities of the uncertainties to the resulting max temperature and cool down rate. The uncertainty with the greatest effect on the maximum temperature is the batteries resistance growth, followed by remaining capacity. This highlights the importance of further study into the state of health of these batteries if such a device is to be manufactured. The uncertainty with the greatest effect on cooling rate is

the convection coefficient, and future analysis would benefit from more thorough fluid analysis such as CFD simulations or experimental testing.

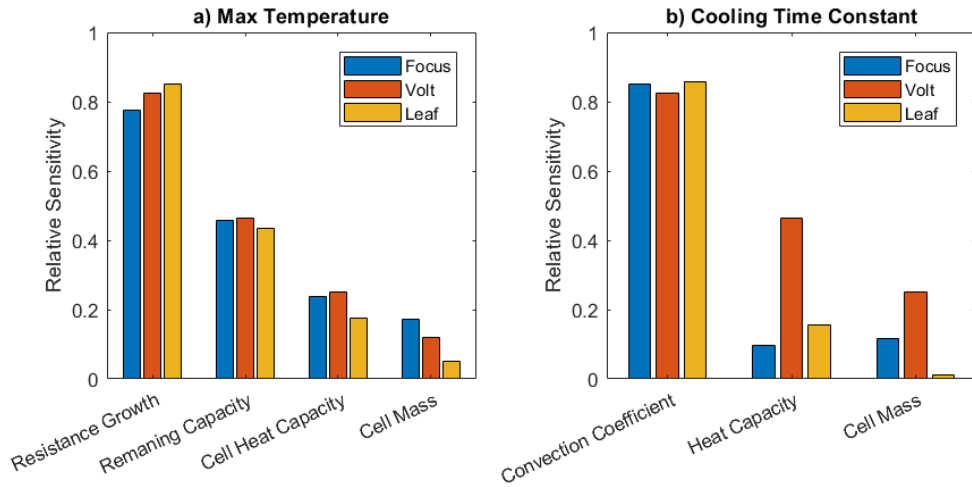


Figure 77 – Sensitivity of (a) max temperature and (b) cooling time constant to uncertainty in parameters

4.2.4 Discussion

The results of the passive thermal management analysis show that the large thermal mass of battery may be able to reduce the temperature rise of fast discharging, even when accounting for uncertainty. However, the relatively low convection rate leads to a long cool down time that leaves the battery at elevated temperatures for a long period of time, which could have a significant effect on battery lifetime and safety.

Additionally, the results are particularly sensitive to resistance growth and remaining capacity which shows the high dependence of the thermal performance of these

batteries to their state of health at end of vehicle life as well as through their second life. Future analysis should focus on these factors for more accurate predictions of thermal performance.





4.3 Thermal Performance with Active Liquid Cooling

Next, we studied the temperature of the cells under various rates of discharge with active liquid cooling. Only the Volt and Focus cells include liquid cooling channels, so the Leaf battery is not included in this analysis.

4.3.1 Step Response to Various Discharge Powers

First, we examined the step response of the Volt and Focus battery packs to different levels of discharge, while circulating coolant through various sized heat exchangers and liquid chillers. The exact models and parameters of heat exchangers we used are shown in Table 20. For each heat exchanger we choose a flow rate of 9.5 liters per minute as flow rate past this point sees diminishing cooling capacity increase. Later analysis will show that pumping of fluid creates relatively low power draw, thus we can choose the flow rate with little concern for additional power consumption.

Table 20 – Heat exchanger and liquid chiller data used for

	Small Heat Exchanger	Medium Heat Exchanger	Large Heat Exchanger	Liquid Chiller
Manufacturer	Advanced Thermal Solutions	Advanced Thermal Solutions	Advanced Thermal Solutions	Liard Technologies
Model Number	ATS-HE24	ATS-HE25	ATS-HE26	MRC300,DH2, DV
General Dimensions	25.4 x 29.6 x 13 cm	51.0 x 30.1 x 13 cm	37.8 x 34.4 x 13 cm	39.1 x 20.3 x 33.8 cm
Heat Transfer Capacity @ 9.5 lpm (Based on fluid inlet temperature relative to ambient)	100 W/K	170 W/K	250 W/K	10 W/K
Liquid Chilling Provided	0 W	0 W	0 W	290 W
Power Consumption	48 W	96 W	276 W	507 W
Cost @ 500 pieces	\$643	\$861	\$938	\$2,586
Picture				
Datasheet	[60]	[60]	[60]	[61]

Next, we generate three different cooling cases with three different combinations of heat exchangers and liquid chiller. The first is the “minimum cooling” case where only the small, 100 W/K heat exchanger is used, the second is the “medium cooling” case where only the medium, 170 W/K heat exchanger is used, and the last is the “maximum cooling” case which combines the large, 250 W/K heat exchanger with the liquid chiller in series.

The step response of the cell temperature to various discharge rates under the minimum, medium, and maximum cooling cases are shown in Figure 78, Figure 79, and Figure 80 respectively. Solid lines are average cell temperature above ambient and dotted lines are the difference between cell minimum and maximum temperatures. The starting battery temperature and ambient temperature was 25°C for each simulation and the SOC range was 100%-20%. The results show that the maximum temperature decreases with the increase in cooling capacity and liquid chilling, with all cases having a max temperature below 5°C, 10°C and, 20°C for 25, 50, and 100 kW respectively and a cell temperature gradient below 5°C for each case. Compared to passive cooling, not only is the maximum temperature reduced, but the cool down rate is also greatly increased.

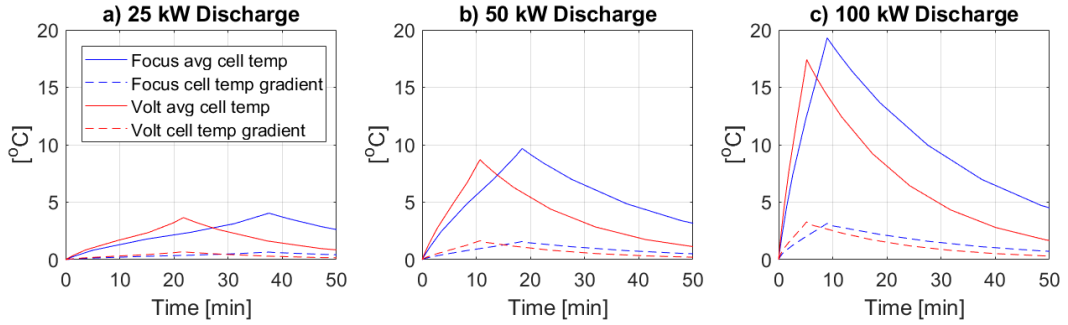


Figure 78 – Step response of battery pack paired with 100 W/K heat exchanger

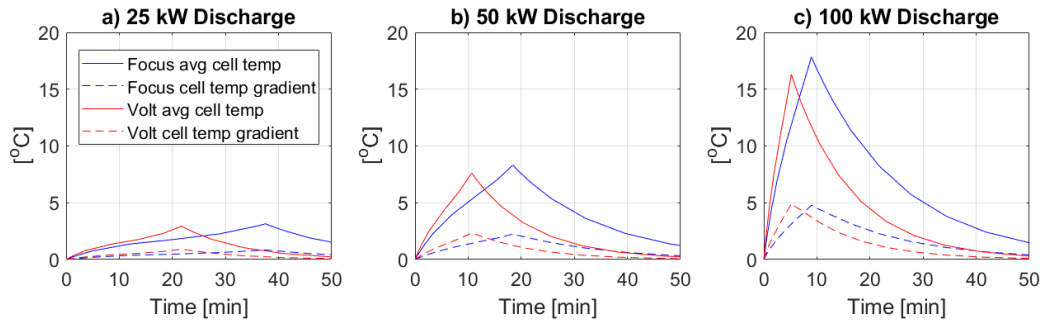


Figure 79 – Step response of battery pack paired with 170 W/K heat exchanger

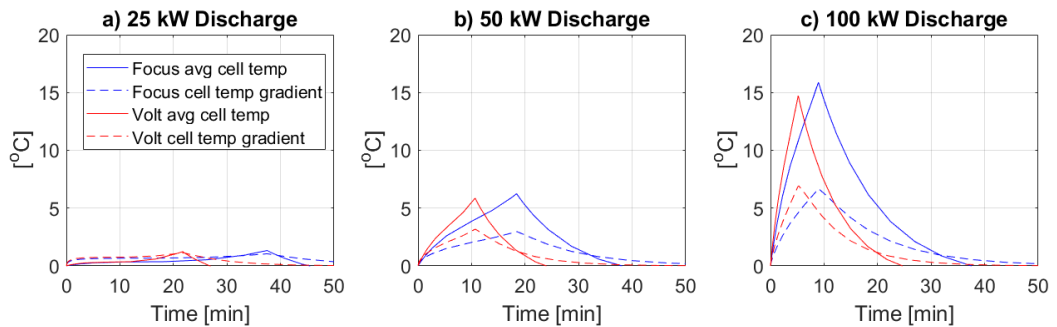


Figure 80 – Step response of battery pack paired with 250 W/K heat exchanger and 290 W of liquid chilling

For all cooling cases the maximum cell temperature gradient was typically below 5°C. This is likely low enough to be acceptable especially for the 25 and 50 kW discharges. Note however that this is likely an under prediction of temperature gradient as non-uniform heat generation was not considered. An example of the internal cell temperature difference in the Volt battery after 50 kW discharge under the medium cooling case is shown in Figure 81. The fluid temperature is shown as well as the cell temperature across three different surfaces of varying depth in the cell, including the front surface in contact with the fluid channel, the back insulated surface, and a cross section in between them (cell center). As expected, the cell is coolest at the fluid entrance and warmest at the fluid exit as the fluid heats up across the surface of the cell. Additionally, the cell temperature increases though the depth of the cell due to the low thermal conductivity in this direction.

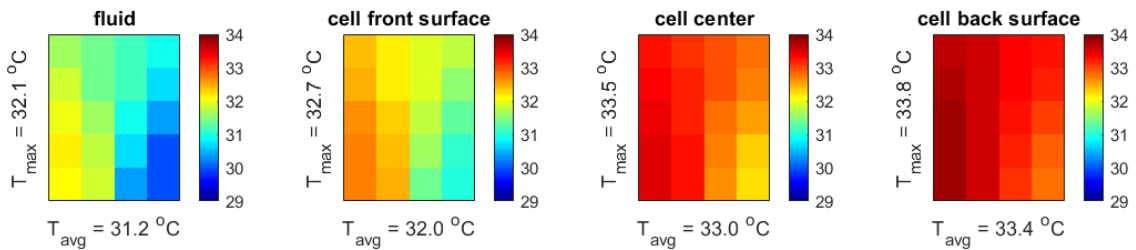


Figure 81 – Temperature for cross sections of Volt cell after 50 kW discharge for “medium cooling” case. Fluid enters at bottom left, exits at bottom right.

4.3.2 Cool Down Rate

To estimate the cooldown rate for the liquid cooling scenario, we calculated the amount of time taken for the batteries to cool down 63% of the way to ambient temperature

to approximate the cooling time constant. Table 21, shows the calculated cooling time constants for each cooling scenario. Note that the time constants are on the order of minutes rather than hours like in the passive cooling case, suggesting the batteries cool much more rapidly. The Volt battery cools more quickly than the Focus battery because it has less thermal mass relative to the size of the heat exchanger. It should be noted that the time constant calculation for the maximum cooling condition does not yield a true “time constant” as the cell temperature does not follow an exponential decay like the other cases due to the liquid chilling; however, it is a useful approximation of the cool down rate.

Table 21 – Time constant for cooldown of battery cells with liquid cooling after 50 kW discharge

	Focus	Volt
Time constant [min^{-1}] with 100 W/K heat exchanger	28	19
Time constant [min^{-1}] with 170 W/K heat exchanger	17	11
Time constant [min^{-1}] with 250 W/K heat exchanger + 300 W liquid chilling	8.5 *	5.7*

4.3.3 *Parameters Sweep of Cooling Capacity*

To determine the effect that heat exchanger capacity and liquid chilling power has on the temperature of the cells we conducted a parameter sweep as shown in Figure 82. All values are for a flow rate of 9.5 liters per minute, with maximum heat exchange rate possible being around 650 W/K, which is equivalent to the heat exchanger cooling the

liquid to ambient temperature. The liquid chilling rate is in terms of heat removed from the liquid. The results show that the addition of heat exchanger capacity has a diminishing effect because as the cell temperature and the fluid exit temperature decrease, a greater heat exchanger size is needed to remove the same amount of heat. The liquid chilling has a more linear effect on the maximum battery cell temperature but provides little increase in performance relative to the high amount of power consumption and cost of such systems.

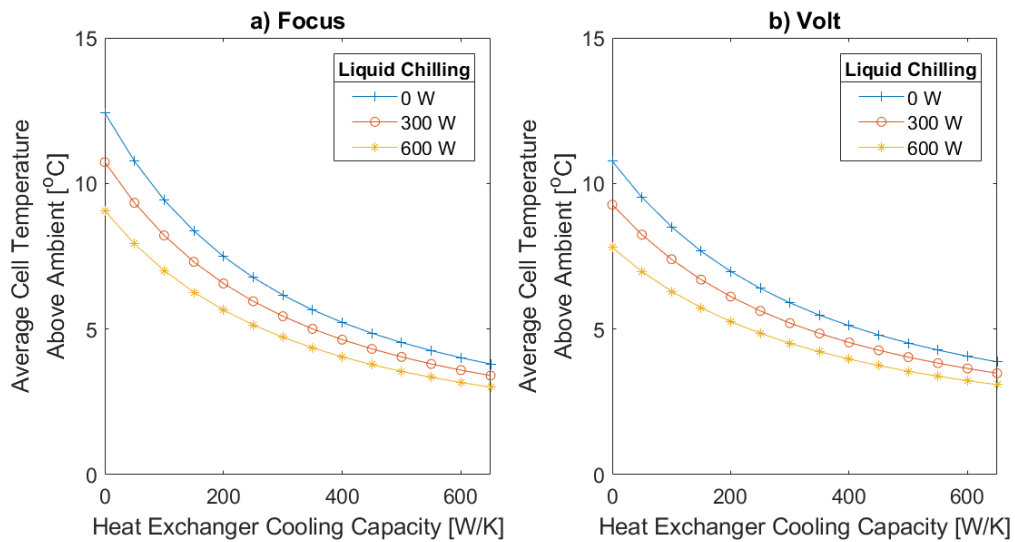


Figure 82 – Effect of heat exchanger cooling capacity and liquid chilling rate to the average cell temperature at end of 50 kW discharge

4.3.4 Uncertainty and Sensitivity Analysis

To incorporate uncertainty into our estimates of cell temperature and cooling time we conduct a Monte Carlo simulation with 1000 runs for battery packs providing 50 kW discharge under the medium cooling scenario using the uncertainty distributions described

in Section 3.7.7. Figure 83 shows the resulting distributions for max cell temperature, cool down rate, and cell temperature gradient. The results show that we can be reasonably certain that the battery maximum temperature will be below 10°C above ambient, which suggest the battery will be kept within safe battery temperatures for nearly all conditions. Also, the cool down time constant will likely be less than 20 minutes for both battery packs, with the Volt cooling faster due to its lower thermal mass. Finally, the maximum cell temperature gradient is likely under 4°C which Chen et al. (2016) suggest as a target maximum for cell temperature difference and thus we assume is acceptable [62].

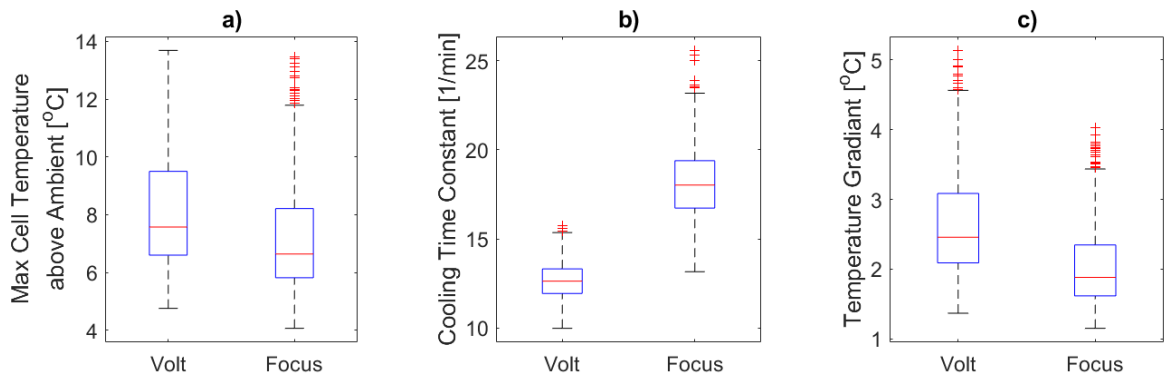


Figure 83 – Distribution of maximum cell temperature (a), cooling time constant (b), and cell temperature gradient (c) for all monte-carlo runs for step discharge at 50 kW with liquid cooling

Figure 84 shows the sensitivity of the thermal performance of the liquid cooled cells under 50 kW discharge to the uncertainties. Like in the passive cooling case the uncertainties with the greatest effect on maximum temperature are the uncertainties in battery capacity and resistance. Again, further reducing uncertainties in these parameters

will yield the greatest increase in certainty for thermal performance. Also note that although uncertainty about cell thermal conductivity is large it has limited effect on the maximum average cell temperature. The cool down rate is mostly sensitive to the parameters effecting thermal mass and less so to the convection coefficient. This is because the convection coefficient is typically not the limiting mechanism for heat loss from the system but rather the heat exchanger cooling capacity. Finally, the cell temperature gradient is affected by uncertainty in cell thermal conductivity but more so by uncertainty in resistance. This is because higher temperatures overall, lead to higher temperature gradients.

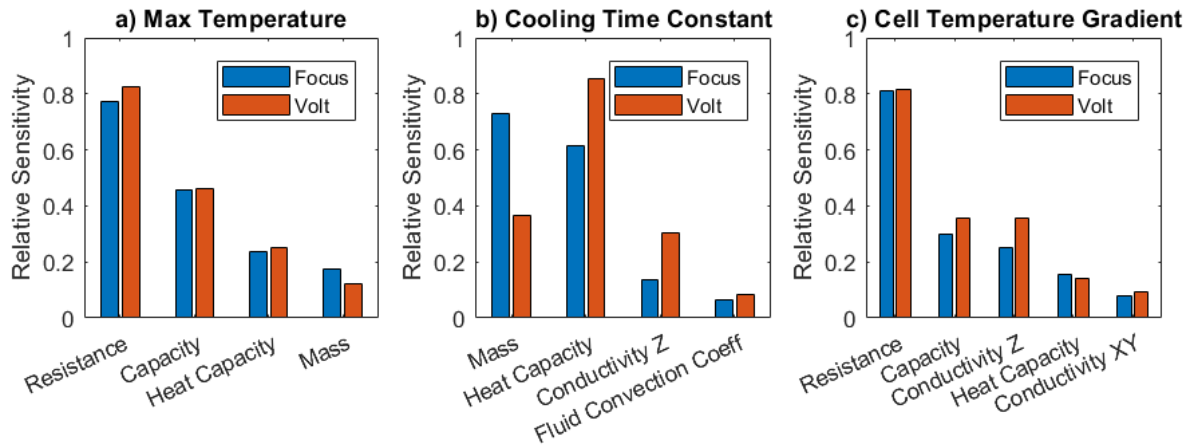


Figure 84 – Sensitivity of max temperature (a), cooling time constant (b), and cell temperature gradient (c) to uncertainty in parameters for liquid cooled batteries under 50 kW discharge and “medium cooling” case

4.3.5 Discussion

The step response analyses show that the addition of active liquid cooling significantly reduces the maximum cell temperature low enough to make 50 kW discharge feasibly safe even for high ambient temperatures and possibly allow for even higher rates. Also, the cool down rate is greatly decreased relative to passive cooling, reducing the cooling time constant from hours to minutes. This is desirable as reducing the amount of time spent at elevated temperatures will increase battery life.

The parameter sweep showed that liquid chilling provided relatively little drop in maximum cell temperature given such a systems power consumption and cost. Thus, we assume that the addition of a chiller to reduce temperature rise is likely unwarranted, but such a device could be used in other ways such as reducing the battery temperature below ambient when the ambient temperature is too high, or by pre-cooling the battery prior to rapid discharges. This would increase battery lifetime and maximum safe discharge power.

Finally, similar to the passive cooling case, the high uncertainties in battery health parameters like remaining capacity and resistance growth have the greatest effect on the uncertainty in performance. Thus, it is desirable to increasing certainty in these parameters for future analyses.

4.4 Thermal Performance with Active Air Cooling

For the final set of thermal analyses, we examine the performance of the active air-cooled design for various discharge rates. This design is assumed to be constructed only with the Nissan Leaf cells, thus the Volt and Focus batteries are left out of this analysis.

4.4.1 Step Response to Various Discharge Powers

Similar to the liquid cooling analysis, we create three different cases for different rates of air cooling. The “minimum”, “medium”, and “maximum” cooling case include air flow rates of 500, 1500, and 3000 cubic meters per hour respectively to the battery pack. Figure 85 to Figure 87 , shows the air-cooled packs response to various discharge rates and air flow rates for each of these cases. Again, the SOC range was 100%-20% and the initial and ambient temperatures were 25°C. The results show that active air cooling can reduce the maximum cell temperature significantly and increase the cool down rate. Additionally, the cell temperature gradient is below 5°C for all case, which is considered acceptable.

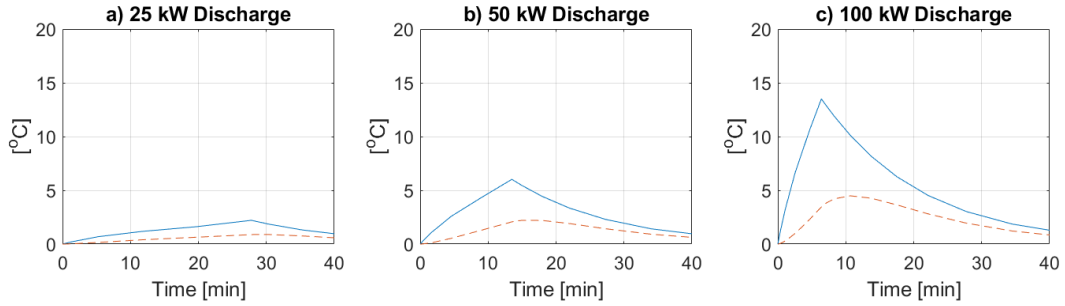


Figure 85 – Figure Step response of air cooled battery with 500 m³/h of air flow heat exchanger to 25 kW (a), 50 kw (b), and 100 kW (c) discharge.

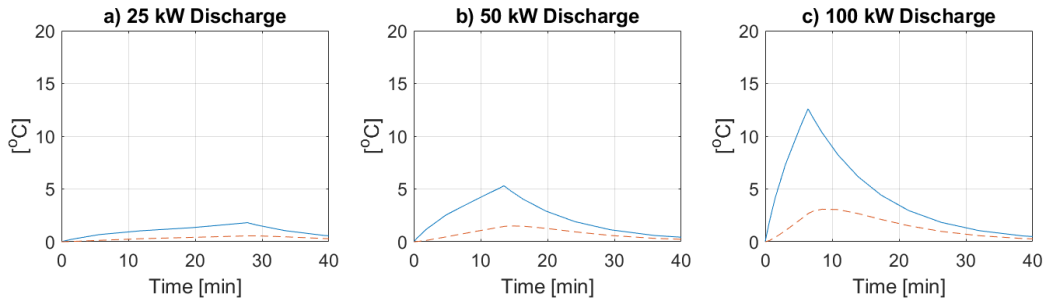


Figure 86 – Figure Step response of air cooled battery with 1500 m³/h of air flow heat exchanger to 25 kW (a), 50 kw (b), and 100 kW (c) discharge.

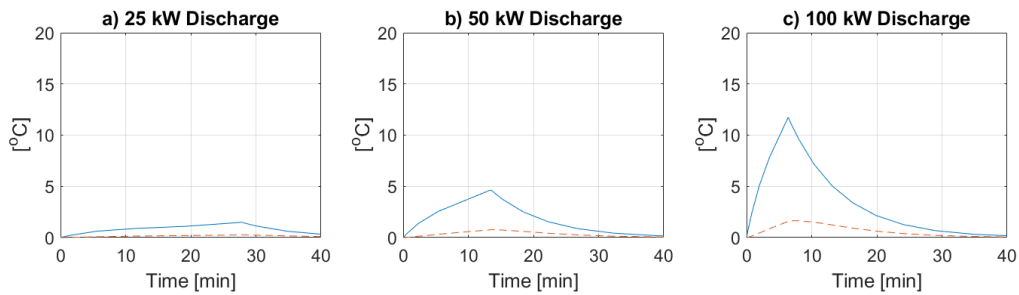


Figure 87 – Figure Step response of air cooled battery with 3000 m³/h of air flow heat exchanger to 25 kW (a), 50 kw (b), and 100 kW (c) discharge.

Figure 88, shows the temperature distribution in the fluid and at different cross sections of the cell after 50 kW discharge of the Leaf battery with 1500 m³/hr of air flow. As the air passes over the surface of the cell, it heats up and thus creates a temperature distribution along the surface of the cell. Additionally, there is a slight temperature gradient through the depth of the cell due to the low thermal conductivity in this direction. Regardless, the total temperature difference within the cell is relatively small.

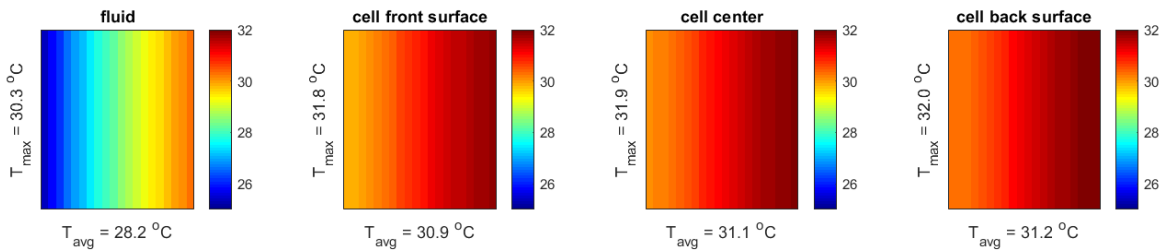


Figure 88 – Temperature for cross sections of Leaf cell after 50 kW discharge with 1500 m³/hr of air flow.

4.4.2 Cool Down Rate

Like in the liquid cooling case, we estimate the cooling time constant by measuring the amount of time taken to return to within 63% of the ambient temperature. For each case the time constant was on the order of 10 minutes which is slightly faster than the liquid cooled batteries, and significantly faster than the passive cooling case.

Table 22 – Time constant for cooldown of battery cells with air cooling

	Leaf
Time constant [min^{-1}] with 500 m^3/hr of air flow	14.4
Time constant [min^{-1}] with 1000 m^3/hr of air flow	10.4
Time constant [min^{-1}] with 1500 m^3/hr of air flow	8.1

4.4.3 *Parameter Sweep*

We conduct a parameter sweep of both the total air flow to the system and the size of the air gap to observe their effect on the temperature of the cells. Figure 89, shows the results for average cell temperature and cell temperature gradient after 50 kW discharge. Increasing the gap size increases the maximum cell temperature due to the decrease in convection coefficient, but also decreases the cell temperature gradient. Meanwhile, increasing the flow speed also decreases the cell temperature gradient but has minimal effect on average cell temperature. Because the flow in the channel is assumed laminar, the Nusselt number correlation is not dependant on flow speed, and thus the convection coefficient is constant with flow rate.

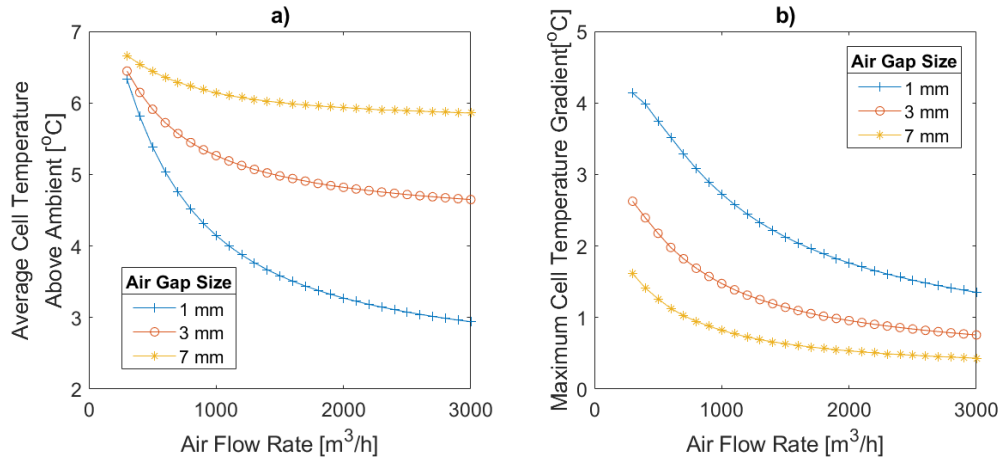


Figure 89 – Parameter sweep of air cooling gap size and air flow rate for air cooled battery after 50 kW discharge.

4.4.4 Uncertainty and Sensitivity

Figure 90 shows the results of a Monte Carlo simulation with 1000 runs of a Leaf battery after 50 kW discharge and 1500 m³/hr air flow including uncertainty in the input parameters. Most runs show a max temperature below 7°C, a cooling time constant less than 12 minutes, and a cell temperature gradient below 2°C. However, some runs show that these values could be as high as 10°C, 13 minutes, and 3°C respectively.

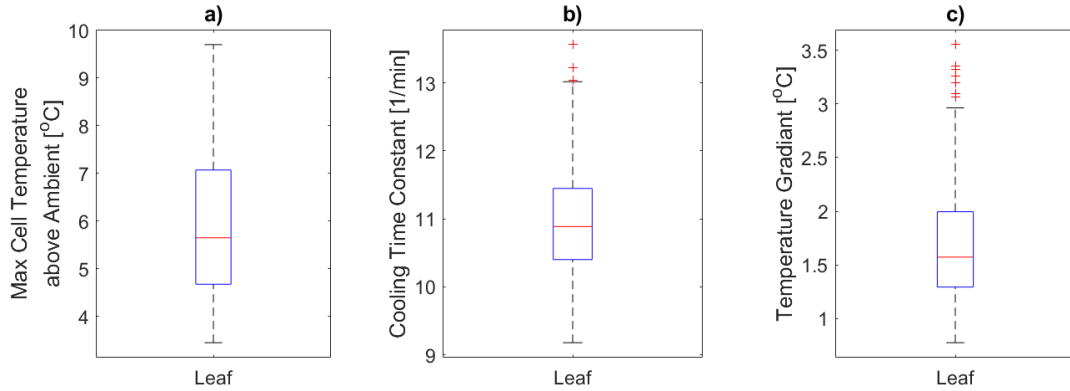


Figure 90 – Distribution of maximum cell temperature (a), cooling time constant (b), and cell temperature gradient (c) for all Monte Carlo runs for step discharge at 50 kW with active air cooling

4.4.5 Discussion

In general, the results show that the addition of active air cooling is similar to the addition of active liquid cooling, in that it significantly decreases the maximum cell temperature for rapid discharge and increase the rate at which the battery returns to ambient temperature. In fact, the active air cooling cases studied seemed to have better cooling performance than the active liquid cooling cases. This is likely because we assume air cooling occurs at both the front and back faces of the cell, whereas liquid cooling is only from the front face. Thus, the large amount of surface area at which air convection occurs makes up for the small convection coefficient relative to liquid cooling. Also, we are assuming that air is brought in at ambient temperature, whereas the heat exchanger in the liquid cooling case is not able to reduce the liquid temperature back to ambient in most cases.

Recall, however, that the Nissan Leaf battery is not designed for active air cooling and exposing the front and back surface areas of the cell to convection would require a great amount of effort. Comparatively, liquid cooling lines are already present in the Volt and Focus batteries making implementation less costly. Additionally, liquid cooling allows the battery to remain sealed which has advantages for safety.

4.5 Fluid Analysis and Thermal Management Power Consumption

In this section we will estimate the amount of power required to run the different thermal management systems.

4.5.1 *Liquid Cooling*

We start with the power consumption of the active liquid cooling system. Figure 91 shows the pressure drop for a given flow rate to the liquid cooled battery packs, with its correlated ideal and real pump power consumption. The coolant chosen was a 50/50 Ethylene Glycol mixture and the pump efficiency was assumed to be 75%. From figure a, the pressure drop increases mostly linearly with flow rate. This is because the flow is laminar and major losses dominate over minor losses. The power consumption thus increases quadratically with flow rate as it is the product of pressure and flow rate. Although the pressure drop is rather high (~1 kpa) the power consumption is low due to the relatively low flow rate of fluid.

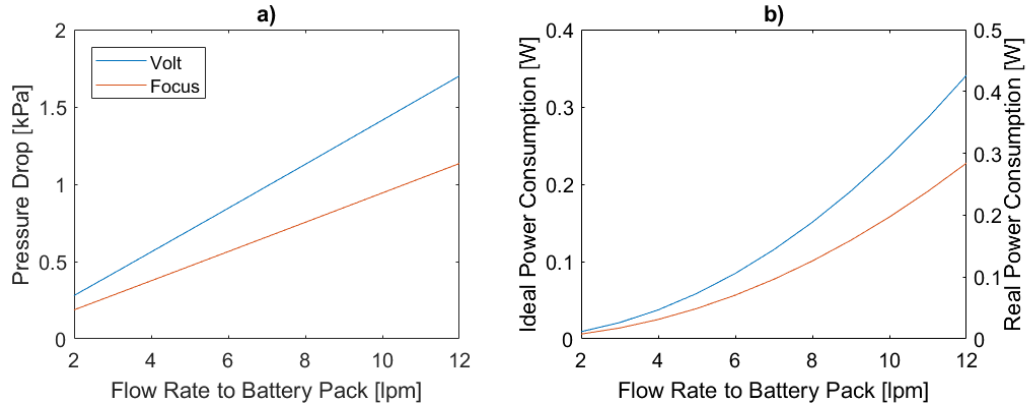


Figure 91 – Pressure drop and power consumption for coolant flow across liquid cooled battery pack

Next, we estimate the pressure drop across the whole coolant loop by including pressure losses for the heat exchanger and connections from the packs to the heat exchanger. The heat exchanger pressure drop was taken from the data referenced in Table 20 and the pipe connections pressure drop was calculated with the pressure drop equation, assuming a diameter of 12.7 mm, 1 m in total length, and six 90° bends. Figure 92 shows the pressure drop and corresponding power consumption for each of these components. We can see that the heat exchanger and pipe connection dominate the pressure losses across the system. This is due to the flow cross-sectional area being relatively smaller in these components, with the cross section being around 130 mm² for the heat exchanger and pipe, compared to around 2600 mm² when adding all the cross sections of each cooling channel in parallel.

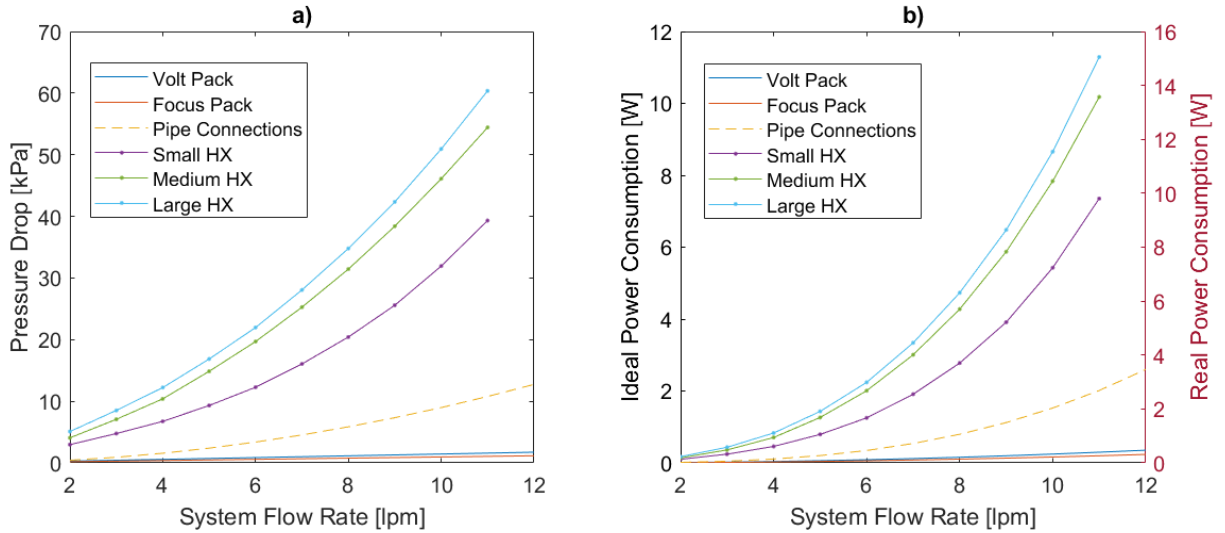


Figure 92 – Pressure drop and power consumption for different components in liquid cooling loop

Finally, we add in the power consumption of the heat exchanger fans and chiller (data found in Table 20). Figure 93 shows the power consumption of the minimum, medium, and maximum cooling configuration as defined in Section 0. For each configuration, the power consumption of the pump (on the order of 10 watts) is minimal compared to the power consumed by the heat exchanger fans (on the order of 100 watts). Also, the addition of a chiller drastically increased the total power consumption of the cooling system.

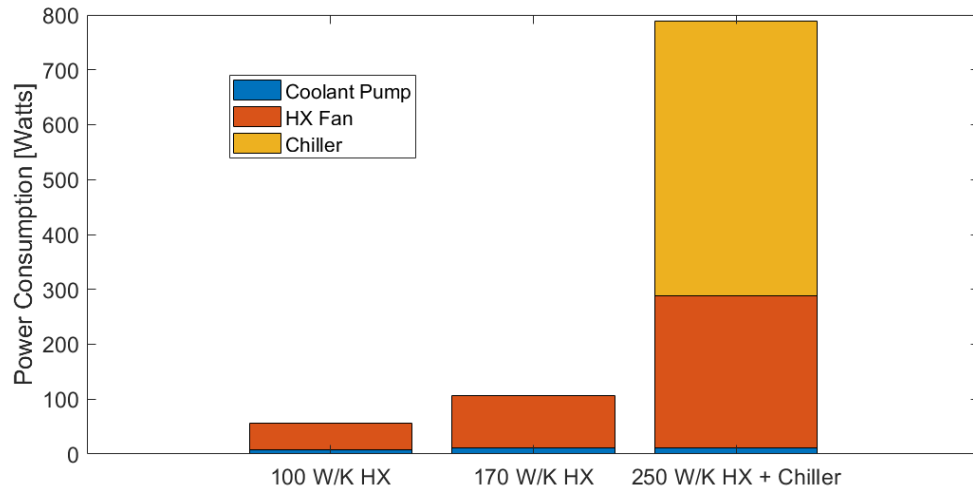


Figure 93 – Power consumption of different liquid cooling system configurations separated by pump, fan, and chiller

4.5.2 Air Cooling

Next, we estimate the pressure drop and power consumption for the active air cooling system with the Nissan Leaf cells, as shown in Figure 94. We used properties for dry air and a fan efficiency of 25%. From Figure 94a, we can see that the pressure drop is slightly non-linear with respect to air flow which is due to the greater relative effect of minor losses. Compared to the pumping of liquid it takes considerably more power to pump air through the battery pack, which matches estimates from Chen et al. (2016) [62].

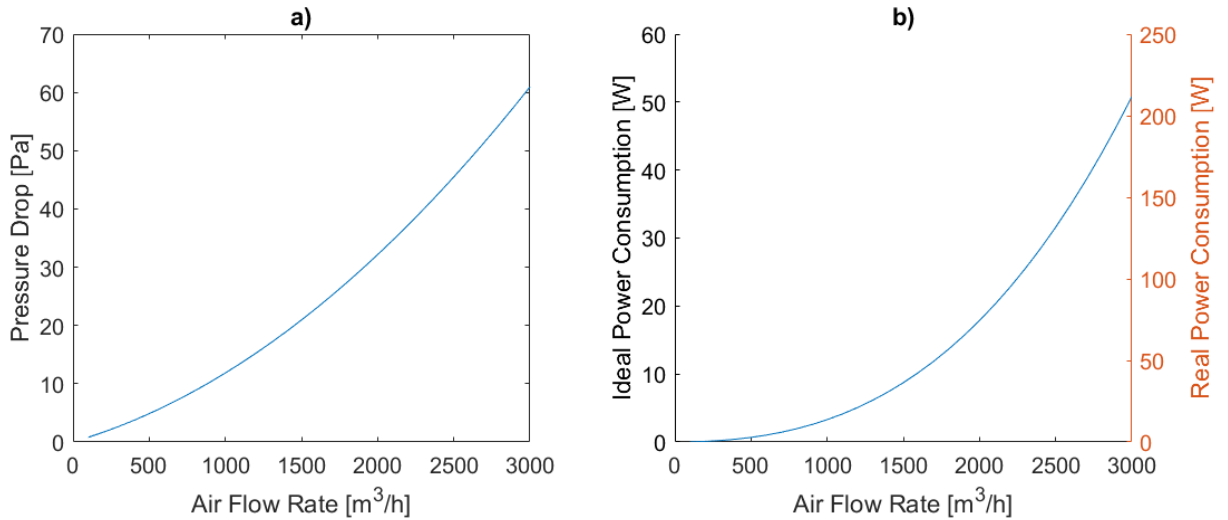


Figure 94 – Pressure drop and power consumption for coolant flow across air cooled Leaf battery pack

Next, we look to add other components in the air flow system. For our generalized design we assume this includes an air filter to prevent contaminants from reaching the cells. We found that pressure drops for pleated filters at these flow rates vary between 50 and 135 Pa, with a typical value of 70 Pa. Figure 95 shows the total power consumption for our system with three different flow rates separated by power to pump air through the air filter and the battery. Like in the active liquid cooling case, the power consumed by the system is dominated by the components other than the battery pack itself. Also, it should be noted that this estimate is likely low for any real system as it neglects pressure drops from other components such as minor losses from flow entrances/exits, bends, and branches.

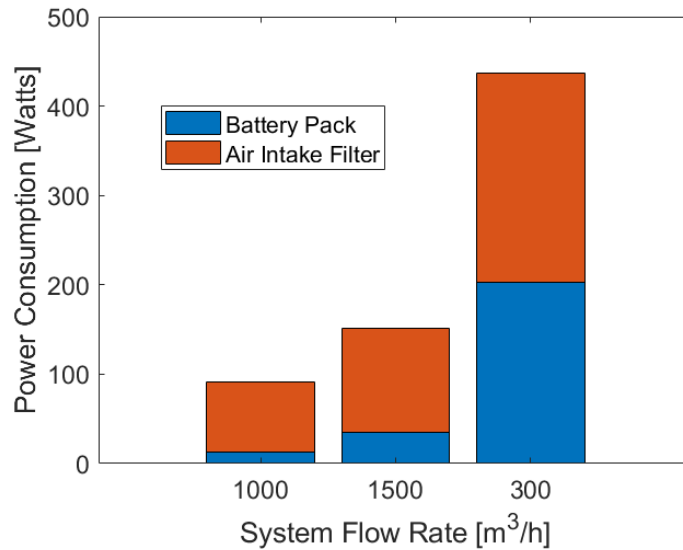


Figure 95 – Power consumption of different active air cooling flow rates by power to drive fluid through battery pack and air filter.

4.5.3 Discussion

When considering a liquid cooled battery design, the power required to pump the cooling fluid through the liquid cooling circuit is relatively small compared to the power required by the heat exchanger fans or a liquid chiller. Thus, the sizing of these components is critical to the power consumption of the device. For instance, adding a liquid chiller can significantly increase the power consumption but was shown in the thermal analysis to have a minimal effect on the temperature rise for fast discharge. It seems unjustified to add a liquid chiller for this use case, but further analysis should be done to see if chilling is useful for other reasons, as mentioned previously.

Similar to the liquid cooled system, pressure losses for the active air-cooled system are likely to be dominated by components other than the battery pack, such as air filters.

Regardless, both systems tend to have total power consumptions of a couple hundred watts. If these systems are only run when DC fast charging a vehicle, lasting on the order of one hour per day, then the total energy consumed in one year will be on the order of 30-40 kWh. If we assume a typical energy price of 10-15 ¢/kWh, then total yearly cost of operation should be around 3 to 6 dollars which is negligible.

4.6 Comparison of Thermal Management Methods

Pooling the results from the previous sections we can make some general comparisons between the different thermal management methods. Figure 96 shows a direct comparison of battery temperature for 50 kW discharge under adiabatic, passive cooling, and active cooling scenarios. The SOC range chosen was 100%-20% and the initial battery and ambient temperature was 25°C. The active cooling for each battery is taken at the “medium cooling case” which includes a 170 W/K heat exchanger for the liquid cooled Volt and Focus and 1500 m³/hr of air flow for the air-cooled Leaf battery. Comparing the adiabatic case with the passive case, shows that the addition of natural convection does not reduce the maximum temperature by much, whereas active cooling significantly decreases the maximum temperature and the rate at which the battery cools down. Additionally, the active air cooling seems to outperform the liquid cooling. This is since the cell surface area exposed to convection is rather large thanks to its flat shape, and air flow is provided to both sides of the cell rather than one side like in the liquid cooling case. However, as mentioned before, exposing these surface areas to convection would require a significant amount of redesign to the Nissan Leaf module, whereas liquid cooling of the Volt and Focus packs is already present in the design. Also, liquid cooling allows for the battery pack to be completely sealed which will have advantages for safety and robustness. These reasons combined make liquid cooling more practical.

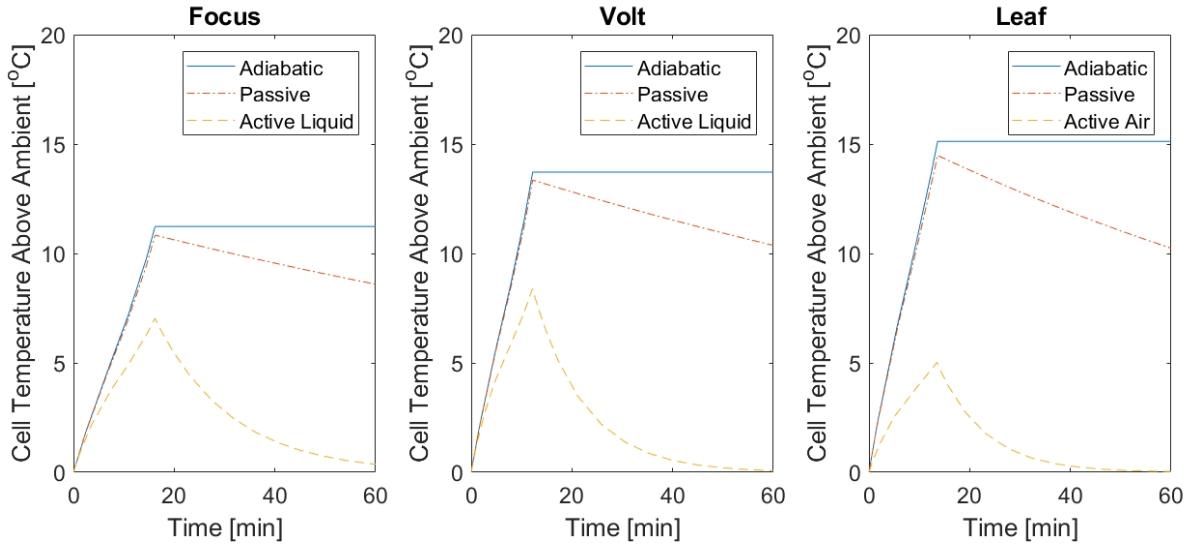


Figure 96 – Comparison of thermal management methods for 50 kW discharge

Figure 97 compares the power consumption for the passive, active liquid, and active air cooling thermal management systems under the “medium cooling” scenario. We assume that the passive cooling will consume around 10 watts for small fans to exchange air with the environment as mentioned in Section 4.2. In general, the two active cooling cases consume around the same amount of power, on the order of 100 watts. Although air cooling consumes more power in this case, it does provide better performance as shown in Figure 96, and thus is not a one-to-one comparison.

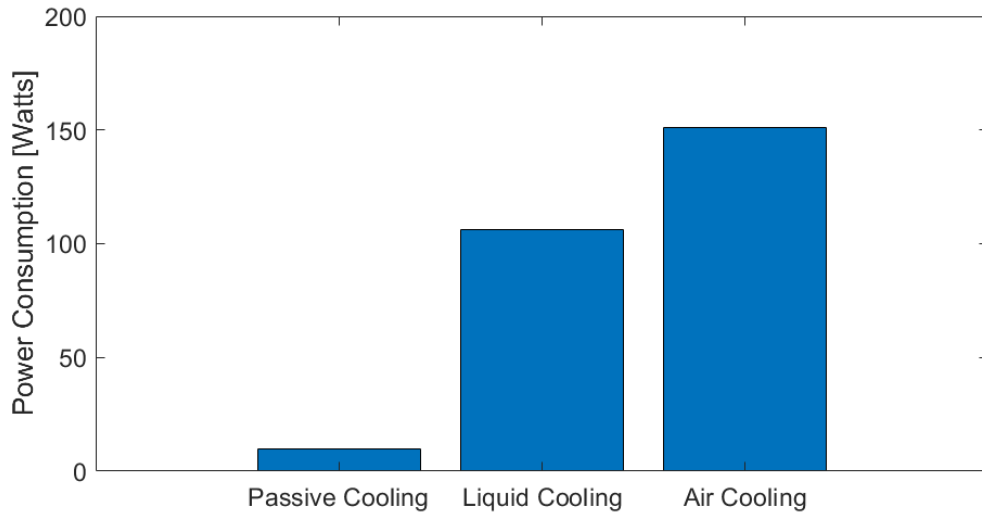


Figure 97 – Comparison of thermal management method power consumption under “medium cooling” case

4.7 Simple Life Estimates

To estimate the amount of degradation of battery capacity in second life we adopt the battery aging model from literature as described in Section 3.6 and calculate the capacity loss for 10 years under the following four simplified use cases:

1. **No Cycling:** calendar ageing of the battery if it was simply left in storage without cycling.
2. **No DCFC:** the battery provides load shifting and solar storage but does not provide DC fast charging of a vehicle and includes a passive thermal management system.
3. **Passive Cooling:** the battery provides load shifting, solar storage, and DC fast charging with only a passive thermal management system.
4. **Active Cooling:** the battery provides load shifting, solar storage, and DC fast charging with an active thermal management system. This includes active liquid cooling for the Focus and Volt batteries, and active air cooling for the Leaf battery.

For simplicity, the number of cycles per day and the ambient temperature for each scenario is kept constant. The conditions of the ageing scenarios are summarized in Table 23. Each condition can contain two types of cycles: a house load shifting cycle, where the current draw is assumed low enough not to effect temperature, and a DCFC cycle where the temperature rises predicted by the thermal model are added as stress factors using Equation 47. The passive and active cooling conditions contain one house load shifting cycle and one DCFC cycle per day, while the ‘No DCFC’ condition has just two load

shifting cycles. The power draw chosen for the DCFC cycles was 50 kW. For each cycle the battery is assumed to be charged and discharged between 100% and 20%. The ambient temperature is assumed to be 25°C which is similar to the average ambient temperature in Phoenix, AZ [98].

Table 23 – Summary of ageing scenario conditions

	Number of house load shifting cycles	Number of DCFC cycles	SOC range	Ambient temperature
No Cycling	0	0	60%	25°C
No DCFC	2	0	100-20%	25°C
Passive Cooling	1	1	100-20%	25°C
Active Cooling	1	1	100-20%	25°C

Figure 98 shows the capacity fade predicted by the model for each scenario and for each vehicle battery. We can see that even in the “No Cycling” case there is significant degradation in the battery even compared to the other cases with cycling. This enforces the findings from studies such as Neubauer et al. (2015) who determined calendar aging to be the dominant over cycling aging for electric vehicle batteries [4]. The “No DCFC” scenario sees slightly greater degradation due to the influence of cycling. Including DC fast charging as seen in the passive cooling case increases the degradation, even though the total number of cycles is the same. This is due to the increased temperatures seen by the battery during the DCFC cycles. However, when including active cooling methods, the degradation is decreased to near the same level as the “No DCFC” case, because the thermal management

system can reduce the batteries maximum temperature and increase the rate of cool down significantly. Despite this, the change in remaining capacity after 10 years gained by including active battery cooling is only around 2-3%.

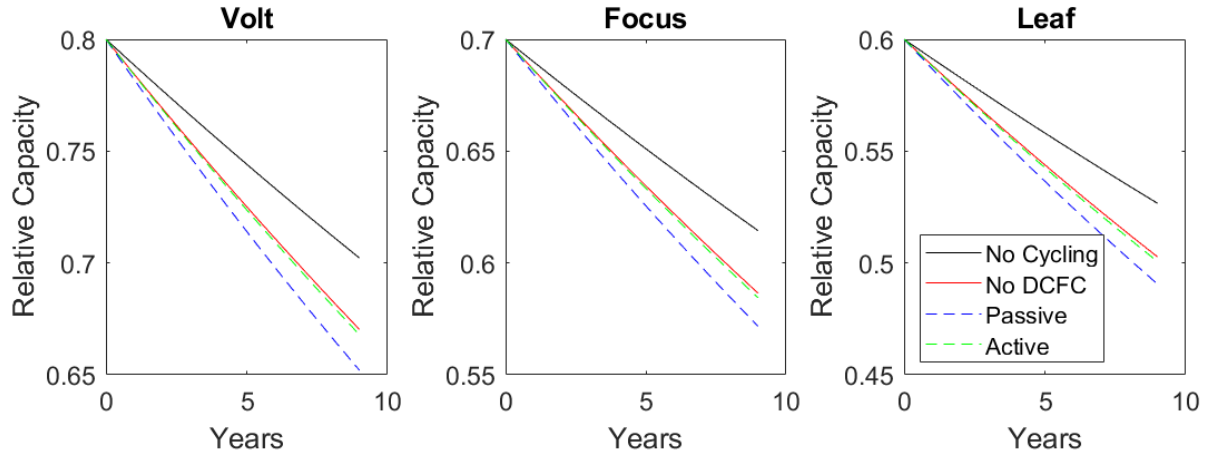


Figure 98 – Capacity degradation estimates in second-life under different scenarios

Overall, the model predicts a relatively gentle decline in battery capacity in second life, even when rapidly discharging with passive cooling. It is important to consider, however, that the methods adopted only models the decelerating fade portion of the batteries life. Experimental studies such, such as those by Martinez-Laserna et al. [38], have shown that the region of accelerating fade can be extremely important to the lifetime of aged batteries. Thus, there is a high degree of uncertainty to the degradation of these batteries in second life, and if a region of accelerated fade is reached, degradation would be much higher than is predicted by the model we used. Thus, in future work, it will be

important to study this phenomenon in greater detail for a more accurate prediction of system lifetime.

Regardless of the possible inaccuracies of the model, the results of this analysis still show that the addition of active cooling does reduce the amount of ageing seen by rapid discharging and may even make it comparable to the same system without rapid discharging. Also, even if accelerated decline becomes a factor, temperature will still play a role in this mechanism, which active thermal management is likely to mitigate.

4.8 Case Study Simulation of Realistic Use in Homes

This section covers the results of the simulations of realistic usage of our concept energy storage device in homes. This includes its effect on energy consumption, energy expenditures, and vehicle charging.

4.8.1 *Home Energy Use without Storage Device*

Before running the case study simulations, it is helpful to quantify the energy usage in the homes prior to the addition of energy storage. Table 24 summarizes both the total energy consumption, production, and grid use for each of the three houses. Note that the total “household” energy consumption includes all loads other than electric vehicle charging and is higher than most homes since we assume that all the homes are fully electric and do not rely on any use of natural gas. The amount of energy spent charging an electric vehicle is also a significant portion of the total energy consumption. We then match the size of the PV array to generate enough electricity to match the total energy demand, meaning the net energy production of the house is zero. Despite this, there is a great temporal disparity between peak solar production in mid-day and the peak consumption in the evening when occupants are more likely to be at home and when vehicles are more likely to be charging. This means the homes still pull a significant amount of the energy it consumes from the grid, ranging from 69-81% of total consumption. This means 69-81% of solar energy produced by the homes is sold back to the grid.

Table 24 – Energy consumption of case study homes before the addition of energy storage

City	Energy Consumed			PV Generation	Energy From Grid	
	Household [kWh]	EV Charging [kWh]	Total [kWh]	[kWh]	[kWh]	Relative to total consumption
Los Angeles	11,285	6,060	17,345	17,345	14092	81%
Phoenix	15,467	6,060	21,527	21,527	14884	69%
Chicago	19,668	6,060	25,728	25,728	18716	73%

Next, we estimate the electricity costs for these homes. We start by assuming that the homes are on the time-of-use plan offered by their utility company, except for Chicago where only a flat-rate plan is offered. All information on rate prices and times was taken from the Department of Energy’s “openEI” utility rate database [99]. The plans chosen for each city include:

- **Los Angeles:** Southern Californian Edison, TOU-D-A Plan
- **Phoenix:** Salt River Project, TOU Plan
- **Chicago:** Commonwealth Edison Co, Residential Single Family with Electric Space Heat Plan

Figure 99 compares the electricity prices for the summer months for all three utility rate plans. The Phoenix and Los Angeles plans have a mid-peak in the morning and middle

of the day followed by a peak in the evening and off-peak late at night. Chicago on the other hand has a flat rate price for all times of day. Also, the price of electricity is significantly higher in Los Angeles than in Phoenix or Chicago; this will have a great effect on overall electricity expenditures.

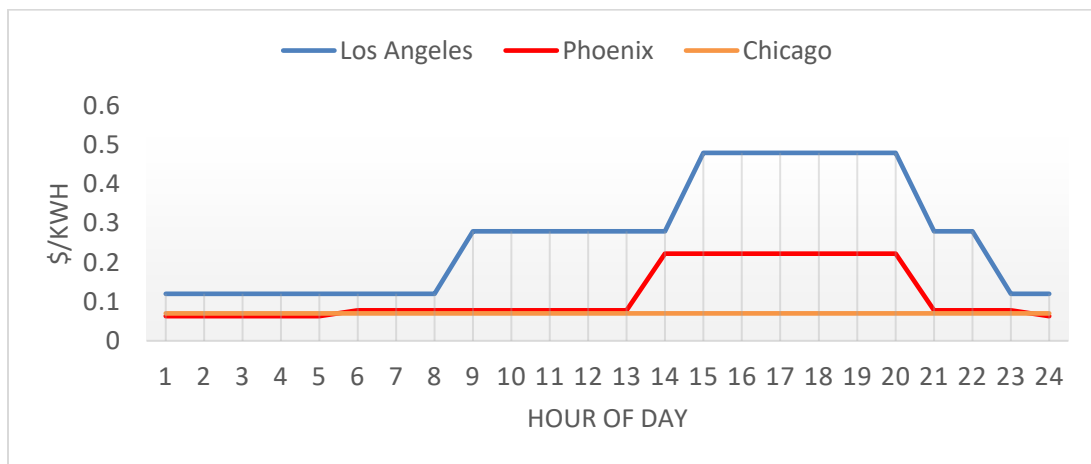


Figure 99 – Comparison of utility rates in selected locations for summer months

Next, we calculate the total electricity expenditures for each home based on three scenarios for the feed-in-rate, choosing 100%, 50%, and 0% for the feed-in-rate meaning the user is compensated at 100%, 50%, and 0% of the current electricity price for solar energy sold back to the grid. 100% is equivalent to a net metering policy, whereas 50% may be more realistic in a future scenario if utility companies remove net metering policies, and 0% is an unlikely worst-case scenario.

Table 25, compares the electricity costs for one year in each home for each of the feed-in-rate scenarios. For the net-metering 100% feed-in-rate the cost for all three homes

is around zero because we set the net energy use to near zero, with slight variations in Los Angeles and Phoenix due to the changing electricity price based on time of day. Decreasing the amount paid for solar energy greatly increases the cost of energy, especially in Los Angeles due to the relatively high cost of electricity. Note we do not model the effect that using the time-of-use plan has on consumption behavior for the residence which may significantly decrease these costs.

Table 25 – Comparison of utility rates chosen for each city for summer period.

City	Energy Cost		
	100% feed-in-rate	50% feed-in-rate	0% feed-in-rate
<i>Los Angeles</i>	-\$216	\$1,781	\$3,777
<i>Phoenix</i>	\$173	\$751	\$1,328
<i>Chicago</i>	\$17	\$671	\$1,326

4.8.2 Home Energy Use with Storage Device

Next, we simulate the use of our energy storage device in each home using each electric vehicle pack. We specify that each system uses the “medium cooling” active thermal management strategy defined previously. This includes a 170 W/K heat exchanger and no chiller for the liquid cooled Volt and Focus batteries and 1500 m³/hr of air flow for the Nissan Leaf battery.

Table 26, shows the resulting change in energy consumption patterns after the addition of the energy storage device. The overall energy consumed by the homes increased by 1-3% due to inefficiencies in the batteries and power consumption of the battery

management systems. This is consistent with results from other studies such as Hittinger et al. (2017) [10]. The homes still pull a majority of the energy they consume from the grid however the batteries were able to reduce the amount of grid reliance by between 11% and 25%. The reduction in grid reliance was higher in Los Angeles and Phoenix compared to Chicago, which we hypothesis is due to low solar generation in Chicago during winter months. Additionally, the Focus and Leaf batteries were able to reduce grid use more than the Volt battery due to their higher energy capacity. It may be possible to increase the reduction in grid reliance by increasing the number of battery packs used per house or changing the SOC range in which the battery operates home storage, but this will include trade-offs with cost which should be studied in future analysis.

Table 26 – Change in energy consumption for one year simulation

City	Vehicle	Increase in Energy Consumption [kWh]		Energy from Grid [kWh]		Change in Grid Reliance
		kWh	Relative to total consumption	kWh	Relative to total consumption	Compared to without battery
Los Angeles	Volt	363	2%	10,621	61%	-20%
	Focus	441	3%	9,753	56%	-25%
	Leaf	477	3%	10,335	60%	-22%
Phoenix	Volt	322	1%	11,609	54%	-15%
	Focus	407	2%	10,674	50%	-20%
	Leaf	410	2%	11,272	52%	-17%
Chicago	Volt	455	2%	15,825	62%	-11%
	Focus	552	2%	15,018	58%	-14%
	Leaf	608	2%	15,585	61%	-12%

Table 27, summarizes the cost savings calculated for one year for each simulation given the three different feed-in-rate scenarios described in Section 4.8.1. For the 100%

feed-in-rate (net-metering) scenario, the addition of the battery had minimal cost savings or actually increased energy costs. This is because the additional energy consumption cost outweighed savings from energy time shifting, especially in Chicago where there is a flat electricity rate. In such locations it may be better to gear the system more toward providing DC fast charging as it may provide greater benefits to the user. Decreasing the feed-in-rate to 50% or 0% increases the total energy savings due to increased self-consumption of solar energy. Savings are particularly higher in Los Angeles due to their relatively high energy prices. Still if we assume that the system will cost around the same as a Tesla Powerwall (~\$10,000), most cases will likely not see a return on investment within 10 years except for the extreme 0% feed in rate in Los Angeles, and this does not consider degradation during second life. The energy saving could be increased, however, by changing the battery control algorithm to prefer cost savings over self-consumption or by utilizing more of the battery capacity for home energy storage rather than vehicle charging. Future analysis of these would be beneficial if any such device is to be constructed.

Table 27 – Energy cost savings for one year simulation

City	Vehicle	Decrease in Energy Cost		
		100% feed-in-rate	50% feed-in-rate	0% feed-in-rate
Los Angeles	<i>Volt</i>	\$88	\$602	\$1,117
	<i>Focus</i>	\$102	\$745	\$1,387
	<i>Leaf</i>	\$69	\$638	\$1,207
Phoenix	<i>Volt</i>	-\$3	\$156	\$315
	<i>Focus</i>	\$10	\$208	\$405
	<i>Leaf</i>	-\$3	\$173	\$348
Chicago	<i>Volt</i>	-\$32	\$93	\$218
	<i>Focus</i>	-\$39	\$118	\$275
	<i>Leaf</i>	-\$43	\$96	\$235

Table 28 summarizes the amount of DC fast charging that was provided to the vehicles over the course of the one-year simulation. The total amount of energy delivered to the vehicle through DC fast charging was around 2000-2500 kWh, which accounts for around a third of the total energy demand for the vehicle (from Table 24). The average energy delivered per charge event was around 6-9 kWh which is roughly equal to 18-27 miles of range which at 50 kW equates to charge times of around 10 minutes. It is expected that such at home fast charging would be particularly desirable to the user, but to determine if this outweighs the cost of the system should be the subject of further study.

Table 28 – DC fast charging energy delivered to vehicle for one year simulation

City	Vehicle	Total Energy Delivered to Vehicle	Average Energy Delivered to Vehicle per Charge Event	
		kWh	kWh	miles range
<i>Los Angeles</i>	<i>Volt</i>	2003	6.4	19
	<i>Focus</i>	2743	8.8	26
	<i>Leaf</i>	2246	7.2	22
<i>Phoenix</i>	<i>Volt</i>	2041	6.6	20
	<i>Focus</i>	2803	9.0	27
	<i>Leaf</i>	2313	7.4	22
<i>Chicago</i>	<i>Volt</i>	1876	6.0	18
	<i>Focus</i>	2539	8.2	24
	<i>Leaf</i>	2083	6.7	20

4.8.3 General Observations

Looking closely at the results of the case study simulations reveals some general observations about how the system behaves. Figure 100 shows the temperature of the battery versus ambient temperature for the Volt battery during the first week of the year in Phoenix. During general operation the battery temperature follows the ambient temperature with some lag and dampening. This is as expected, as the convection rate is low compared to the thermal mass and the heat generation for low power applications is low enough to not significantly affect battery temperature. The spikes in temperature seen are when the battery is providing fast charging to the vehicle, but we can see that the temperature quickly returns to ambient thanks to the active liquid thermal management system.

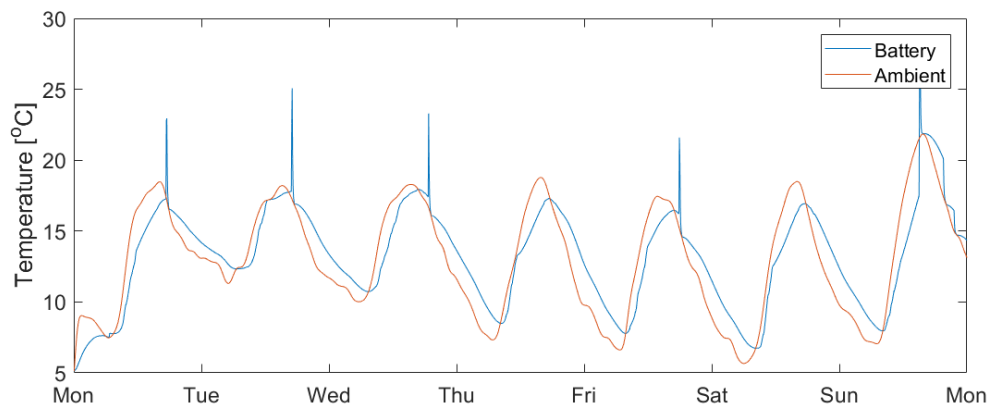


Figure 100 – Example of battery temperature for Volt battery during first week of the year in Phoenix home.

Figure 101 shows the battery SOC for the same Volt battery for the same first week in Phoenix. The black dotted lines show when charging events occur. The battery is typically charged up to 100% by mid-day when solar generation is high, then quickly drained in the evening if a car is charged. After which there is typically no additional solar generation and the battery is not used for the rest of the night until the next day. On Thursday when there was no charge event we see that the battery was left at the reserve SOC point of 50%. This reveals a trade-off inherent in the system, if the device had known that vehicle would not be charged that day, then the remaining battery capacity could have been used to offset house load but doing so would cause the user to forfeit any possible fast charging later in the day. Another problem is on days like Sunday when multiple charge events occur. The first charge event drains the battery, and without solar generation afterward there is no charge left for the next charge events and thus no fast charging occurs. This could be an issue that could be solved by allowing the battery to charge from the grid after fast charging, but this adds complexity to the battery management algorithm and might increase energy costs as this might include charging at peak times. Ultimately the optimal way to manage energy into and out of the battery should be the subject of future study.

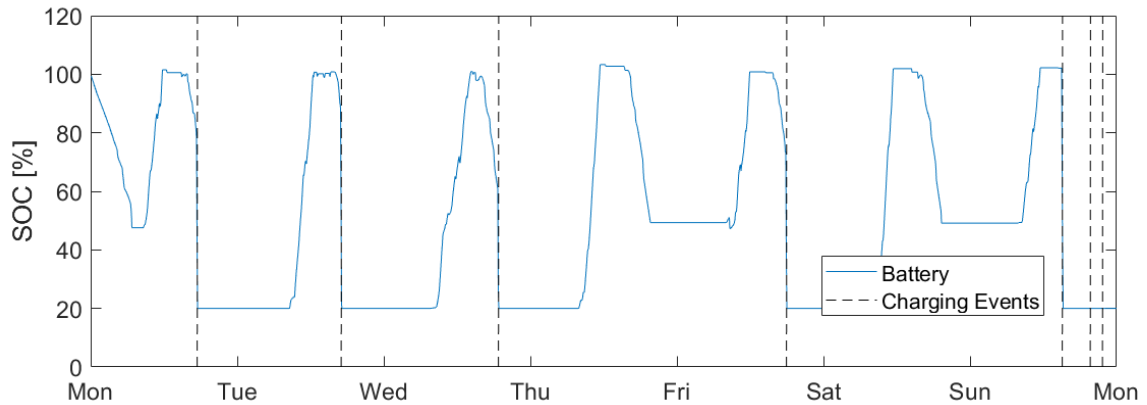


Figure 101 – Example of battery SOC for Volt battery during first week of the year in Phoenix home.

Figure 102, shows the grid power draw both with and without the battery for the same time period of simulating the Volt battery in the Phoenix home. The addition of the battery in general dampens the use of the grid, however not after the battery has reached the minimum or maximum SOC. As mentioned, this is partially due to the trade-off between sending energy to the home or to the car. On most days the car charging drains most of the energy from the battery which leaves little to none for use in the home afterwards. This could be alleviated by changing the battery management algorithm to charge from the grid or by increasing the size of the battery such as using two battery packs. Additional analysis is required however to determine if such solutions are economically feasible.

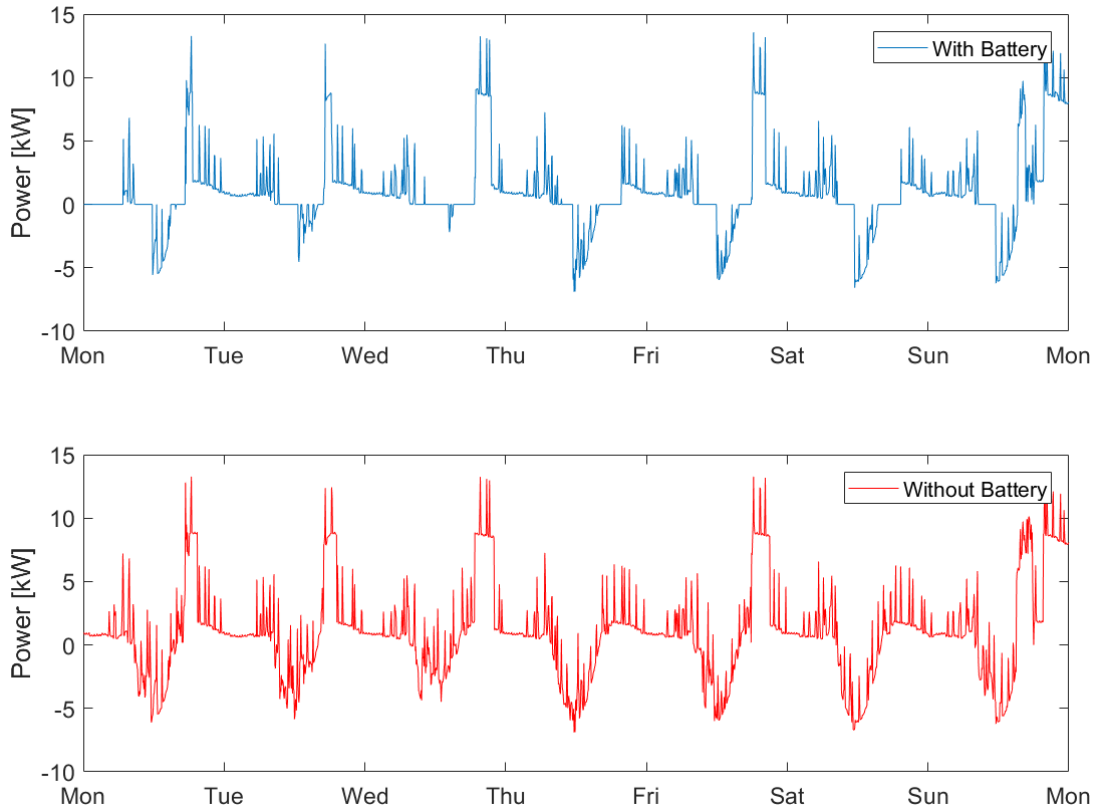


Figure 102 – Example of grid use with and without Volt battery during first week of the year in Phoenix home.

Close observation also reveals that the thermal management system was able to maintain safe battery temperatures throughout the simulation. Figure 103, shows the battery temperature for the Focus battery during one of the hottest weeks in Phoenix. Though the ambient temperature exceeded 40°C the thermal management system was able to keep the battery temperature below 45°C which is still below unsafe levels.

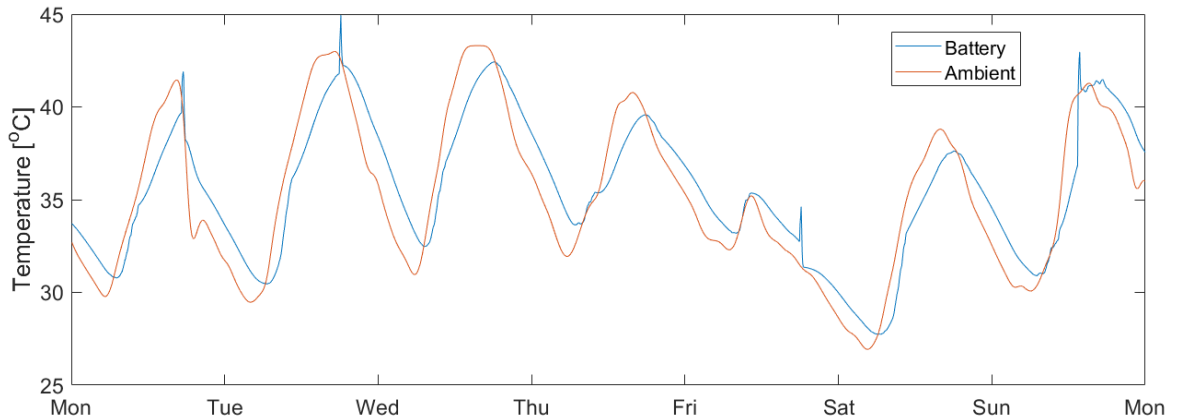


Figure 103 – Example of battery temperature for Focus battery during summer week in Phoenix home.

Similarly, Figure 104 shows the battery temperature of the Volt battery during one of the coldest weeks in Chicago. The heating system maintains the battery temperature above 0°C even as the ambient temperature dips below -20°C. Additionally, the cooling system is not activated when DC fast charging, which allows the battery to maintain the heat generated during this time.

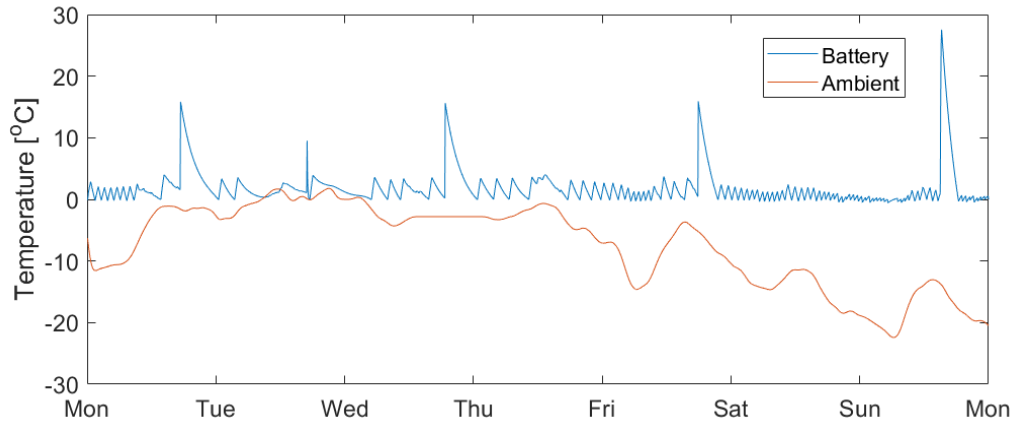


Figure 104 – Example of battery temperature for Volt battery during winter week in Chicago home.

4.8.4 Discussion

In general, the results of the case study simulations prove that the reused electric vehicle batteries can provide home energy storage and vehicle charging while maintaining safe operating temperatures. Results show such systems can reduce the amount of grid use by around 10-25%, but significant reductions in energy costs are only seen for cases without net-metering policies. Without a significant discount to the amount paid to the user for energy returned to the grid, there is little economic incentive to store and use one's own solar energy. Additionally, inefficiencies in the storage system increased the energy consumption by 1-3% which degrades the energy cost savings. This would likely only be greater if the size of the system were increased to include two batteries, for example.

Under the current control scheme chosen, the batteries were able to provide around 1/3rd of the total electric vehicles home charging demand through DC fast charging,

typically providing around 20 miles of range in 10 minutes. However, on days with multiple charging events, the battery is typically depleted after the first event, leaving little to no fast charging for subsequent charges. This could be fixed by changing the battery control algorithm but doing so might increase energy costs.

Looking at the results closely reveals trade-offs in the system between focusing on reducing energy cost, reducing grid use, and providing electric vehicle charging; as focusing in one area typically means sacrificing benefits in another. Ultimately, additional analysis is required to determine the optimal design of such a system and maximize economic feasibility. It would be beneficial for future analysis to focus on the battery management algorithms to determine the optimal energy flow between the battery, home, and vehicle. Doing so would require estimates of the relative value the user assigns to cost savings, reducing in grid reliance, and vehicle fast charging. Additionally, adding capacity degradation and resistance growth estimates to the simulation would increase the accuracy of performance estimates for our systems. Finally, adding simulations for the system providing back-up power would aid in determining total utility.

CHAPTER 5. CONCLUSIONS AND FUTURE WORK

Results from the thermal studies showed that passive thermal management strategies are likely adequate for low power consumption applications like the less than 10 kW typically required for powering a house. Even for low rates of providing DC fast charging to a vehicle, such as discharging at 25 kW, the battery does not reach dangerous temperature levels for most cases, before depleting. This is because the thermal mass of the batteries is high enough to absorb a large amount of the heat generated. Thus, the batteries see minimal temperature rise if the power draw is for a brief period of time, like would be expected for covering brief load spikes in a home or providing DC fast charging to a vehicle. However, the minimal amount of exposed surface area of the battery cells, and the low convection rates from natural convection mean that the batteries take many hours to cool down from any temperature increase under passive cooling. This increases the amount of time spent at elevated temperatures and increases the rate of battery degradation.

The addition of active thermal management decreases the maximum battery temperature due to high power draw, allowing the battery to sustain discharge rates of up to 50 kW or more without reaching dangerous battery temperatures, even when accounting for uncertainty. Equally if not more important, is that active thermal management significantly decreases the amount of time taken to cool the batteries from a temperature rise; from hours under the passive cooling case to minutes with active cooling. Analysis of capacity loss during second life showed that this decreased time spent at elevated

temperature decreased the degradation caused by rapid discharging to the point where it matched a similar system without rapid discharging.

Comparing active air cooling to active liquid cooling showed that active air cooling had slightly better performance, due to the large amount of cell surface area exposed to forced convection, even though the convection coefficients are lower than with liquid cooling. Despite this, none of the battery packs studied were originally designed for active air cooling, whereas implementing active liquid cooling for the Chevy Volt and Ford Focus battery packs requires considerably less remanufacturing of the battery pack. Additionally, liquid cooling allows the batteries to remain sealed which increases safety and robustness. Thus, we assume that active liquid cooling is a more practical solution, and still allows for very high rates of discharge.

Analysis of thermal management power consumption showed that the pumping of liquid coolant consumed very little power due to the relatively low flow rate and the high efficiency of the pump. Thus, most of the power consumed by an active liquid cooling system is from the fans used in the heat exchanger. Additionally, adding a liquid chiller to the cooling circuit nearly doubled the energy consumption of the system without much decrease in maximum temperature or cooling rate for a rapid discharge. This suggests adding a chiller for these reasons is likely unjustified. However, adding a chiller for reasons of lowering the battery temperature below ambient temperature for long periods of time may significantly increase battery lifetime, but additional study is required in this area to weight the costs and benefits. Without a chiller, an active liquid cooling system is expected to consume around 100 watts during operation, which if operated for one hour each day for

vehicle fast charging yields a yearly energy consumption of around 40 kWh, which is relatively small compared to the total energy use of a home (typically >10,000 kWh).

Analysis of power consumption for active air cooling schemes showed a similar amount of power consumption to the liquid cooling layout, with most of the power consumed by forcing flow through system components other than the cells themselves, such as an air filter. The expected power consumption of an air-cooled system is also on the order of 100 watts but varies greatly with flow rate.

Estimates of degradation during second life showed around a 10-15% drop in capacity after 10 years with the inclusion of a thermal management system leading to around 2-3% less capacity loss. However, the model we adopted from literature only models the decelerating fade region of battery life, whereas experimental studies have shown that the accelerating fade region can be extremely important to the lifetime of second use batteries. Thus, further study of this phenomenon is required to increase the accuracy of future estimates. Regardless, results from our analysis show that active thermal management systems can successfully mitigate the accelerated degradation caused by increased temperature from rapid discharge.

The results of the case study simulations proved that the proposed devices can reduce grid reliance by around 20% and provide an average of around 20 miles of range in 10 minutes per fast charging event, all while maintaining safe battery temperatures. However, total energy consumption increased due to system efficiency losses and thermal management power consumption. Also, the energy savings were minimal unless the feed-in-rate paid for solar energy was sufficiently low. Thus, the economics of such a device

will likely be highly dependent on the prevalence of net-metering rates in the future. If the device is implemented in an area with net-metering rates, then it might be better to gear the device more toward vehicle charging and less toward energy cost reduction to maximize utility. Also, we expect that home DC fast charging will be of great value to the user, but as the size of electric vehicle batteries and the availability of charging infrastructure increase, range anxiety may be reduced such that home fast charging is less desirable.

Closer analyses of the case study results also revealed the trade-offs in how energy is used, as using more of the battery for home energy storage leaves less for vehicle charging and vice versa. There is wide variety of battery control schemes that could be chosen to balance these uses and maximize ultimate utility, but this is left for future analysis.

Overall, the analysis shows the feasibility of repurposing electric vehicle batteries for home energy storage and electric vehicle fast charging. Further work is needed, however, to determine the economic viability of such a device. This would include an estimate of device cost as well as a survey of potential customers to estimate the value of reduced grid reliance and home DC fast charging to the user. Such information would inform the optimal selection of design parameters like heat exchanger and liquid chiller size, DC fast charging speed, and the best balance between energy storage and vehicle charging. Additionally, including an estimate of device cost will allow for comparison with expected utility to the customer and thus determine if the concept device is economically viable.

REFERENCES

- [1] J. Shankleman, "The Electric Car Revolution Is Accelerating," in *Bloomberg News*, ed, 2017.
- [2] S. Santhanagopalan, K. Smith, J. Neubauer, G.-H. Kim, A. Pesaran, and M. Keyser, *Design and analysis of large lithium-ion battery systems*. Artech House, 2014.
- [3] M. O. Ramoni and H.-C. Zhang, "End-of-life (EOL) issues and options for electric vehicle batteries," *Clean Technologies and Environmental Policy*, vol. 15, no. 6, pp. 881-891, 2013.
- [4] J. Neubauer, K. Smith, E. Wood, and A. Pesaran, "Identifying and overcoming critical barriers to widespread second use of PEV batteries," National Renewable Energy Lab.(NREL), Golden, CO (United States)2015.
- [5] G. Reid and J. Julve, "Second life-Batteries as flexible storage for renewables energies," *Hg. v. Bundesverband Erneuerbare Energien eV (BEE)*, 2016.
- [6] R. Madlener and A. Kirmas, "Economic Viability of Second Use Electric Vehicle Batteries for Energy Storage in Residential Applications," *Energy Procedia*, vol. 105, pp. 3806-3815, 2017.
- [7] C. Heymans, S. B. Walker, S. B. Young, and M. Fowler, "Economic analysis of second use electric vehicle batteries for residential energy storage and load-levelling," *Energy Policy*, vol. 71, pp. 22-30, 2014.
- [8] F. Guo *et al.*, "Residential usage profile optimization and experimental implementation of the retired HEV battery with a hybrid microgrid testbed," in *Energy Conversion Congress and Exposition (ECCE), 2014 IEEE*, 2014, pp. 428-435: IEEE.
- [9] R. L. Fares and M. E. Webber, "The impacts of storing solar energy in the home to reduce reliance on the utility," *Nature Energy*, vol. 2, no. 2, p. 17001, 2017.
- [10] E. Hittinger and J. Siddiqui, "The challenging economics of US residential grid defection," *Utilities Policy*, vol. 45, pp. 27-35, 2017.
- [11] P. Hanser, R. Lueken, W. Gorman, and J. Mashal, "The practicality of distributed PV-battery systems to reduce household grid reliance," *Utilities Policy*, vol. 46, pp. 22-32, 2017.
- [12] (2018, 2/26/2018). *Meet Powerwall, your home battery*. Available: <https://www.tesla.com/powerwall>

- [13] S. Agnew and P. Dargusch, "Consumer preferences for household-level battery energy storage," *Renewable and Sustainable Energy Reviews*, vol. 75, pp. 609-617, 2017.
- [14] S. H. David Darling. (2016). *EIA data show average frequency and duration of electric power outages.* Available: <https://www.eia.gov/todayinenergy/detail.php?id=27892>
- [15] (2/26). *Vehicle Charging.* Available: <https://energy.gov/eere/electricvehicles/vehicle-charging>
- [16] Z. Lin and D. Greene, "Promoting the market for plug-in hybrid and battery electric vehicles: role of recharge availability," *Transportation Research Record: Journal of the Transportation Research Board*, no. 2252, pp. 49-56, 2011.
- [17] K. Tweed, "HECO Tests Batteries to Enable DC Fast Charging and Avoid Grid Upgrades," in *Greentech Media*, ed, 2016.
- [18] "Connected Energy and Renault to collaborate on energy storage and EV charging technology," ed: Renault Group, 2016.
- [19] "EVgo Wins Energy Storage North America 2016 Innovation Award," ed: EVgo, 2016.
- [20] J. PYPER, "How FreeWire's Second-Life Battery Packs Could Help EVs Go Mainstream," ed: Green Tech Media, 2017.
- [21] B. Nykvist and M. Nilsson, "Rapidly falling costs of battery packs for electric vehicles," *nature climate change*, vol. 5, no. 4, p. 329, 2015.
- [22] T. Reddy, "Linden's handbook of batteries 4th edition," ed: McGraw-Hill, New York, 2010.
- [23] J. T. Warner, *The handbook of lithium-ion battery pack design: chemistry, components, types and terminology.* Elsevier, 2015.
- [24] Q. Wang, B. Jiang, B. Li, and Y. Yan, "A critical review of thermal management models and solutions of lithium-ion batteries for the development of pure electric vehicles," *Renewable and Sustainable Energy Reviews*, vol. 64, pp. 106-128, 2016.
- [25] N. Nitta, F. Wu, J. T. Lee, and G. Yushin, "Li-ion battery materials: present and future," *Materials today*, vol. 18, no. 5, pp. 252-264, 2015.
- [26] (2017). *BU-105: Battery Definitions and what they mean.* Available: http://batteryuniversity.com/learn/article/battery_definitions

- [27] A. A. Pesaran, T. Markel, H. S. Tataria, and D. Howell, "Battery Requirements for Plug-in Hybrid Electric Vehicles--analysis and Rationale," National Renewable Energy Lab.(NREL), Golden, CO (United States)2009.
- [28] T. M. Bandhauer, S. Garimella, and T. F. Fuller, "A critical review of thermal issues in lithium-ion batteries," *Journal of the Electrochemical Society*, vol. 158, no. 3, pp. R1-R25, 2011.
- [29] G.-H. Kim and A. A. Pesaran, *Battery thermal management system design modeling*. Citeseer, 2006.
- [30] G. Liu, M. Ouyang, L. Lu, J. Li, and X. Han, "Analysis of the heat generation of lithium-ion battery during charging and discharging considering different influencing factors," *Journal of Thermal Analysis and Calorimetry*, vol. 116, no. 2, pp. 1001-1010, 2014.
- [31] Y. Shi, K. Smith, R. Zane, and D. Anderson, "Life prediction of large lithium-ion battery packs with active and passive balancing," in *American Control Conference (ACC), 2017*, 2017, pp. 4704-4709: IEEE.
- [32] K. Smith, Y. Shi, and S. Santhanagopalan, "Degradation mechanisms and lifetime prediction for lithium-ion batteries—A control perspective," in *American Control Conference (ACC), 2015*, 2015, pp. 728-730: IEEE.
- [33] K. Smith, A. Saxon, M. Keyser, B. Lundstrom, Z. Cao, and A. Roc, "Life prediction model for grid-connected Li-ion battery energy storage system," in *American Control Conference (ACC), 2017*, 2017, pp. 4062-4068: IEEE.
- [34] A. Assunção, P. S. Moura, and A. T. de Almeida, "Technical and economic assessment of the secondary use of repurposed electric vehicle batteries in the residential sector to support solar energy," *Applied Energy*, vol. 181, pp. 120-131, 2016.
- [35] A. Saez-de-Ibarra, E. Martinez-Laserna, C. Koch-Ciobotaru, P. Rodriguez, D.-I. Stroe, and M. Swierczynski, "Second life battery energy storage system for residential demand response service," in *Industrial Technology (ICIT), 2015 IEEE International Conference on*, 2015, pp. 2941-2948: IEEE.
- [36] L. Ahmadi, S. B. Young, M. Fowler, R. A. Fraser, and M. A. Achachlouei, "A cascaded life cycle: reuse of electric vehicle lithium-ion battery packs in energy storage systems," *The International Journal of Life Cycle Assessment*, vol. 22, no. 1, pp. 111-124, 2017.
- [37] L. Ahmadi, A. Yip, M. Fowler, S. B. Young, and R. A. Fraser, "Environmental feasibility of re-use of electric vehicle batteries," *Sustainable Energy Technologies and Assessments*, vol. 6, pp. 64-74, 2014.

- [38] E. Martinez-Laserna *et al.*, "Technical Viability of Battery Second Life: A Study from the Ageing Perspective," *IEEE Transactions on Industry Applications*, 2018.
- [39] S. Tong, T. Fung, and J. W. Park, "Reusing electric vehicle battery for demand side management integrating dynamic pricing," in *Smart Grid Communications (SmartGridComm), 2015 IEEE International Conference on*, 2015, pp. 325-330: IEEE.
- [40] H. Li, M. Alsolami, S. Yang, Y. M. Alsmadi, and J. Wang, "Lifetime Test Design for Second-Use Electric Vehicle Batteries in Residential Applications," *IEEE Transactions on Sustainable Energy*, vol. 8, no. 4, pp. 1736-1746, 2017.
- [41] S. J. Tong, A. Same, M. A. Kootstra, and J. W. Park, "Off-grid photovoltaic vehicle charge using second life lithium batteries: An experimental and numerical investigation," *Applied Energy*, vol. 104, pp. 740-750, 2013.
- [42] D. Muoio, "10 home batteries that rival Tesla's Powerwall 2," in *Buisness Insider*, ed, 2017.
- [43] "Telsa Powerwall 2 AC Datasheet," ed. Tesla.com, 2017.
- [44] "ESS LG Chem Catalog," ed: LG Chem, 2017.
- [45] (2017). *The sonnenBatterie*. Available: <https://www.sonnen-batterie.com/en-us/sonnenbatterie#sonnenbatterie-eco>
- [46] (2018). *XSTORAGE*. Available: <https://www.nissan.co.uk/experience-nissan/electric-vehicle-leadership/xstorage-by-nissan.html>
- [47] "xStorage Home," in *Eaton Nissan Home energy storage*, ed: EATON, 2017.
- [48] D. Muoio, "BMW's new rechargeable home battery could rival Tesla's Powerwall," in *Business Insider*, ed, 2016.
- [49] "RENAULT AND POWERVault GIVE EV BATTERIES A "SECOND-LIFE" IN SMART ENERGY DEAL," ed: Renault, 2017.
- [50] "2016 CHEVROLET VOLT BATTERY SYSTEM," ed: GM, 2016.
- [51] "Advanced Vehicles Testing," I. N. Labs, Ed., ed, 2013-2016.
- [52] R. Parrish *et al.*, "Voltec battery design and manufacturing," SAE Technical Paper0148-7191, 2011.
- [53] A. T. III, "Here comes the electric Nissan Leaf," ed. Fortune, 2010.
- [54] M. Ikezoe *et al.*, "Development of high capacity lithium-ion battery for nissan leaf," SAE Technical Paper0148-7191, 2012.

- [55] M. Shirk and J. Wishart, "Effects of electric vehicle fast charging on battery life and vehicle performance," Idaho National Laboratory (INL), Idaho Falls, ID (United States)2015.
- [56] D. Siry, "IN RACE TO MARKET, NISSAN'S ELECTRIC CAR TAKES SHORTCUTS," in *Wired*, ed, 2010.
- [57] M. Lee, "Focus Electric Battery Warranty Comes Up Short," ed: InsideEVs, 2012.
- [58] L. Ahmadi, M. Fowler, S. B. Young, R. A. Fraser, B. Gaffney, and S. B. Walker, "Energy efficiency of Li-ion battery packs re-used in stationary power applications," *Sustainable Energy Technologies and Assessments*, vol. 8, pp. 9-17, 2014/12/01/ 2014.
- [59] (2009). *Basics of MPPT Solar Charge Controller*. Available: www.leonics.com/support/article2_14j/articles2_14j_en.php
- [60] *Heat Exchangers*. Available: <https://www.qats.com/Products/Liquid-Cooling/Heat-Exchangers>
- [61] (2010). *MRC300,DH2,DV Re-circulating Chiller*. Available: <http://assets.lairdtech.com/home/brandworld/files/THR-DS-MRC300%200910.pdf>
- [62] D. Chen, J. Jiang, G.-H. Kim, C. Yang, and A. Pesaran, "Comparison of different cooling methods for lithium ion battery cells," *Applied Thermal Engineering*, vol. 94, pp. 846-854, 2016.
- [63] R. Karwa, *Heat and Mass Transfer*, 1st ed. ed. Springer, 2016.
- [64] A. Rattner and J. Bohren, "Heat and Mass Correlations," ed: Nov, 2008.
- [65] "Dry Air Properties," T. E. ToolBox, Ed., ed.
- [66] G. W. Recktenwald, "Finite-difference approximations to the heat equation," *Mechanical Engineering*, vol. 10, pp. 1-27, 2004.
- [67] (2017). *BU-808c: Coulombic and Energy Efficiency with the Battery*. Available: http://batteryuniversity.com/learn/article/bu_808c_coulombic_and_energy_efficiency_with_the_battery
- [68] J. Neubauer and E. Wood, "The impact of range anxiety and home, workplace, and public charging infrastructure on simulated battery electric vehicle lifetime utility," *Journal of power sources*, vol. 257, pp. 12-20, 2014.
- [69] B. R. Munson, T. H. Okiishi, A. P. Rothmayer, and W. W. Huebsch, *Fundamentals of fluid mechanics*. John Wiley & Sons, 2014.

- [70] (2012, 2/22/2018). *PUMP POWER CALCULATION*. Available: <https://neutrium.net/equipment/pump-power-calculation/>
- [71] T. Mathson and M. Ivanovich, "AMCA's Fan Efficiency Grades: Answers to Frequently Asked Questions," *ASHRAE Journal*, vol. 53, no. 9, p. S8, 2011.
- [72] B. Xu, A. Oudalov, A. Ulbig, G. Andersson, and D. Kirschen, "Modeling of lithium-ion battery degradation for cell life assessment," *IEEE Transactions on Smart Grid*, 2016.
- [73] S. Wilcox and W. Marion, "Users Manual for TMY3 Data Sets (Revised)," National Renewable Energy Lab.(NREL), Golden, CO (United States)2008.
- [74] *Heat Pump Systems*. Available: <https://www.energy.gov/energysaver/heat-and-cool/heat-pump-systems#303167-tab-0>
- [75] E. Wilson, "Commercial and Residential Hourly Load Profiles for all TMY3 Locations in the United States," *O. o. EE a. R. Energy, Ed., ed. US Department of Energy Open Data Catalog: US Department of Energy*, 2014.
- [76] M. Pipattanasomporn, M. Kuzlu, S. Rahman, and Y. Teklu, "Load profiles of selected major household appliances and their demand response opportunities," *IEEE Transactions on Smart Grid*, vol. 5, no. 2, pp. 742-750, 2014.
- [77] M. M. Armstrong, M. C. Swinton, H. Ribberink, I. Beausoleil-Morrison, and J. Millette, "Synthetically derived profiles for representing occupant-driven electric loads in Canadian housing," *Journal of Building Performance Simulation*, vol. 2, no. 1, pp. 15-30, 2009.
- [78] D. McCracken, "Synthetic High Resolution Solar Data," *Mater Thesis, Dept. Mechanical Engineering, University of Strathclyde*, 2011.
- [79] G. Vijayakumar, M. Kummert, S. A. Klein, and W. A. Beckman, "Analysis of short-term solar radiation data," *Solar energy*, vol. 79, no. 5, pp. 495-504, 2005.
- [80] J. Smart and S. Schey, "Battery electric vehicle driving and charging behavior observed early in the EV project," *SAE International Journal of Alternative Powertrains*, vol. 1, no. 1, pp. 27-33, 2012.
- [81] A. Santos, N. McGuckin, H. Y. Nakamoto, D. Gray, and S. Liss, "Summary of travel trends: 2009 national household travel survey," 2011.
- [82] J. S. Neubauer and E. Wood, "Will your battery survive a world with fast chargers?," SAE Technical Paper0148-7191, 2015.
- [83] "Solar Edge Single Phase StoreEdge Solutions for North America," SolarEdge, Ed., ed, 2017.

- [84] (2017). *SUNNY BOY STORAGE 3.8-US*. Available: <http://files.sma.de/dl/30859/SBS3.8-5.0-6.0-US-DUS173415W.pdf>
- [85] (2017, 4/5/2018). *Smart DC/DC Converter Buck-Boost-Bidirectional*. Available: https://www.tame-power.com/sites/tame-power.com/files/datasheet/converter/conv-dcdc-xxkw-xxxx-01-x_liquid_ed03.pdf
- [86] C. FLEMING, "Nissan turns out a new battery electric Leaf," in *Los Angeles Times*, ed, 2018.
- [87] *Charging Plug-In Electric Vehicles at Home*. Available: https://www.afdc.energy.gov/fuels/electricity_charging_home.html
- [88] N. Bomey, "Average age of cars on U.S. roads breaks record," in *USA Today*, ed. usatoday.com, 2015.
- [89] D. DeMuro, "2013 Nissan Leaf Gets New Battery Warranty," ed. Autotrader, 2013.
- [90] (2013). *2013 Model Year Ford Hybrid Car and Electric Vehicle Warranty Guide*. Available: <https://www.ford.com/resources/ford/general/pdf/2013HybridWarranty.pdf>
- [91] G. A. Hazelrigg, *Fundamentals of decision making for engineering design and systems engineering*. 2012.
- [92] M. Malik, I. Dincer, M. A. Rosen, M. Mathew, and M. Fowler, "Thermal and electrical performance evaluations of series connected Li-ion batteries in a pack with liquid cooling," *Applied Thermal Engineering*, vol. 129, pp. 472-481, 2018.
- [93] B. Wu, Z. Li, and J. Zhang, "Thermal design for the pouch-type large-format lithium-ion batteries I. thermo-electrical modeling and origins of temperature non-uniformity," *Journal of the Electrochemical Society*, vol. 162, no. 1, pp. A181-A191, 2015.
- [94] S. J. Drake, *Thermal conduction and heat generation phenomena in Li-ion cells*. The University of Texas at Arlington, 2014.
- [95] P. Taheri and M. Bahrami, "Temperature rise in prismatic polymer lithium-ion batteries: An analytic approach," *SAE International Journal of Passenger Cars-Electronic and Electrical Systems*, vol. 5, no. 2012-01-0334, pp. 164-176, 2012.
- [96] L. Saw, A. Tay, and L. W. Zhang, "Thermal management of lithium-ion battery pack with liquid cooling," in *Thermal Measurement, Modeling & Management Symposium (SEMI-THERM), 2015 31st*, 2015, pp. 298-302: IEEE.
- [97] P. A. Nelson, K. G. Gallagher, I. D. Bloom, and D. W. Dees, "Modeling the performance and cost of lithium-ion batteries for electric-drive vehicles," Argonne National Laboratory (ANL)2012.

- [98] (2018, 4/5/2018). *Climate Phoenix - Arizona*. Available: <https://www.usclimatedata.com/climate/phoenix/arizona/united-states/usaz0166>
- [99] E. Open, "Transparent cost database," ed: Retrieved from Open EI: <http://en.openei.org/apps/TCDB>, 2014.